Università degli Studi di Padova
Department of Industrial Engineering

Ph.D. COURSE IN: Industrial Engineering

CURRICULUM: Materials Engineering

Cohort XXXVIII

Permeability and Mechanical Properties of Triply Periodic Minimum Surface Shell Structures Produced by Additive Manufacturing

Thesis for the degree of Doctor of Philosophy

Coordinator: Prof. Paolo Sgarbossa
Supervisor: Prof. Paolo Colombo
Co-Supervisor: Prof. Giorgia Franchin

Ph.D. student : Yu Zhang

Padova

September 30,2025

Acknowledgements

First of all, I want to thank my supervisor Professor Paolo Colombo and co-supervisor Professor Giorgia Franchin for their kind and warm guidance. Professor Paolo Colombo always provides me with timely professional guidance when I need help and also assists me in contacting other scholars who can offer academic support.

Then, I want to thank Dr. Marco D'Agostini, Dr. Subhadip Bhandari and Dr. Kai Huang for their assistance in my research. Under their patient guidance, I quickly became familiar with and mastered the relevant experimental methods and devices. Meanwhile I want to thank Prof. Simone Carmignato and Dr. Nicolò Bonato (Dipartimento di Tecnica e gestione dei sistemi industriali) for their graceful help in providing the XCT data.

And most important, I want to thank my wife, Dr. Cao Siwen, for her companionship, support, and understanding, which have provided me with strong backing during my studies away from home. And thank Ph.D. student Heqiang Liu, Xiang Li, Junbing Lu and visiting Post-doctor Li Qiaolei for their companionship and daily academic discussions.

Finally, I would like to thank the China Scholarship Council (202209210003) for giving me the chance to do my research.

Abstract

The additive manufacturing technique has developed rapidly in recent years, and the widespread application makes it accessible to create complex porous structures. The Triply Periodic Minimum Surface (TPMS) structures, which have smooth and connected channels and high geometric surface area, are now being used in many areas such as biomimetic materials, energy absorption systems, catalyst systems, and lightweight design. Meanwhile, those applications also give more requirements for better structural design with TPMS structures.

This research aims to investigate the influence of the design of different TPMS structures on their permeability and mechanical properties. Specifically, an orthogonal experimental design was used to study how TPMS architectures, porosity, and cell size affect permeability and mechanical properties. Moreover, the effect of the weight function on the mechanical properties of a one cell hybrid TPMS structure was also investigated.

The results of orthogonal experiments show that the Primitive TPMS structure has the highest permeability but the lowest mechanical properties. Permeability (k_1) increases with porosity, and so do the Forchheimer coefficient β, Young's modulus, and energy absorption. Porosity is the most important factor for all properties. For permeability, TPMS structure type is less important for k_1 but more important for β, meaning it has a larger effect in high-speed flow than in slow flow. For mechanical properties, Young's modulus and energy absorption show similar trends, suggesting they can be improved together by controlling the same factors.

For hybrid TPMS structures, the Young's modulus results are affected by the cell number and become stable when the cell number is 3*3*3 or larger. Structures made by combining the hybrid TPMS cell and its mirror symmetry structure cell by different sequences show similar mechanical properties, which means this assembly method is feasible. For hybrid TPMS structures with linear and nonlinear weight functions, mechanical properties differ in the x, y, and z directions, showing both are anisotropic. For the linear hybrid TPMS structures, the Young’s modulus in x and y directions is much lower than z direction, and for the nonlinear hybrid, which in y and z directions is similar and higher than x direction. Compression strength experiments show the linear hybrid improves all mechanical properties compared to basic Gyroid and Diamond TPMS, while the nonlinear hybrid mainly improves the Young's modulus. Three-point bending experiments show that both hybrid structure beams perform better than basic TPMS structure beams in most properties. The linear hybrid beam has higher energy absorption, while the nonlinear hybrid beam has higher flexural modulus. This means that the weight function can be used to affect the mechanical performance of hybrid TPMS structures.

Contents

Index of Figures

Index of Tables

1. Introduction

Structures with pores, such as cellular structures, have a significant advantage in biomimetic materials, energy absorption systems, catalyst systems, and lightweight design. With the development of the Additive Manufacturing (AM) techniques, it has become possible to design complex porous structures according to the requirements and details of specific applications, which are unachievable through traditional manufacturing techniques. As a periodic porous structure, Triply Periodic Minimal Surfaces (TPMS) have several advantages over traditional porous structures, such as smooth, interconnected channels, easy and precise controllability volume of porosity, and high geometric surface.

Research on TPMS structures and more complex hybrid TPMS structures aims to investigate the permeability and mechanical properties of TPMS-based porous designs, providing insights for further enhancing the performance of structures designed with TPMS. This chapter first reviews the development of additive manufacturing techniques and then introduces the characteristics and current research of fundamental TPMS structures and hybrid TPMS structures.

1.1. Additive manufacturing

Manufacturing refers to the process of transforming raw materials into products using one or more technologies, on the basis of drawings or molds. Generally, as Fig. 1 shows, manufacturing techniques include: subtractive manufacturing (SM), formative manufacturing (FM), and additive manufacturing (AM) [1,2]. Subtractive manufacturing generates products by removing excess material through machining, drilling, grinding, etc. [3] Formative manufacturing uses molds or other tools to shape raw materials into products or semi-finished parts [2]. Additive manufacturing builds up materials layer by layer to rapidly fabricate products or green bodies [4]. Subtractive manufacturing and formative manufacturing are relatively mature processes, capable of using a wide range of materials and well suited for large scale production conditions. Their production costs decrease progressively as manufacturing scale increases. In contrast, additive manufacturing is a relatively new technique with a shorter development history. The types of materials suitable for additive manufacturing are still somewhat limited, and its cost is difficult to reduce significantly in large scale production conditions [5]. However, additive manufacturing offers significant advantages in fabricating complex structural components. Compared to subtractive and formative manufacturing, additive manufacturing can easily make porous parts with complex interconnected structures [6-8] and can be used to make multi-material composite components [9-11]. Moreover, in small batch production and rapid prototyping applications, AM greatly speeds up the efficiency of the design, manufacturing, validation, and improvement cycle due to its rapid prototyping ability. In recent years, additive manufacturing has developed rapidly [12-14] and, thanks to its advantages, has gained widespread adoption in its specialized domains.

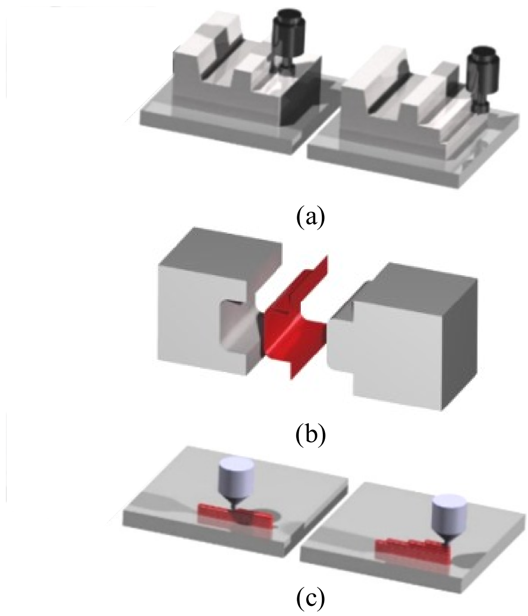

Figure 1. Manufacturing techniques. (a) Subtractive manufacturing (SM). (b) Formative manufacturing (FM). (c) Additive manufacturing (AM). [2]

The development of additive manufacturing technology began in the 1980s [15], and the range of materials it can process has been expanded widely. Today, the additive manufacturing technique can fabricate parts from polymers, metals, ceramics and more, including fiber-reinforced composites [16]. To meet the processing requirements of different materials, various AM techniques based on different methods have been developed [17]. As shown in the Fig. 2 below, common additive manufacturing techniques used in engineering applications include: binder jetting (BJT), directed energy deposition (DED), material extrusion (MEX), material jetting (MJT), powder bed fusion (PBF), sheet lamination (SHL), and vat photopolymerization (VPP) [18]. Additionally, depending on whether post processing is required after fabrication, additive manufacturing processes can be categorized into multi-step and single-step processes. For instance, polymer materials, ABS, PLA, are typically produced via the single-step process of additive manufacturing, that is the final product doesn't require any additional processes, while ceramic materials, such as zirconia and alumina, generally require multi-step processing of additive manufacturing that include debinding and sintering after shaping [19,20].

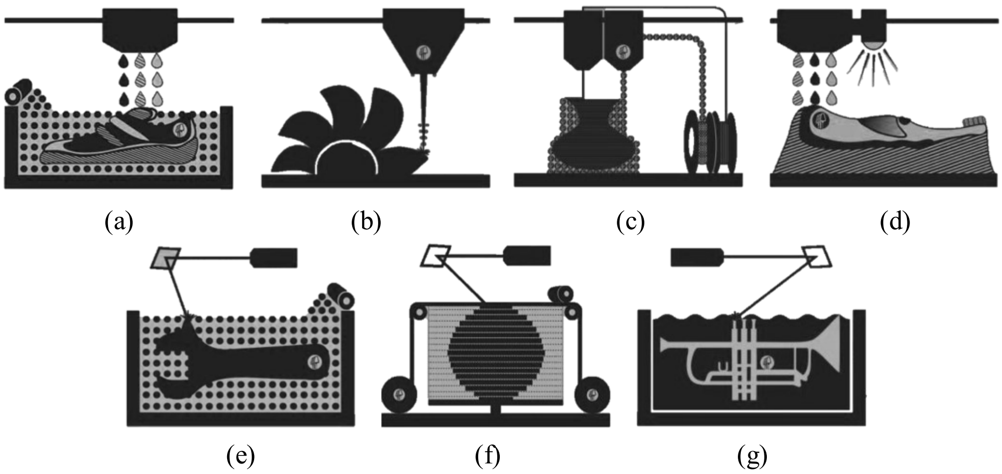

Figure 2. Additive manufacturing techniques. (a) Binder jetting (BJT). (b) Directed energy deposition (DED). (c) Material extrusion (MEX). (d) Material jetting (MJT). (e) Powder bed fusion (PBF). (f) Sheet lamination (SHL). (g) Vat photopolymerization (VPP). [18,21]

In the early years of additive manufacturing technique development, the materials used were solely polymers or metals [22]. In recent years, as additive manufacturing technology has gained increasing attention and developed rapidly, its application has broadened, and new requirements are imposed on the materials that can be processed by additive manufacturing [23].

As materials known for its corrosion resistance and excellent mechanical properties, ceramics are becoming increasingly used in additive manufacturing [24,25]. There are various techniques for additive manufacturing of ceramics. Laser Powder Bed Fusion (L-PBF) [25-27] and Directed Energy Deposition (DED) [28-30] technologies can directly produce ceramic components, i.e., the single-step processes additive manufacturing [31]. Multi-step processes additive manufacturing is more widely applied, with major techniques including Binder Jetting (BJT) [32-34], Material Extrusion (MEX) [35-37], and Vat Photopolymerization (VPP) [38-40]. The typical manufacturing steps of them include model design, slicing, additive manufacturing of green bodies, and post-processing [41]. Generally, post-processing involves debinding and sintering to obtain the final ceramic parts needed.

1.2. TPMS structures

Triply Periodic Minimal Surfaces (TPMS) have attracted significant interest as highly versatile and functionally advantageous structures, especially in fluid transport and mechanical performance applications. Table 1 gives the TPMS structures and its equation, the inherent geometric complexity, characterized by smooth, interconnected channels and high geometric surface [42], makes them an ideal structure for optimizing permeability in porous media while maintaining mechanical strength, and for structural designing of lightweight or energy absorbing components [43-46]. Integrating TPMS architecture into fields such as biomimetic design, Fig. 3, energy absorption systems, and catalyst systems highlights their potential in fluid flow and mechanical performing structures, and understanding the influence of their topological features on permeability and mechanical properties is important for advancing their application in several fields.

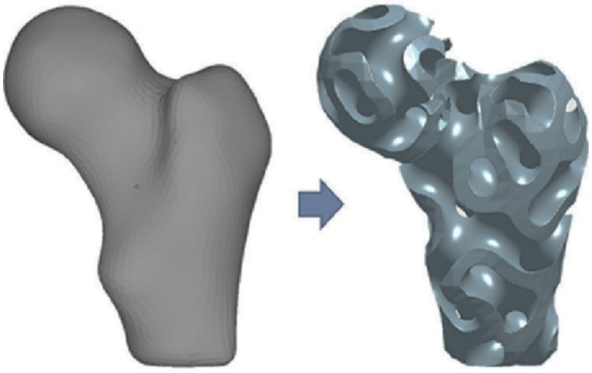

Figure 3. Application of TPMS structures. [47]

Table 1. TPMS structures and the equation. [48]

Equation of TPMS structure	TPMS structure
Primitive: $\Phi_P = cos(X) + cos(Y) + cos(Z) = c$	
Gyroid: $\Phi_G = sin(X)\,cos(Y) + sin(Y)\,cos(Z) + sin(Z)\,cos(X) = c$	
Diamond: $\Phi_D = cos(X)\,cos(Y)\,cos(Z) - sin(X)\,sin(Y)\,sin(Z) = c$	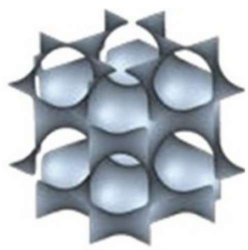

I-WP:

$$\Phi_{I-WP} = 2\big[cos(X)\,cos(Y) + cos(Y)\,cos(Z) + cos(Z)\,cos(X) - [cos(2X) + cos(2Y) + cos(2Z)]\big] = c$$

F-RD:

$$\Phi_{F-RD} = 4\,cos(X)\,cos(Y)\,cos(Z) - [cos(2X)\,cos(2Y) + cos(2Y)\,cos(2Z) + cos(2Z)\,cos(2X)] = c$$

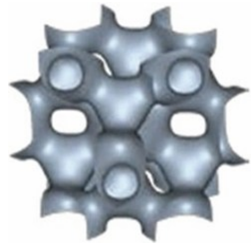

I2-Y:

$$\Phi_{I2-Y} = -2[sin(2X)\,sin(Y)\,sin(Z) + sin(X)\,sin(2Y)\,sin(Z) + sin(X)\,sin(Y)\,sin(2Z)] + co\,s(2\mathrm{X})\cos(2\mathrm{Y}) + \cos(2\mathrm{Y})\cos(2\mathrm{Z}) + \cos(2\mathrm{Z})\cos(2\mathrm{X}) = \mathrm{c}$$

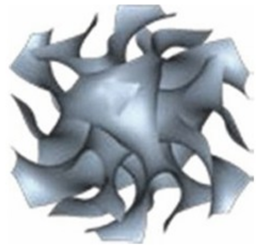

Research on the permeability properties of TPMS structures has predominantly focused on quantifying the fluid flow as a function of their topology, by carrying out permeability experiments and simulations. Thakur et al. [49] and Nhaichaniya et al. [50] reported superior permeability and nutrient transport in TPMS structures, while Pires et al. [51] and Santos et al. [52] showed that geometry, beyond porosity, governs fluid flow and that Gyroid often achieves higher permeability than the Schwarz Diamond structure. Ali et al. [53] and Rathore et al. [54] linked pore size variation, morphology, and tortuosity to wall shear stress, flow regime, and uniform fluid distribution. Gabrieli et al. [55] and Castro et al. [56] experimentally confirmed that Diamond/Gyroid outperform IWP or Schwarz P in permeability for tissue engineering. Zeng and Wang [57] and Montazerian et al. [58] investigated TPMS structure permeability via parametric control and consideration of transport directions, and Lumba et al. Penubarthi et al. [59] showed favorable capillary performance and permeability in Gyroid/Diamond for thermal management, and Zhou et al. [60] demonstrated Ti64–5Cu Gyroid with high permeability and corrosion resistance for implants. Karaman and Ghahramanzadeh Asl [61] and Sauermoser-Yri et al. [62]

compared sheet and different network architectures, reporting, respectively, superior permeability and uniform shear stress distribution in sheet-based designs and higher permeability in Schwarz primitive. Li et al. [63] and Liu et al. [64] proposed optimization and topological strategies to customize permeability while maintaining mechanical strength. Tian et al. [65] and Hesselmann et al. [66] extended TPMS to process and device applications, showing that structural design enables high permeability and controlled flow distribution without sacrificing mechanical properties.

Concerning mechanical properties, porous TPMS architectures can provide functional structural components with tailored Young's modulus and energy absorption [67,68], as demonstrated both experimentally and numerically. Qiu et al. [69] and Feng et al. [70] and Guan et al. [71] and Ravichander et al. [72] tested metal and polymer TPMS by experiments and simulations, showing improved mechanical properties: load-bearing capacity, stable deformation, and higher specific energy absorption. Al-Ketan et al. [73] and Yang et al. [74] and Ma et al. [75] and Chen et al. [76] reported pore-gradient, functionally graded, amplitude- and frequency-controlled lattices that enable tunable stiffness, multi-platform stress–strain behavior, and robust energy absorption. Luo et al. [77] and Zhao et al. [78] developed interpenetrating and strut-shell TPMS, avoiding sharp stress drops and achieving tunable anisotropy. Cao et al. [79] and Viet et al. [80] and Guo et al. [81] compared Primitive, Gyroid, Diamond, IWP and skeletal vs strut architectures, showing Gyroid has stable orientation response, Primitive has higher anisotropy, IWP and Diamond have favorable stiffness, and skeletal-TPMS provides uniform stress transfer. Sengsri et al. [82] and Xi et al. [83] and Jian et al. [84] and Chatzigeorgiou et al. [85] and Song et al. [86] targeted applications in bridge bearings, impact protection, acoustic metastructures, and biomedical implants, confirming good energy absorption, reduced stress shielding, and matched bone-like behavior.

For mechanical and permeability investigations, Bobbert [87] showed that TPMS-based metallic biomaterials combine favorable topology, mechanical property, mass transport, with high fatigue resistance and bone-range permeability. Xu [88] and Montazerian [89] reported that radial/graded porosity TPMS scaffolds enhance mechanical modulus/strength and fluid permeability, comparable to natural bone. Li [63] and Zeinali [90] enabled design control via multi-objective optimization and numerical simulation, allowing independent tuning and prediction of elastic modulus and permeability for balanced mechanobiological properties.

However, the coupled effects of different structural parameters (e.g., unit cell size, wall thickness, porosity gradient) on both permeability and mechanical properties remain unquantified and, considering the multi factors dependencies of TPMS permeability and mechanical properties, an orthogonal experimental design approach provides a powerful method to ascertain the significant sequence of factors affecting the properties. In fact, this approach can systematically reduce the number of experiments and has been widely adopted in several fields to optimize processes and designing parameters [91,92]. For instance, Guo et al. employed orthogonal experimental design to investigate the influence of the FDM 3D printing parameters on the mechanical properties of PLA TPMS structures [93].

1.3. Hybrid TPMS structures

Although the extensive family of Triply Periodic Minimal Surfaces (TPMS) structures, which includes well-known types such as Primitive, Diamond, and Gyroid, already provides a wide range of options for lightweight designing and other industrial requirements, the mechanical properties offered by a single, uniform TPMS structure are inherently limited and fixed. This limitation means that, for design applications with highly specific or complex mechanical performance demands, a single TPMS structure may not be sufficient. Consequently, as Fig. 4 shows, combining multiple TPMS cells to form a hybrid TPMS structure has emerged as a viable and effective approach to overcome this constraint. In the case of hybrid TPMS structures, the use of appropriate hybrid methods or the selection of specific constituent components allows for the tailoring of mechanical properties, enabling the structure to exhibit distinct responses in different loading directions.

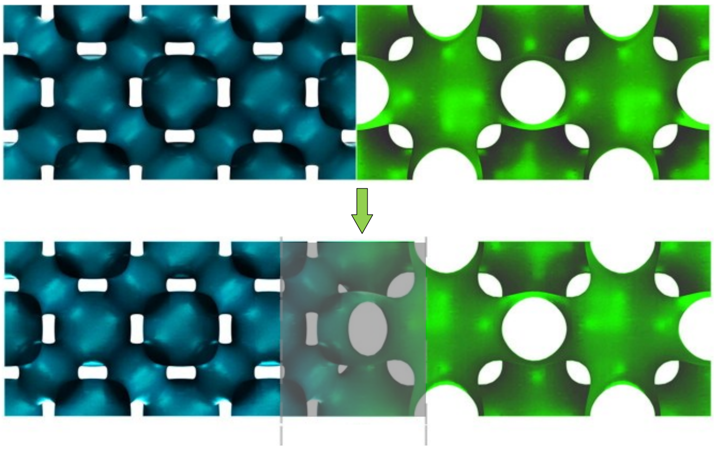

Figure 4. Hybrid of TPMS structures. [94]

Lu et al. [95] and Song et al. [96] examined hybrid Gyroid–Primitive and other hybrid TPMS under static and dynamic loading, showing improved energy absorption capacity, deformation stability, and damage tolerance. Novak et al. [97,98] reported distinct deformation modes, progressive deformation, and higher energy absorption for Gyroid–Diamond hybrid lattices. Nazir et al. [99] designed nature-inspired hybrid lattices by material extrusion, also achieving progressive deformation and improved energy absorption over uniform morphology. Gao et al. [100] targeted functional property regulation, with anisotropy and directional elastic modulus control by hybridization, and elastic wave manipulation via air–solid phases to control stress wave transmission and enhance acoustic isolation. For thermal–flow applications, Wang et al. [101] analyzed functionally graded hybrid TPMS heat exchangers and showed improved heat transfer efficiency with reduced flow resistance in compact heat exchanger layouts.

Moreover, it is important to note that the method of hybridization can also influence the properties of hybrid TPMS structures. When compared to basic TPMS structures, these tailored characteristics provide hybrid TPMS structures with substantially broader potential for a variety of applications, particularly in fields such as lightweight design. Therefore, a thorough investigation into the regulation of properties in hybrid TPMS structures is crucial for their effective and reliable implementation in these advanced engineering fields.

Gao et al. [102], Yin et al. [103], and Zhang et al. [46, 104] examined hybridization direction and orientation effects, revealing that loading direction relative to hybrid interfaces and component arrangement critically influence deformation behavior and energy absorption characteristics. Li et al. [105], Li et al. [106], and Yoo and Kim [107] investigated transition region characteristics, showing that shape, position, weighting parameters, and volume proportions of transition boundaries affect stress distribution and mechanical performance. Zhang et al. [108, 109] studied multi-stage mechanisms and transition geometry, finding that component proportion, transition layer width, transition radius, and component distribution determine stress response stability and impact resistance. Liu et al. [110] and Wang et al. [111] explored wall thickness effects, demonstrating that continuous and discrete thickness variations, along with unit cell size, effectively control deformation patterns and prevent premature failure. Ye et al. [112] and Na et al. [113] examined structural fusion parameters, revealing that rotation direction, angle of inner-layer units, fusion coefficient, and transition interface design critically affect permeability, mechanical stability, damage tolerance, and energy absorption efficiency.

Moreover, weight functions utilized in the generation of the hybrid structure, such as linear or nonlinear functions, exert a significant influence on the resulting mechanical properties of the hybrid TPMS structure, when compared to basic, single-unit TPMS structures. Gao et al. [94] focused on weight function design, using Sigmoid functions and volumetric distance fields to achieve smooth transitions, demonstrating that weight functions control elastic modulus and anisotropy. Most of the above research either use hybrid TPMS structures as a transition layer between two basic TPMS structures or generates hybrid TPMS across multiple cell sizes.

This study focuses on the mechanical properties of the one cell hybrid TPMS structure with different weight functions, and of structures made by combining several of these one cell hybrid TPMS structures

1.4. Research approach

This research aimed to experimentally investigate the permeability and mechanical properties of basic TPMS structures and hybrid TPMS structures, providing insights for further enhancing the performance of structures designed with TPMS. The details are as follows:

For basic TPMS structures, the orthogonal experimental design was applied to investigate the effects of three factors, namely TPMS architecture, porosity, and cell size, on two permeability (Darcy permeability coefficient k_1 and Forchheimer coefficient β) and two mechanical characteristics (Young's modulus and energy absorption). Using the FDM additive manufacturing technique, both PLA and zirconia samples were fabricated and tested under controlled fluid flow and mechanical loading conditions. The aim was to quantify the effects of TPMS architecture, porosity, and cell size on permeability and mechanical properties, determining the significance of each factor, and provide a reference for further designing and optimizing of TPMS structures in applications where permeability and mechanical properties are of interest.

For hybrid TPMS structures, a program was developed with Python to create a one cell hybrid TPMS structure, and structures made by combining several of these one cell hybrid TPMS structures. With the FDM additive manufacturing technique, alumina samples were fabricated and tested by uniaxial compression and three-point bending experiments. The mechanical properties of TPMS structures with different cell configurations, the mechanical properties and anisotropy of hybrid TPMS structures with different weight functions were investigated. The main aim of the work was to expand the applicability of hybrid TPMS structures in engineering fields requiring tailored mechanical and fluid transport performance.

2. Triply Periodic Minimum Surface (TPMS) Shell Structures Modeling

Even though the mathematical equations for Triply Periodic Minimum Surface (TPMS) are always concise, modeling these cellular structures with traditional software, like SolidWorks and Autodesk CAD, etc., is still a challenge. Considering the requirement of parameter-driven TPMS structures generation and more complex TPMS structures, such as the hybrid TPMS structures in Chapter 5, developing software for TPMS structures modeling is more efficient. In this chapter, with Python programming language and the program library of VTK and PyVista, the modeling of basic geometry, TPMS shell structures, and hybrid TPMS shell structures were investigated.

2.1. Implicit modeling and visualization

For the Additive Manufacturing technique, as Fig. 5 shown, .STL file is the most commonly used file format to describe geometry structures, which formats a geometry structure as a series of triangle facets, and then store the nodes three dimension coordinates data and the facets. For a solid body, the triangle facet is enclosed, and for a surface, they are not.

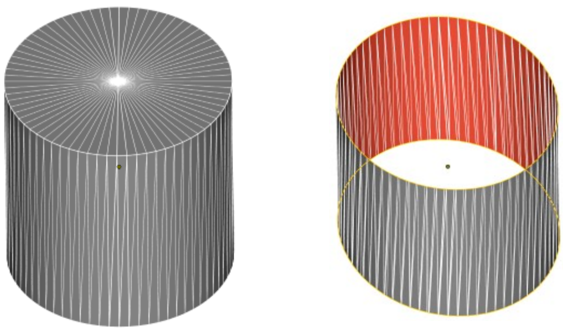

(a) (b)

Figure 5. Solid and surface models with .STL format and show of triangle facet. (a) solid model. (b) surface model.

Generally, .STL format models can be generated by two technique routines, first one is Polygonal modeling generate directly, like 3D max and Blender, which allow user to generate mesh model and modify in vertex level of .STL models directly. The second method is boundary representations (B-reps) based software, like SolidWorks, Rhino, etc., theoretically, which can accurately characterize the geometric features of regular geometry structures, and can easily be modelled parametrically. Both two methods are the Explicit modeling method, which mainly define and modify the geometry element, vertex, line, and face, and can generate the geometry structures directly and intuitively, but for complex cellular structures in this research, modeling a geometry structure by the Explicit modeling method is not effective, and for software like SolidWorks, even they support parameter modeling, there still is limitation for complex cellular structures. For the requirement of modeling those kinds of cellular structures, the Implicit modeling is an efficient tool.

Implicit modeling is a powerful and advanced geometry modeling tool, and is becoming more popular in various applications, such as additive manufacturing models designing, which represents a geometry structure as a field function $\Phi(x,y,z)$ related to the space coordinates instead of the structure boundary. The field function can be defined differently, generally, for simple geometry structures, such as a circle in 2D space, the field function can be defined as the implicit function of the 2D circle:

$$\Phi(x, y) = x^2 + y^2 - R^2 = c \tag{1}$$

where, x, y is the coordinates of the 2D space, R is the radius of the circle, and c is the iso-value which defines the curve of the circle. For R=1, Fig. 6 gives the 2D circle field function generated by Implicit modeling, and we can see that the curve corresponding to the iso-value c=0 is the circle we want by implicit modeling, and the field function inside the circle are negative, and outside the circle are positive, which is the basic characters of the implicit model.

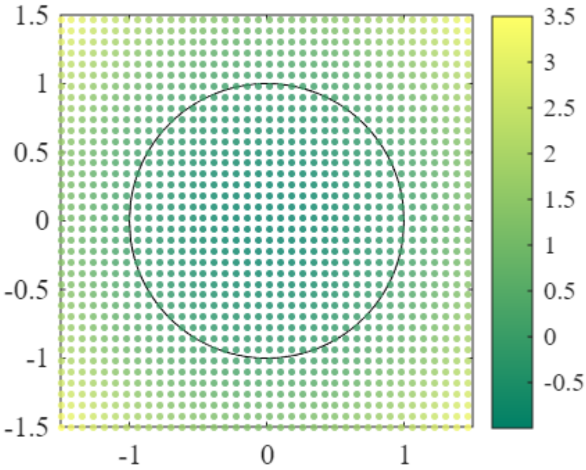

Figure 6. 2D circle field function results.

However, using the implicit function of simple geometry structure can bring error and limitation for complex geometry operation applications and geometry structures. For geometry operation like offset, Fig. 7 gives the line defined by Equation 2, where the line 1 passing through points (1,0) and (0,1) is the line represent to *c*=0, the line 2 passing through points (1.5,0) and (0,1.5) is the line represent to *c*=0.5, and the line 3 passing through points (1.7,0) and (0,1.7) is the line represent to *c*=0.7, where the distance between line 1 to line 2 and line 3 are 0.35 and 0.5, respectively, which means that by increasing the iso-value, one can move the offset line toward the negative side of the original line, but the increased value doesn't correspond to the correct offset value.

$$\Phi(x,y) = x + y - 1 = C \tag{2}$$

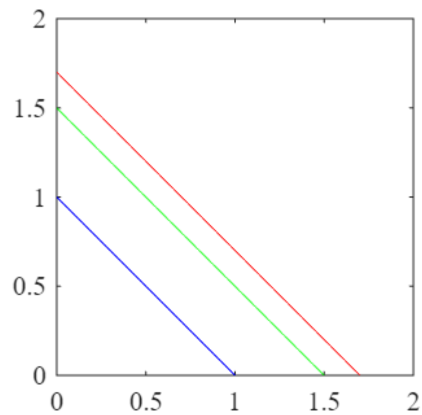

Figure 7. Offset error of using implicit function as field function.

Meanwhile, for geometry structures which come from CT and other geometry scanning methods, in Fig. 8 shows the reconstructed 3D model, but the exact implicit function and using implicit functions are no longer suitable, while the Signed Distance Field (SDF) is a better option for the field implicit function Φ. As Fig. 9 shows, the SDF is defined as the minimum distance of each point of the space coordinates to the surface of geometry structures and, in this research, every implicit geometry structures generated by the implicit function based implicit modeling will be transferred to the SDF based field function for better Boolean operation and, differently to the implicit function, the SDF value inside the geometry structures is positive and outside is negative. As Fig. 8 shows, with the help of SDF, we can import and convert the traditional .STL to the implicit model and do further work.

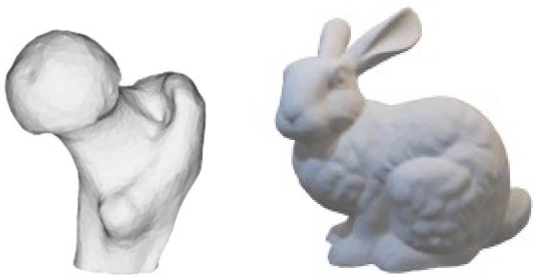

(a) (b)

Figure 8. Complex structres. (a) Femoral head 3D model by CT. (b) Stanford Bunny scanned with the Stanford Large Statue Scanner. [114, 115]

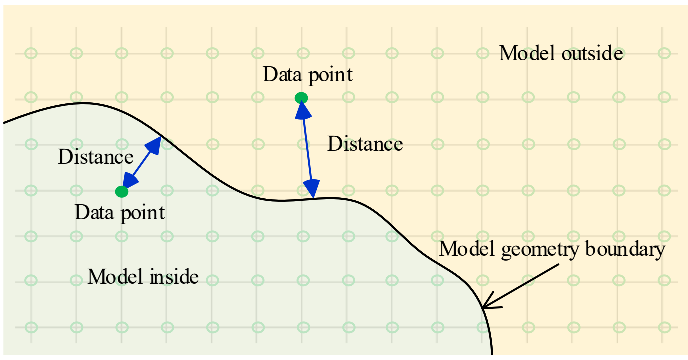

Figure 9. Signed Distance Field definition.

For implicit modeling, Boolean operation is a very strong advantage in comparison to B-rep modeling methods. The Implicit modeling method is field based, and the geometry structures generated by it are a naturally watertight structure, and all Boolean operations edit the field of the geometry structures directly, which makes the Boolean operation in Implicit modeling a robust and efficient operation. The equations of the Boolean operation for Implicit modeling are given below.

$$\text{Intersect: } f_{1\cap 2} = \min(f_1, f_2) \tag{3}$$

$$\text{union: } f_{1\cup 2} = \max(f_1, f_2) \tag{4}$$

$$\text{subtract: } f_{1-2} = \min(f_1, -f_2) \tag{5}$$

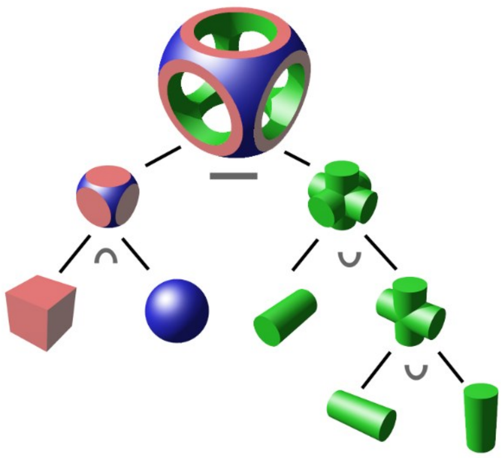

Figure 10. Example of boolean operation modeling. [116]

With SDF, the .STL format geometry can be imported and edited by Implicit modeling and, for additive manufacturing applications, the .STL format is still the most important file that is used. To extract the geometry structures from Implicit modeling, in this research the program function vtkContourFilter() of the open source software VTK was used, which can extract the contour of the field function and generate the .STL format geometry structures file. Fig. 11 shows the wireframe diagram of the .STL model and the implicit modeling data point cloud corresponding to its SDF.

Figure 11. SDF of a geometry structures and its .STL format geometry.

2.2. TPMS shell structures

Generally, the implicit function of a TPMS structure can be defined according to Fourier series [117]:

$$\Phi(r) = \sum_n A_n \cos[2\pi n \cdot r - p_n] = 0 \tag{6}$$

where, n is the lattice vector, A_n is the amplitude, p_n is the phase shift. With different parameters and appropriate truncation, the implicit functions of the most common TPMS structures are listed in Table 1.

Specifically, for a Gyroid TPMS surface, the implicit function is:

$$\Phi_G = \sin(X)\cos(Y) + \sin(Y)\cos(Z) + \sin(Z)\cos(X) = c \tag{7}$$

where, $X=2\pi x/T$, $Y=2\pi y/T$, $Z=2\pi z/T$, T is the cell size, and c is the offset coefficient. Figure 12 gives the process of generating a Gyroid solid shell from Gyroid surfaces. For $c=0$ is the zero iso surface of the Gyroid in Fig. 12(a), to generate a shell solid model, an offset value should be applied in Equation 7, with given offset value c, and positive offset and negative offset iso surfaces are plotted in Fig. 12(b), then, with a given boundary, such as cube, cylinder, sphere, or import model boundary, in Fig. 12(c), with the Boolean operation in Equation 3, the Gyroid solid shell model is obtained, as shown in Fig. 12(d).

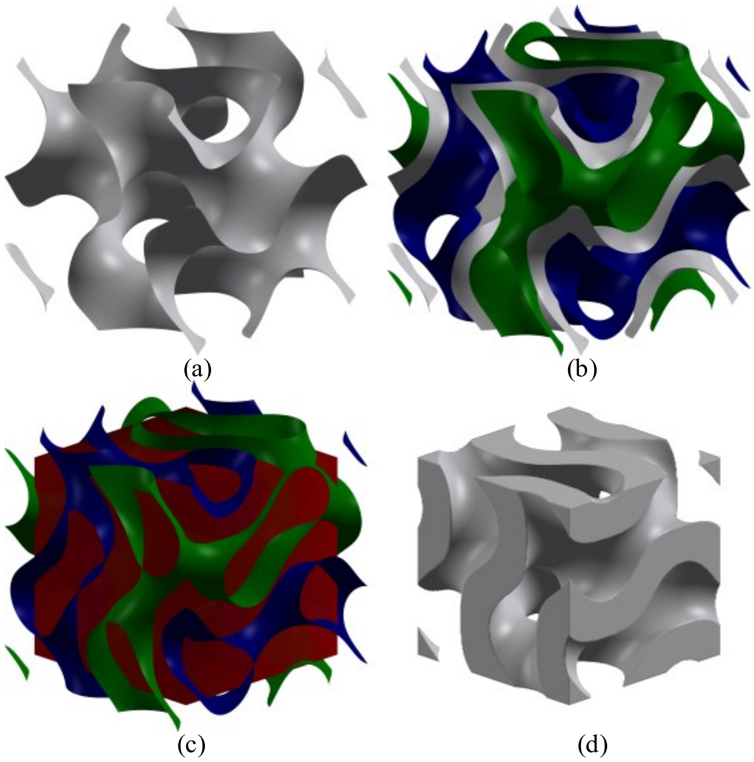

Figure 12. Generating a Gyroid solid model by its surface. (a) Gyroid zero value iso surface. (a) Gyroid zero value and its positive and negative offset iso surfaces. (c) Offset iso surface intersected with a cube. (d) Gyroid solid model.

Meanwhile, for a TPMS structure, by changing the cell size T and offset value c, the shape and porosity of the shell structure change. The pore size can be considered as the distance between two solid walls within a structure, but there is no uniform definition of pore size for different TPMS architectures, cell size is defined as the dimension of the minimum geometrical unit representing the TPMS structure. The more cells in a structure of a given volume, the smaller the cell size is, and Fig.13 shows the shell structures for a Gyroid TMPS with varying cell size T and porosity ϕ. Gyroid structures with the same porosity but different cell sizes have different pore sizes: the larger the cell size, the larger the pore size. Therefore, to investigate the influence of shape and porosity on the permeability and mechanical properties, the cell size T and the porosity ϕ are the key parameters. For a highly efficient and economical experiment plan, as Table 2 and Table 3 show, three factors and three levels for each were considered. For the three factors three level orthogonal array $L_9(3^3)$, the three factors considered were the TPMS architecture, the porosity, and the cell size and, for each factor, there were three different levels: TPMS architecture (Primitive, Gyroid, Diamond), porosity (0.7, 0.5, 0.3), cell size (6, 8, 10 mm). Using this array, only 9 individual experiments instead of 27 were required to obtain the significance of those three factors with respect to the permeability and mechanical properties.

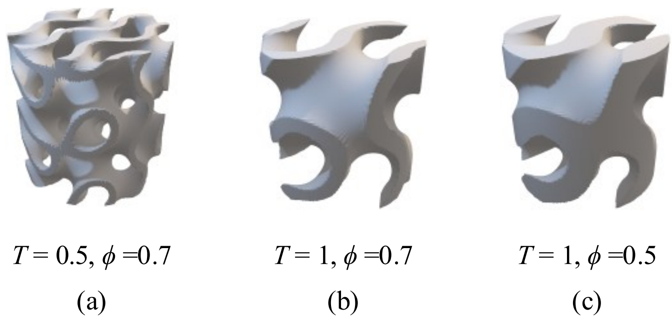

Figure 13. Shell structures for Primitive TPMS with different cell size T and porosity ϕ. (a) cell size T = 0.5, porosity ϕ = 0.7. (b) cell size T = 1.0, porosity ϕ = 0.7. (c) cell size T = 1.0, porosity ϕ = 0.5.

2.3. Hybrid TPMS shell structures

As shown in Fig. 4, instead of directly joining two TPMS structures together, the hybrid TPMS structures give a smooth connection to two TPMS structures and maintains the connection of the pores. Generally, the function for creating an hybrid structure is based on the format below:

$$\Phi_{\text{hybrid}} = \eta\Phi_1 + (1-\eta)\Phi_2 \quad (8)$$

where, Φ_{hybridis} the field function of the hybrid structure, $\Phi 1$ and $\Phi 2$ are the input field functions of structures, which are the implicit function of TPMS structures, and η is the weight function which control the hybrid of two field functions. The simplest function of η is the linear function c:

$$\eta_c(x) = \begin{cases} 0, x < x_1 \\ 1, x > x_2 \\ \frac{x-x_1}{x_2-x_1}, x_1 < x < x_2 \end{cases} \tag{9}$$

where, $\eta_c(x)$ is the linear c function which leads to hybrid TPMS structures along the x direction, x is the x axis coordinates, x_1 and x_2 are the beginning and end coordinates for the hybrid. In this research, only one direction hybrid was investigated, two different TPMS structures were placed along the x direction, which was the hybridization direction.

3. Program for Generating TPMS structures

3.1. Program structure

The program for TPMS structure generation was coded by Python, and the basic program libraries used were VTK and Pyvista for geometry data processes, generation, and visualization. Comparing to previous software, like MSLattice[118], and TPMS Designer[119], this program give more freedom in generating more complex TPMS structures, and supports the generation of hybrid structures, in which two different geometries can be connected smoothly and continuously and, importantly for applications, also maintaining the continuity of the porous channels among the various structures. This program was developed based on classes, and the structure of the program is shown below, it contains core/: for basic geometry structure generation and operation, structure/: for complex geometries, such as TPMS in this research, generation, utils/: additional tools for operational data inputted to and from other softwares, such as ABAQUS.

```
src/
│
├──core/
│  │  GO.py
│  └──GS.py
│
├──structure/
│  │
│  └──tpms/
│      │  BaseTPMS.py
│      └──tpms.py
│
├──utils
│  └──importGS/
└──     └──inp.py
```

Specifically, the core/ section contains the GS.py and GO.py. The GS.py code defines two classes, BaseGS and SimpleGS. BaseGS is the basic class for all geometry structures generated and operated in this program, which defines how the implicit modeling works (see chapter 2.1), how the implicit geometry data is stored and operated, and it also contains functions to convert the implicit modeling result to a .STL format file, and import the .STL format file as implicit modeling data. Then the SimpleGS is the class that inherits from the BaseGS class, in which the basic geometry structures are defined, such as cube, sphere, cone, etc., the geometry structures defined by SimpleGS class are plotted in Fig. 14. The GO.py code contains the hybrid operation to the objects defined by the BaseGS class, and it will be introduced in subsequent chapters.

(a) (b) (c)

Figure 14. Basic geometry structures generated by SimpleGS class. (a) Cube. (b) Sphere. (c) Cone.

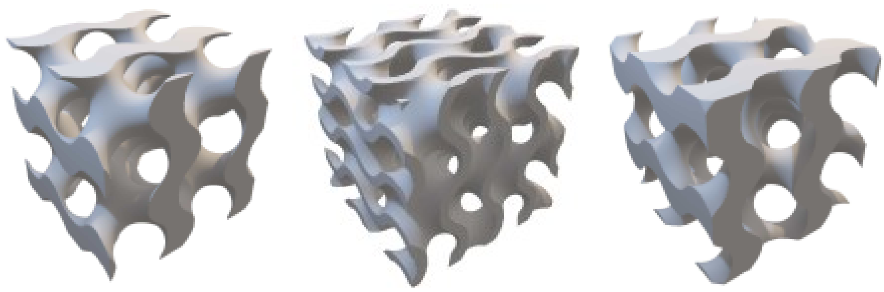

(a) (b) (c)

Figure 15. Gyroid structures. (a) Gyroid positive skeleton. (b) Gyroid shell. (c) Gyroid negative skeleton.

For the structure / section, which contains all complex geometry structures, this requires more complex processes. In this program, which contains two codes for TPMS structures generation: the tpms.py and BaseTPMS.py. BaseTPMS.py stores all basic TPMS structure equations in Table 1. tpms.py is the core code for TPMS structures generation (the method has been presented in Fig. 12), considering the complexity of the whole process, the generation of TPMS structures has been included into a class, named TPMS, that derives from the BaseGS class.Figure 15 shows the Gyroid TPMS structures generated by the TPMS class, with different parameters, besides the shell structure of TPMS, Fig. 15(b) shows the specific domain of skeleton TPMS structures, Fig. 15(a) and (c), can be generated depending on the applications. Meanwhile, the TPMS class can directly generate TPMS structures with specific porosity, and Fig, 16 shows Gyroid TPMS structures with different porosity values.

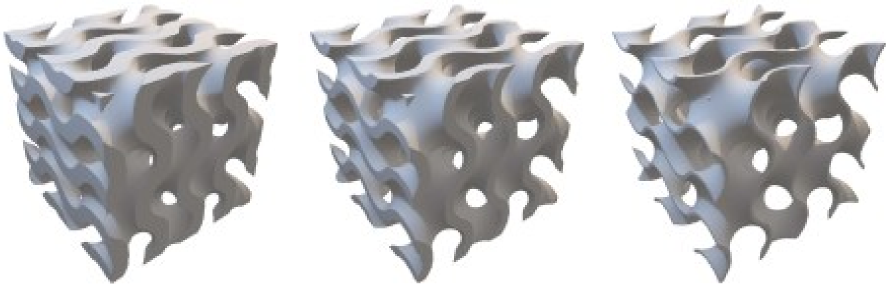

(a) (b) (c)

Figure 16. Gyroid TPMS structures with different porosity values. (a) Porosity = 0.5. (b) Porosity = 0.7. (c) Porosity = 0.9.

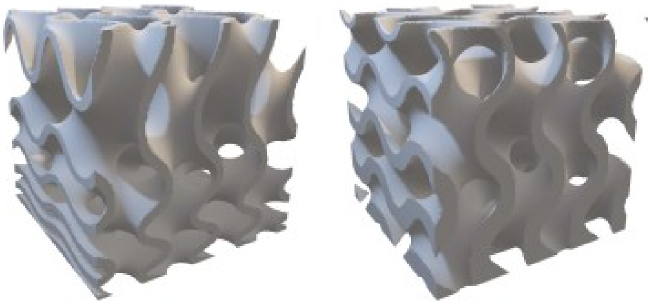

(a) (b)

Figure 17. Gradient Gyroid TPMS structures. (a) Gradient by changing cell size. (b) Gradient by changing shell thickness.

Besides controlling the porosity of TPMS structures, considering the properties of TPMS shown in Fig. 13 and Equation 7, the program can generate gradient TPMS structures by changing the cell size T and offset value c for structures, see Fig. 17, where Figure 17(a) is the gradient TPMS structure whose cell size increases gradually along the height direction, and Fig. 17(b) shows the gradient TPMS structure whose thickness decreases gradually along the height direction. For different applications, those two gradient methods provide different options.

3.2. Geometry structure operation

For simple applications, the BaseGS class generated above can generally meet the requirements but, for complex structures generation, additional geometry operations are essential. In this subchapter, the Boolean and Hybrid geometry operations will be presented.

3.2.1. Boolean

The mathematical principles of Boolean operations have been stated in chapter 2.1, and in the program, it supports the importing of a geometry structure (see Fig 18(a)) that becomes the boundary intersecting the Boolean operation with the simple Gyroid TPMS structure (see Fig 18(b)). The final TPMS structure after the Boolean operation is shown in Fig 18(c), where the Boolean operation and the TPMS structure can be applied according to the geometry boundary conditions.

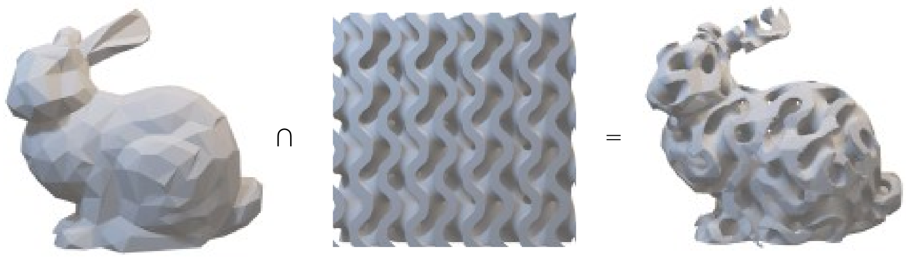

(a) (b) (c)

Figure 18. Complex TPMS structure generation via Boolean operation. (a) input geometry. (b) Simple Gyroid TPMS structure. (c) Gyroid structure after intersecting Boolean operation.

3.2.2. Hybrid structures

The mathematical principles of hybrid operations have been described in chapter 2.3, which is function GO.py under core/ path. Typically, the hybrid operation can mix two completely different structures smoothly, Fig. 19 shows the hybrid of a cube to a cylinder from left to right. The area of the hybrid structure can be controlled by giving different parameters to the GO.py function. Fig. 19(a) shows a fully hybridized structure, while and Fig. 19(b) shows a structure where only a limited area of it has been hybridized.

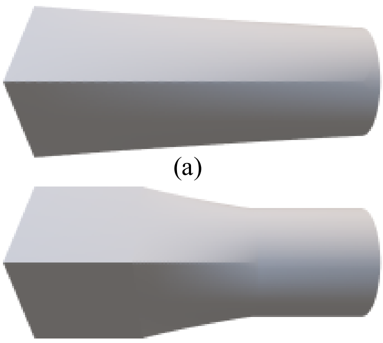

(a)

(b)

Figure 19. Cube to cylinder hybrid structure obtained by using different parameters. (a) Full hybrid. (b) Localized hybrid.

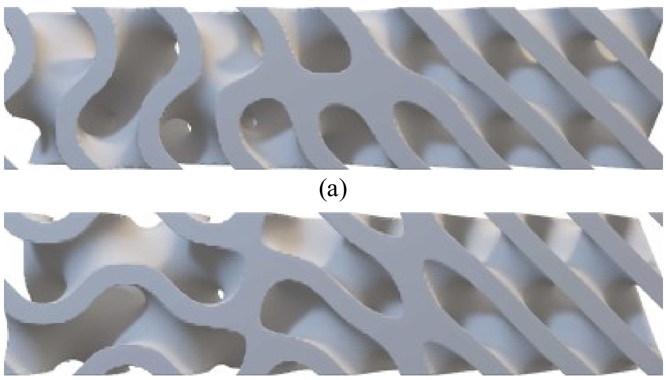

(a)

(b)

Figure 20. A hybrid TPMS structure. (a) Top view. (b) Front view.

For TPMS structures, the hybrid operation is more versatile, because it allows not only to obtain smooth surfaces, but also to achieve the continuity of pores from the two structures, providing advantages in mechanical and permeability applications. Fig. 20 shows the local hybrid of the Gyroid and Diamond structures from left side to right side, Fig. 20(a) is the top view of the hybrid structure, and Fig. 20(b) is the front view of the hybrid structure. It is clear that, with the hybrid operation, the Gyroid and Diamond structure can connect smoothly and the porosity is also well and fully connected.

3.3. Connection with FEM

Besides all functions described previously, the program also supports importing ABAQUS simulation results for shape optimization. Fig. 21 shows the stress field of a simulation, and the ABAQUS supports the export simulation results (e.g., stress, strain, etc.) as a .CSV file, in which all simulation results are stored node by node. By reading this file, the program can use the simulation result field to generate complex and optimized structures for a specific application.

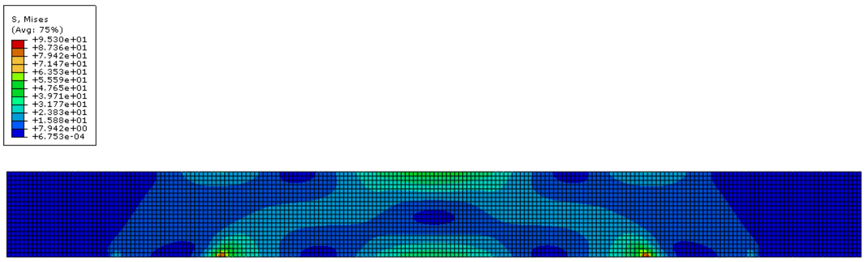

Figure 21. The input stress field from ABAQUS simulation.

In this program, the function inp.py under utils/importGS/ path support for the operation above, which can import the ABAQUS simulation result as a BaseGS object, and then use geometry operation functions mentioned above to generate structures. To perform light weight design using the stress field, Fig. 21, from numerical simulation, the process begins with a finite element analysis (FEM) of the original structure under given loading and boundary conditions. The resulting stress field distribution is then extracted, providing a detailed path of how mechanical loads are carried throughout the structure.

Regions with high stress values indicate critical load bearing paths and should be preserved to maintain structural integrity, and regions with low stress mean less mechanical demand and can allow for material removal or replacement TPMS structures. The critical stress value to recognize the region as a high or low stress value is the threshold for light weight. Fig. 22(a)-(c) give the different light weight designs with different threshold values with Gyroid structures infill. The higher the threshold value is, the more regions of the original beam are filled with the Gyroid structures, and generally, the lower stiffness and strength the light weighted beam will have. In application, the critical stress should be defined according to different design targets and constraints, e.g., target stiffness, allowed strength, allowed displacement, and safety factor, and the light weight structures need to be re-simulated under the same loading and boundary conditions to verify the new stress field distribution.

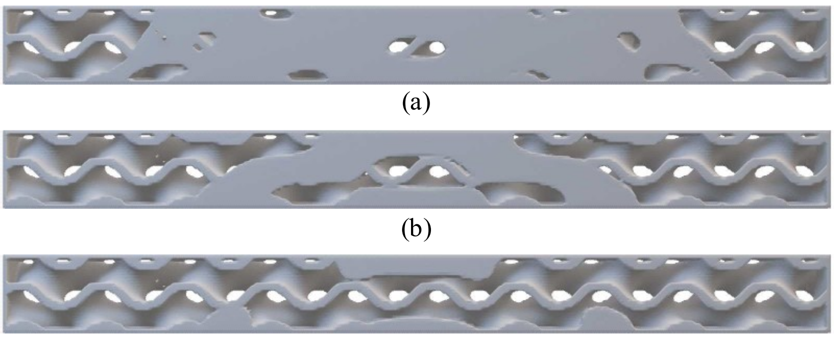

(a)

(b)

(c)

Figure 22. Light weighting structures filled with TPMS. (a) Stress threshold is 10 MPa. (b) Stress threshold is 15 MPa. (c) Stress threshold is 20 MPa.

4. Orthogonal experimental design for the evaluation of the permeability and mechanical properties of TPMS structures

When designing TPMS structures that need to meet specific requirements for permeability and mechanical properties, it is of great significance to investigate the influence of different factors of the TPMS structures (such as TPMS architecture, porosity, and cell size) on their permeability and mechanical properties. In this chapter, three kinds of TPMS architectures, Primitive, Gyroid and Diamond, with different porosity and cell size were manufactured in both PLA and zirconia, based on an orthogonal experimental design, to investigate the influence of those factors on their permeability (Darcy permeability coefficient k_1 and Forchheimer coefficient β) and mechanical properties (Young's modulus and energy absorption). All specimens were tested by permeability tests and uniaxial compression tests to measure the experimental data on permeability and mechanical properties. Meanwhile, numerical simulations were conducted using Fluent and Abaqus. Finally, a range analysis method was employed to determine the primary factor on permeability and mechanical properties.

4.1. Set up of experiments and numerical simulations

4.1.1. TPMS structures and materials

Orthogonal experimental design is a method that uses a suitable orthogonal table for the guidance of experiment design. It uses statistical analysis, such as range analysis, to find how different factors affect the results [120]. With this method, when many factors may affect the results, it helps researchers find the significance of each factor quickly. It also reduces the number of experiments needed.

Table 2. Levels and factors for the orthogonal experiment.

Levels	Factors		
	TPMS architecture	Porosity	Cell size (mm)
1	Primitive	0.7	6
2	Gyroid	0.5	8
3	Diamond	0.3	10

Table 3. Three factors three levels orthogonal table $L_9(3^3)$.

Sample Label	TPMS architecture	Porosity	Cell size (mm)
P_u8p07	Primitive	0.7	8
P_u10p05	Primitive	0.5	10
P_u6p03	Primitive	0.3	6
G_u6p07	Gyroid	0.7	6
G_u8p05	Gyroid	0.5	8
G_u10p03	Gyroid	0.3	10
D_u10p07	Diamond	0.7	10
D_u6p05	Diamond	0.5	6
D_u8p03	Diamond	0.3	8

For both permeability and mechanical properties experiments, all samples were cylinders with the same dimensions (diameter D = 18 mm, length L = 20 mm). PLA samples were printed using a 3D printer (Ender-3, Creality, China) and a PLA filament (SUNLU, China), a temperature of 200°C, a printing speed of 50 mm/s, a nozzle size of 0.4 mm and a slicing layer height of 0.2 mm (see Fig. 23(a)). Figure 23(b) shows the samples listed in Table 3.

(a) (b)

Figure 23. PLA specimens. (a) the printing of a PLA specimen. (b) PLA specimens for all 9 orthogonal experiments.

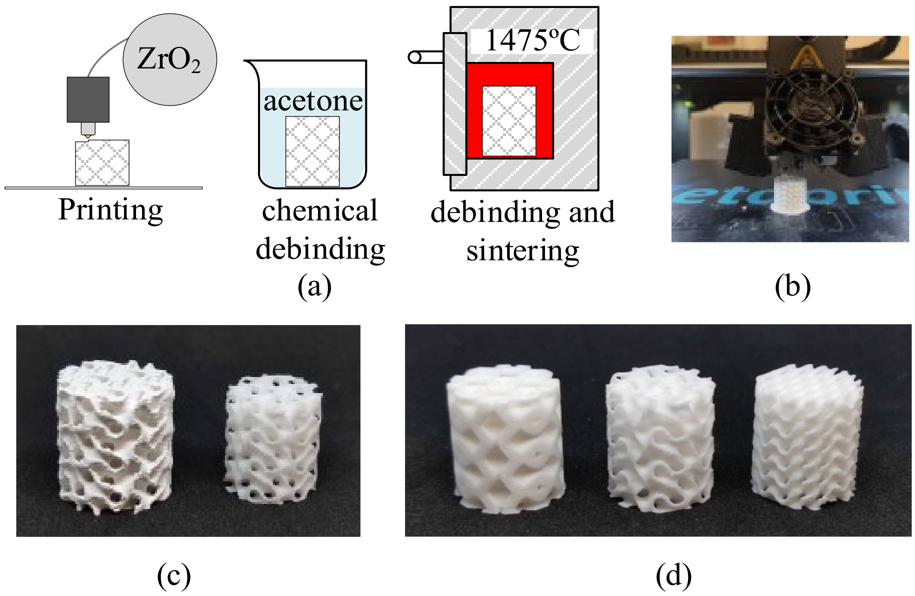

Figure 24. Zirconia specimens. (a) procedure for manufacturing a zirconia specimen. (b) the printing of a zirconia specimen. (c) the shrinkage of zirconia specimens before and after sintering. (d) zirconia specimens for experiments.

Zirconia samples were also manufactured by FDM, for ceramic TPMS structures with larger unit cell sizes, printing the overhanging structures with a zirconia filament is particularly challenging, due to the inability to use support structures, which limits manufacturability. Therefore, only models with a cell size T = 6 mm were produced. As Table 4 shows, is all parameters of the white zirconia filament (Zetamix, France) for zirconia samples fabrication, a temperature of 180°C, a printing speed of 15 mm/s, a nozzle size of 0.4 mm, the build plate does not need to be heated to increase the adhesive of the green bodies while printing and a slicing layer height of 0.2 mm (see Fig. 24(a,b)).

Table 4. Parameters of zirconia sample fabrication.

Material	Zirconia ($ZrO_2 \cdot Y_2O_3$)
3D Printing temperature	180°C
Build plate temperature	No heating
Filament diameter	1.75 mm
Nozzle size	0.4 mm
Layer height	0.2 mm
3D printing speed	15 mm/s
Wall line count	Print wall only
infill density	100%
Supports structure	No
Chemical debinding temperature	40°C
Chemical debinding solver	Acetone
Chemical debinding duration	12 h
Chemical debinding weight lose	>5%
Thermal debinding temperature	20 to 500°C, 8°C /h
Sintering temperature	20 to 1475°C, 50°C /h, holding 2h, 1475 to 20°C, 100°C /h
Linear Shrinkage after sintering	21.5% ±1%

After printing, the samples were placed in acetone for 12 hours at 40°C, losing 5 wt% due to the chemical debinding and, after that, following the recommendation from the producer, they were inserted in a muffle furnace for thermal debinding in air (from 20 to 500 °C with heating rate 8°C/h), and then sintered at 1475°C for 2 h, with a heating rate of 50°C/h. After sintering, the samples underwent a 21.5% linear shrinkage (Fig. 24 (c)), and this was taken into account by printing oversized samples to achieve the desired correct final size previously specified, after sintering. Fig. 24 (d) shows the zirconia samples prepared for the tests.

The X-ray Diffraction (XRD) result of a zirconia sample in this research is given in Fig. 25. The XRD pattern shows that this is a yttria-stabilized zirconia material as the producer mentioned in the technical datasheet, with a series of sharp and intense reflections located at 2θ ≈ 30°, 35°, 50° and 60°, which are characteristic of the tetragonal zirconia phases. No significant splitting of peaks near 28–31° was observed, indicating that the monoclinic phase is largely suppressed. This confirms that the addition of Y_2O_3 effectively stabilizes the high-temperature tetragonal structures at room temperature.

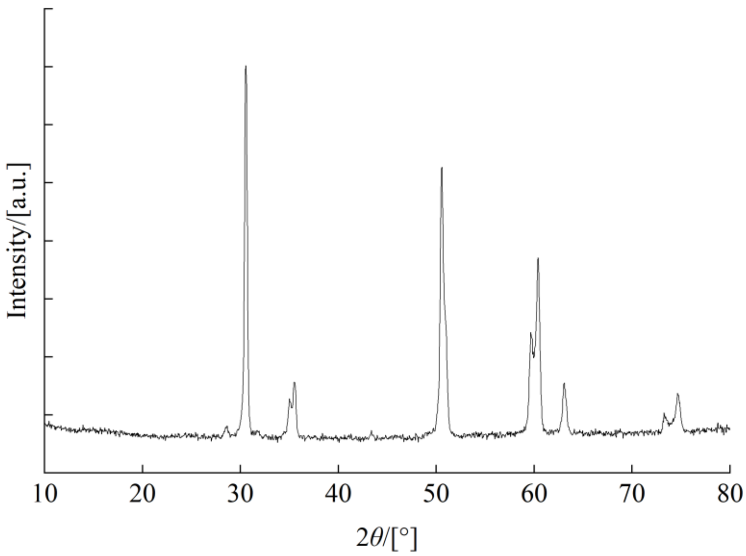

Figure 25. XRD pattern of a zirconia sample.

4.1.2. Permeability experiments and simulations

The set-up of the permeability test experiment is shown in Fig. 26 [121, 122], and it contains a chamber, the sample, a flow rate meter, a pressure drop sensor, gas tubes, an adapter, and a computer. As a chemically inert, non-toxic and dry gas, nitrogen was selected as the test gas. When carrying out the gas flow experiments, a sample was fixed in the center of the chamber, with nitrogen flowing through it, at both the inlet and outlet sides of the chamber there was a gas tube connected to the pressure drop sensor and, at the outlet side of the chamber, the flow rate data were collected by a digital flow rate meter. All pressure drop and flow rate data were collected by the self-developed software with computer via the adapter, for more details about set up of the software please check the Appendix A. For all samples, the gas flow was slowly increased from 0 L/min to 50 L/min.

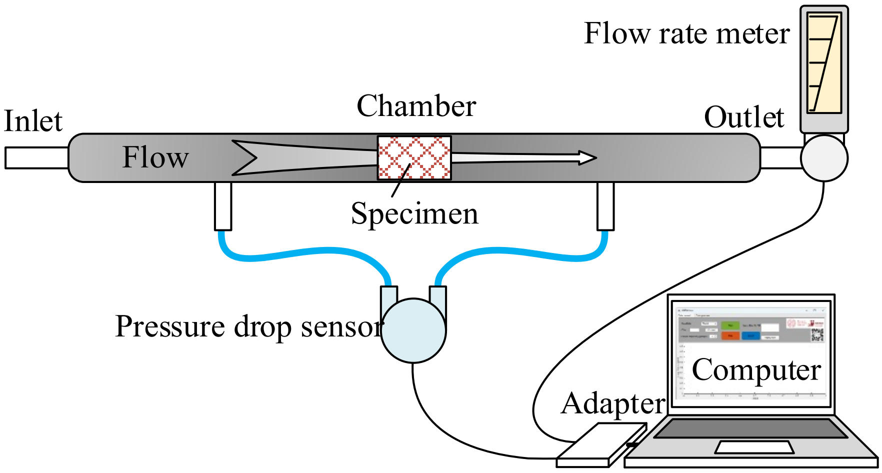

Figure 26. Permeability tests experimental set-up.

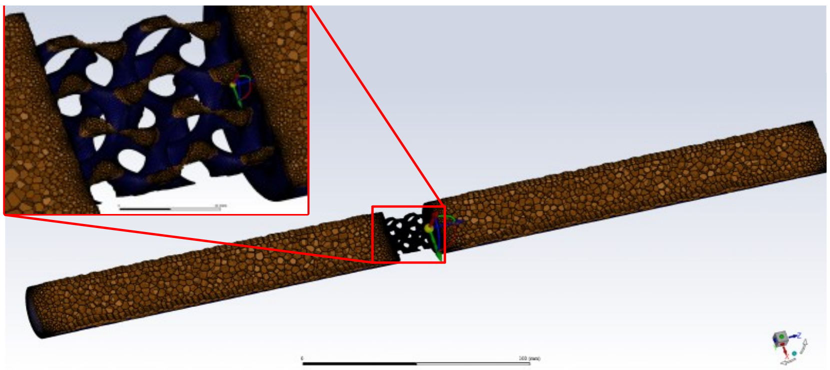

Figure 27. The simulation model mesh in Fluent.

The simulations for the permeability were conducted by Ansys Fluent using a minimum mesh size within the area of the TPMS structure of 0.1 mm, and 5 mm for other areas, with a boundary layer number of 3, using nitrogen as the fluid (the density ρ and viscosity μ are given in Table 5). Figure 27 shows the simulation model mesh in Fluent, the dimensions of the model were the same as those of the experimental chamber (diameter 18 mm for TPMS area, and 25 mm for other areas), and at the inlet side was placed the mass flow boundary condition, where the corresponding flow rate value varied from 0 L/min to 50 L/min, and at the outlet side was the pressure condition at the value of 0 Pa.

Table 5. Properties of the fluid.

Fluid	Density ρ kg/m^3	Viscosity μ Pa s
Nitrogen	1.18029	1.8301×10^{-5}

Table 6. Geometric surface area and Reynolds number Re_{TPMS} for each sample.

Sample label	Geometric surface area S (mm^2)	Reynolds number Re_{TPMS}
P_u8p07	1.92	4.40×10^5
P_u10p05	1.64	5.15×10^5
P_u6p03	2.20	3.84×10^5
G_u6p07	3.23	2.62×10^5
G_u8p05	2.50	3.38×10^5
G_u10p03	1.99	4.25×10^5
D_u10p07	2.52	3.35×10^5
D_u6p05	3.74	2.26×10^5
D_u8p03	2.66	3.18×10^5

Concerning the Fluent simulation of the TPMS structures, the Reynolds number Re_{tpms} for this kind of porous structures can be calculated taking into account the porosity ϕ [123]:

$$Re_{\mathrm{TPMS}} = \frac{D_{\mathrm{TPMS}} u \rho}{\mu \phi} \quad (10)$$

where, u is the velocity, equal to the flow rate divided by the section area of the model, ρ and μ are the density and viscosity of the fluid, respectively, and D_{TPMS} is the hydraulic diameter of the TPMS structures, given by:

$$D_{\mathrm{TPMS}} = \frac{4\phi}{S} \quad (11)$$

where, S is the geometric surface area.

For each sample in Table 3, the geometric surface area S and Re_{TPMS} can then be calculated, as reported in Table 6. The turbulence model k-epsilon is the suitable model for the simulation and, considering that the TPMS model contains several small pores, the standard wall function was applied to simulate the fluid flow near the wall.

4.1.3. Compression tests and simulations

The compression tests were carried out using a uniaxial testing machine (Quasar 25, Galdabini, Cardano, Italy), applying Vaseline to the contact area between the sample and the plates to reduce friction with the steel plates. The loading speed was 2 mm/min, and the test was ended when reaching a target displacement value (10 mm for PLA samples and 2 mm for zirconia) or when the loading force dropped to 0 N. The data reported represent the average of 2 individual tests.

The simulations of PLA TPMS structures deformation under uniaxial compression loading were conducted by Abaqus, and Table 7 gives the adopted material properties for PLA (the data were obtained by directly testing the material).

Table 7. Material properties for PLA.

Young's modulus MPa	Poisson's ratio	Strength MPa	Density kg/m^3
1000	0.3	55	1,230

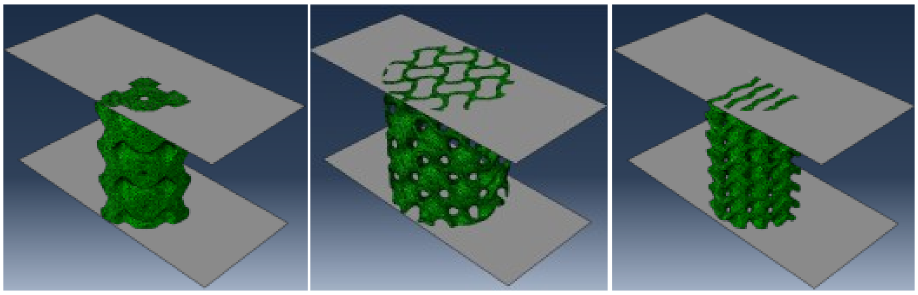

(a) (b) (c)

Figure 28. Model of TPMS samples. (a) Primitive: P_u6p03. (b) Gyroid: G_u6p07. (c) Diamond: D_u6p05.

Fig. 28 (a)-(c) show the models of Primitive, Gyroid, and Diamond TPMS structures, which were all meshed by a tetrahedral mesh and, to save CPU time, the symmetry parts of the Primitive and Diamond structures were simplified to the quarter models (see fig. 28 (a) and (c)). As Fig. 28 (a)-(c) show, the TPMS sample was placed between two planes which are all analytical rigid parts, and all parts were set as general contact with the properties of a hard contact. For the boundary conditions and loading, all degrees of freedom for the bottom plane were fixed, the displacement loading was carried out along the axial direction of the TPMS sample from the top plane, the displacement loading increased from 0 mm to 10 mm, and for the top plane all degrees of freedom except the loading direction were fixed.

The simulations were all conducted using an Explicit/Dynamic solver and, for the quasi-static loading simulations in accordance with the ABAQUS manual [124], the loading rate should not be smaller than 10 times of the first natural period for the TPMS structure, i.e.:

$$t_{min} > 10/f_1 \tag{12}$$

where t_1 is the minimum time defined by natural frequency, f_1 is the first natural frequency of the structure, and the values for the TPMS structures are reported in Table 8. Then the minimum time t_1 can be estimated by:

$$t_{min} > 10/f_{1\_max} = 10/19{,}643 = 5.1 \times 10^{-4} s \tag{13}$$

In this work, for all simulations, the time t was set as 1×10^{-3} s.

Table 8. The first natural frequency for all TPMS structures.

Sample label	First natural frequency (Hz)
P_u8p07	13,329
P_u10p05	16,354
P_u6p03	19,595
G_u6p07	8,643
G_u8p05	9,505
G_u10p03	10,799
D_u10p07	16,675
D_u6p05	19,643
D_u8p03	15,794

The minimum stable time increment Δt is:

$$\Delta t = L_e/c_d = L_e/\sqrt{E/\rho} = 4.4 \times 10^{-7} s \tag{14}$$

where L_e is the characteristic element length, c_d, E, and ρ are the dilatational wave speed, Young's modulus and density for the material, respectively. Then, with the simulation time t and minimum stable time Δt, the amount of steps $N = t/\Delta t$ was 2272, which is an acceptable number for simulations, so mass scaling was disabled for all simulations.

In this chapter, both PLA and zirconia samples were scanned using a metrological micro-focus X-ray CT system (XCT, MCT225, Nikon Metrology, UK) to evaluate the influence of sample architecture on the permeability and mechanical properties. The analysis was carried out in the laboratory of Prof. Simone Carmignato, Department DTG, University of Padova.

4.2. Permeability and mechanical properties results

4.2.1. Permeability properties

The pressure drop between the inlet side and outlet side of the samples and the nitrogen flow rate data were all recorded (see Fig. 26), for further analysis, the flow rate data was converted to the fluid flow velocity data:

$$u = \frac{Q}{\pi(D/2)^2} \tag{15}$$

where, u is the fluid flow velocity, Q is the flow rate recorded by the flow rate meter, D is the diameter of sample.

The fluid flow velocity – pressure drop results from the permeability experiment carried out on PLA samples, together with the Fluent simulation for all cases in

Table 3, are shown in Figs. 29 (a)-(c) (the legends ending with _s mean that the results come from the Fluent simulation).

As the figures highlight, the pressure drop data presents a nonlinear relationship with the fluid flow velocity, and it can be described by Forchheimer's equation:

$$-\frac{\Delta P}{L} = \frac{\mu}{k_1} u + \rho \beta u^2 \tag{16}$$

where, ΔP is pressure drop between the two sides of the sample, L is the length of the sample, k_1 is the Darcy permeability of the structure, characterizing viscous resistance, β is the Forchheimer coefficient, reflecting inertial resistance due to high-velocity flow. The minus symbol at the left term of the equation means that the direction of the pressure drop gradient is opposite to the direction of the fluid flow velocity [52,125].

We can observe, from Figs. 29 (a)-(c), that the experiment results are consistent for all the different specimens, and that the Fluent simulation results match rather well with the corresponding experimental data. The matching is better at lower fluid flow velocity (1.0 m/s) than at higher fluid flow velocity, meaning that when fluid flow velocity is low, the viscous resistance in Equation 16 dominates the fluid flow, and Fluent can simulate this condition well. Concerning the different TPMS architectures, the Gyroid structure's simulation shows a better match with the experimental data than that for the other two structures, with the Fluent results for the D_u8p03 case (the sample with the smallest cell size and lowest porosity) showing the worst results (see Figs. 29 (c)). The pressure drop values were significantly larger than the experimental data when fluid flow velocity was larger than 1.5 m/s, this error is mainly due to the inability to accurately simulate the attrition between the fluid and the solid wall due to the narrow fluid channels under high-speed flow.

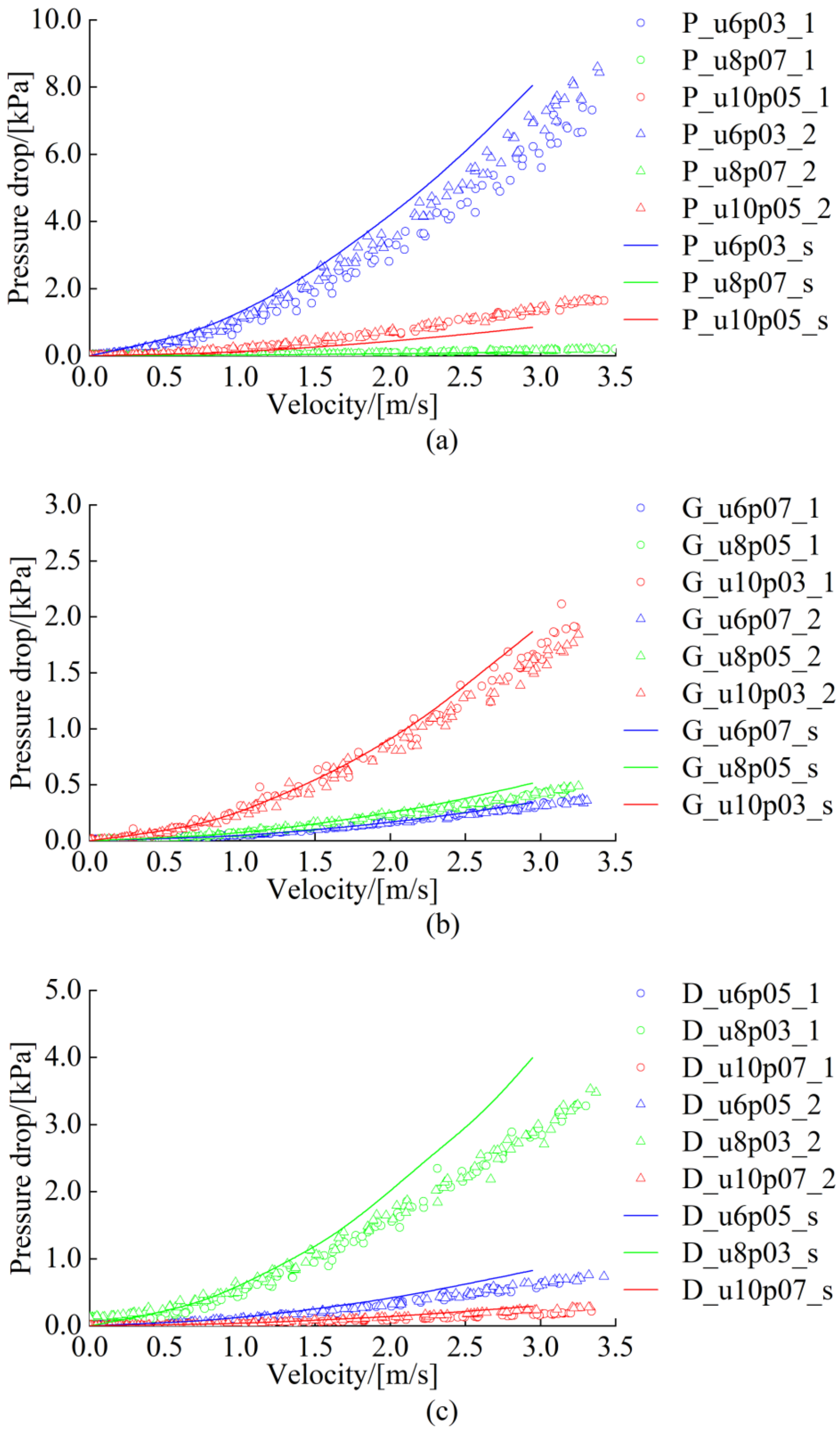

Figure 29. Fluid flow velocity - pressure drop results of simulations and experiments of PLA samples. (a) Primitive structures. (b) Gyroid structures. (c) Diamond structures.

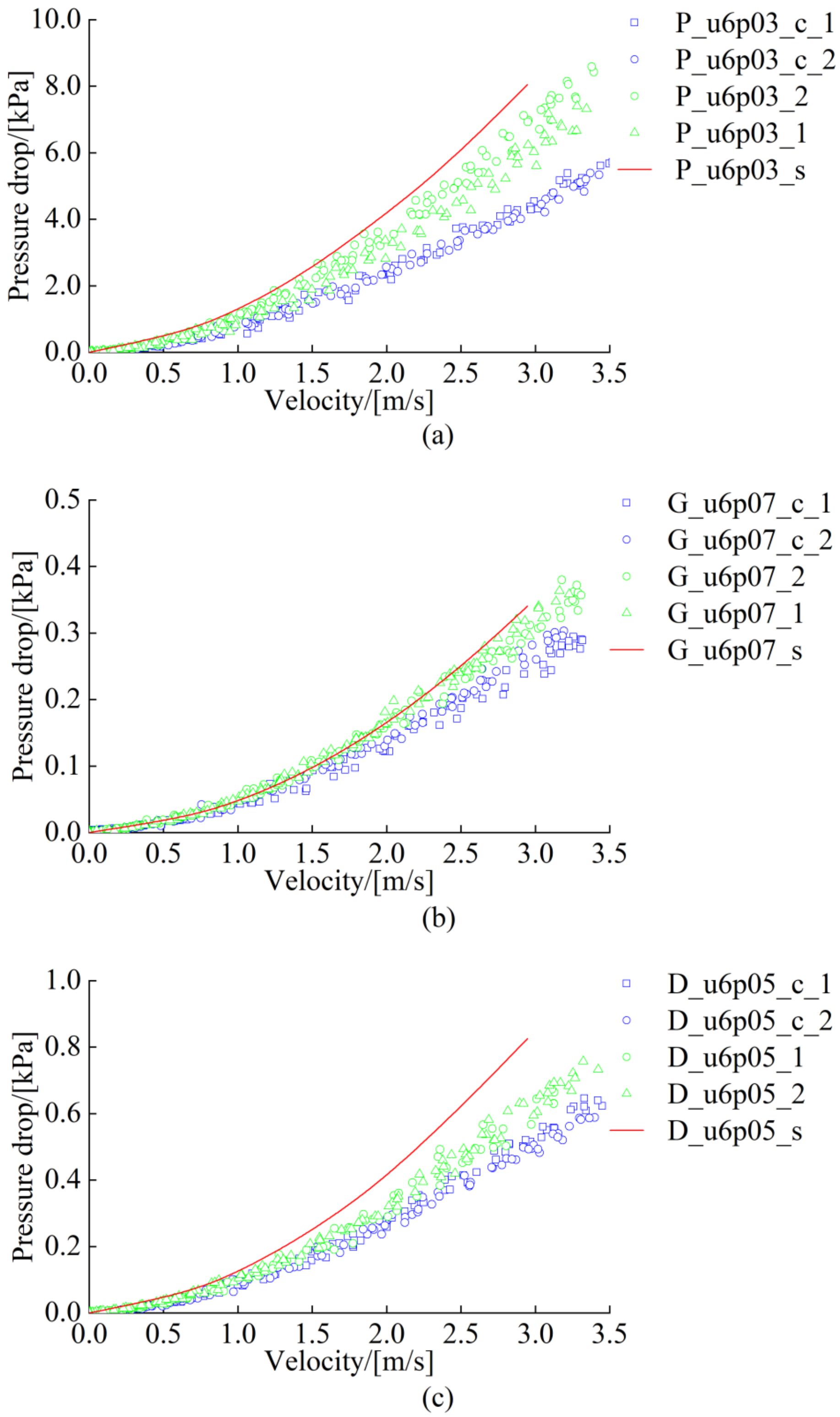

Figure 30. Zirconia samples data (blue scatter), PLA samples data (green scatter), and Fluent simulation results (red curves) comparison. (a) Primitive structure P_u6p03. (b) Gyroid structure G_u6p07. (c) Diamond structure D_u6p05.

For zirconia samples, the permeability experiment results are reported in Figs. 30(a)-(c), where the lines are the Fluent simulation results, and the points which a legend containing _c_ are the data from the zirconia samples tests, while the other ones are the data from PLA samples tests. Comparing the data for PLA and zirconia samples, we can observe that the data for the zirconia samples show less scatter, and it is clear that all pressure drop data of zirconia samples are lower than those for PLA samples at the same fluid flow velocity. Fig. 31 reports the 3D reconstruction of both P_u6p03 PLA and zirconia samples, which were scanned by XCT. By overlapping these data and checking the porous section where the fluid flows, we observed that the minimal pore size of the zirconia sample was larger than that of the PLA sample (0.44 mm with respect to 0.10 mm, respectively). We posit that it is this difference that makes the pressure drop of zirconia samples smaller than measured for the PLA samples. Similarly to what previously discussed, the experimental data for the Gyroid structures showed again the best matching with the simulation, independently on the material of which the samples are comprised of.

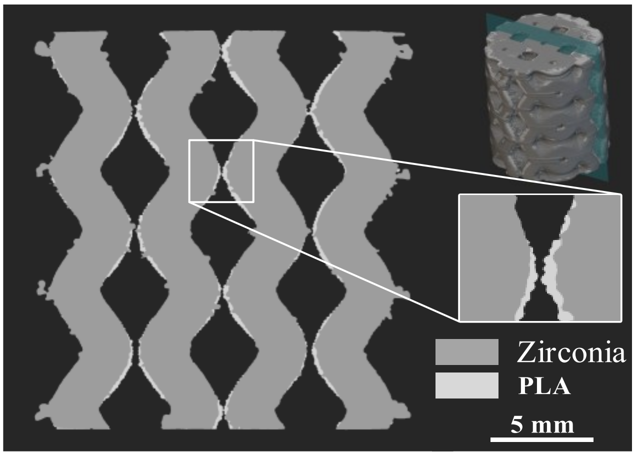

Figure 31. Comparison of the minimal pore size of the zirconia and PLA samples from the XCT sections.

Figure 32 shows the fitting procedure for the P_u6p03 sample data, and the fitting function based on a quadratic polynomial with zero intercept:

$$y = B_1 x + B_2 x^2 \tag{17}$$

With Equations 16 and 17, the Darcy permeability coefficient k_1 and the Forchheimer coefficient β can be calculated by:

$$\begin{cases} k_1 = L\mu/B_1 \\ \beta = B_2/\rho L \end{cases} \tag{18}$$

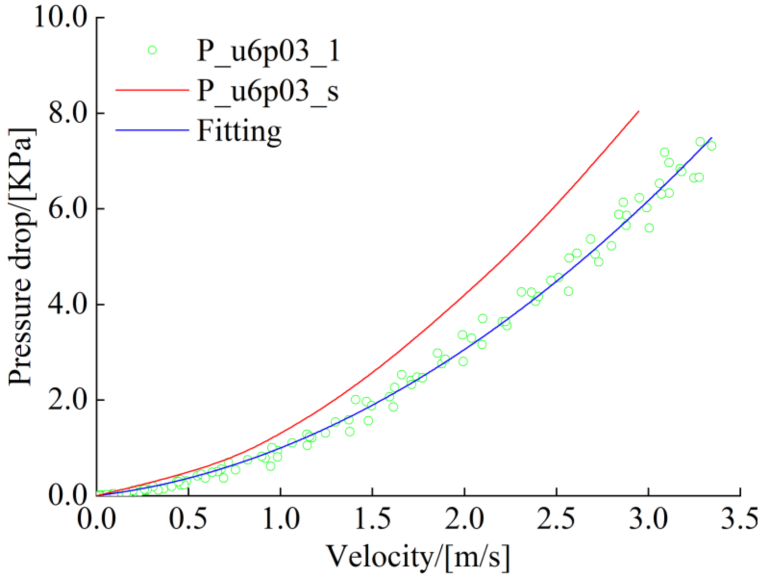

Figure 32. Fitting of the data for the Primitive structure P_u6p03_1 sample.

For all PLA and zirconia samples, the Darcy permeability coefficient k_1 and Forchheimer coefficient β can be calculated by Equation 18, and Table 9 and 10 report the Average, Standard Deviation (std), and Coefficient of Variation (CV) of the two results. The CV is a useful measure to assess the consistency of experimental data. For the PLA samples, the CV values of k_1 and β were all low, with maximum values of 0.19 (k_1 for model D_u8P03) and 0.21 (β for D_u10p07). Similarly, the CV values for k_1 and β in the zirconia samples were also low, with maximum values of 0.07 (k_1 for P_u6p03_c) and 0.09 (β for G_u6p07_c). These low CV values demonstrate good consistency across all tested PLA and zirconia samples. Meanwhile, for both PLA and zirconia samples, the experimental data within the same cases are enclosed by yellow rectangles in Fig. 33, and this shows that only a small difference exists for their Darcy permeability coefficient k_1 and Forchheimer coefficient β. Specifically, the Darcy permeability coefficient k_1 values of the PLA and zirconia samples were in good agreement and, for the Forchheimer coefficient β for the P_u6p03 structure, the difference between the PLA and the zirconia samples was the largest.

Table 9. Darcy permeability coefficient k_1 and Forchheimer coefficient β Average, Standard Deviation (std), and the Coefficient of Variation (CV) for all PLA samples.

Sample label	k_1 (10^{-8}m^2)			β (10^2 m^{-1})		
	Average	std	CV	Average	std	CV
P_u8p07	2.87	0.25	0.09	5.79	0.13	0.02
P_u10p05	0.36	0.01	0.03	51.36	0.54	0.01
P_u6p03	0.07	0.01	0.14	232.95	9.16	0.04
G_u6p07	1.33	0.12	0.09	11.09	0.78	0.07
G_u8p05	0.87	0.07	0.08	13.85	0.21	0.02
G_u10p03	0.27	0.01	0.05	59.75	3.75	0.06
D_u10p07	1.90	0.02	0.01	6.93	1.47	0.21
D_u6p05	0.68	0.05	0.07	21.76	0.34	0.02
D_u8p03	0.10	0.02	0.19	86.71	10.38	0.12

Table 10. Darcy permeability coefficient k_1 and Forchheimer coefficient β Average, Standard Deviation (std), and the Coefficient of Variation (CV) for all zirconia samples.

Sample label	k_1 (10^{-8}m^2)			β (10^2 m^{-1})		
	Average	std	CV	Average	std	CV
P_u6p03_c	0.07	0.005	0.07	137.03	7.67	0.06
G_u6p07_c	1.41	0.05	0.03	8.73	0.78	0.09
D_u6p05_c	0.66	0.01	0.01	16.41	0.84	0.05

The Average results and the Coefficient of Variation between the two different materials are reported in Table 11. The Coefficient of Variation between PLA and zirconia for k_1 was between 0.02-0.03, while the value was about 0.12, 0.14 and even 0.26 (P_u6p03) for β. This indicates that when fluid flow follows Darcy's law, the permeability behavior is primarily dominated by the sample structure rather than by their material composition, and additive manufacturing techniques can produce samples possessing a good consistency in terms of permeability characteristics.

Table 11. The Coefficient of Variation (CV) for the Darcy permeability coefficient k_1 and for the Forchheimer coefficient β for PLA and zirconia samples.

Sample label	k_1 (10^{-8}m^2)			β (10^2 m^{-1})		
	PLA	Zirconia	CV	PLA	Zirconia	CV
P_u6p03	0.07	0.07	0.03	232.95	137.03	0.26
G_u6p07	1.33	1.41	0.03	11.09	8.73	0.12
D_u6p05	0.68	0.66	0.02	21.76	16.41	0.14

The Darcy permeability coefficient k_1 and the Forchheimer coefficient β results with error bar for the PLA and zirconia samples are reported in Fig. 33. The scatter plot shows a strong clustering behavior between experimental data points within the same case (see Table 3), and the datapoints can be further grouped into larger clusters according to the corresponding porosity value. As Fig. 33 shows, all experimental data can be grouped into three clusters within three black rectangles. For all porosity $\phi = 0.3$ cases, the Darcy permeability coefficient k_1 was lower than 0.3×10^{-8} m^2, for all porosity $\phi = 0.5$ cases, the Darcy permeability coefficient k_1 was higher than 0.3×10^{-8} m^2 and smaller than 1.0×10^{-8} m^2, and for all porosity $\phi = 0.7$ cases, the Darcy permeability coefficient k_1 was higher than 1.0×10^{-8} m^2. Generally, The Darcy permeability coefficient k_1 shows a positive correlation with the porosity parameter, as higher porosity means more/larger fluid channels and lower viscous resistance. In contrast, the Forchheimer coefficient β is inversely proportional to porosity, as lower porosity increases inertial losses due to tortuous and narrow flow paths.

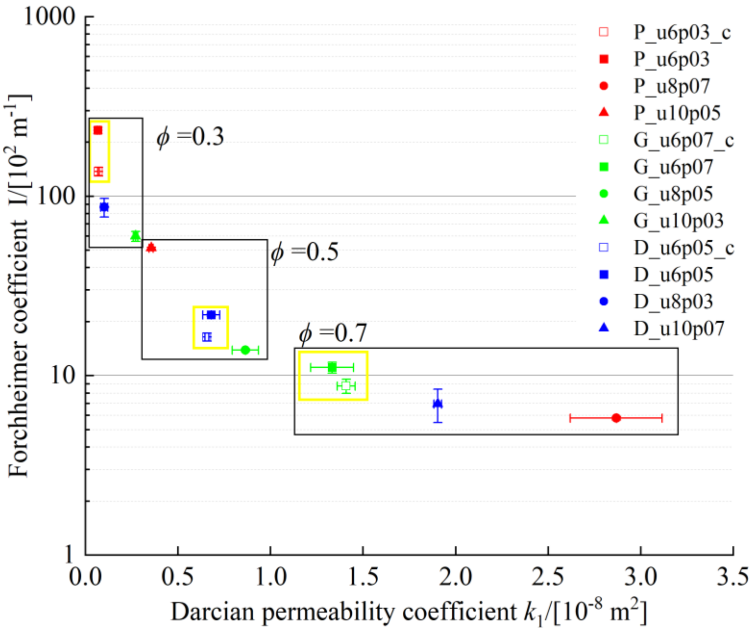

Figure 33. Relationship between the Darcy permeability coefficient k_1 and Forchheimer coefficient β.

4.2.2. Mechanical properties

Figure 34(a) reports the displacement-loading force experimental data and simulation curves for the P_u6p03 sample, generated with a mesh size of 0.4, 0.6, and 0.8 mm, As the mesh density increases, the discrepancy between the numerical simulation results and the experimental data decreases, and the difference between the results of the 0.6 mm and 0.4 mm mesh sizes becomes minimal, indicating that the solution has nearly converged, for the balance between accuracy and computing resources, the selected element size for simulation was 0.4 mm. Meanwhile, the adequacy of all settings concerning the quasi-static explicit/dynamic simulation can be checked by the ratio between the kinetic energy (KE) and the internal energy (IE), which is shown in Fig. 34(b), according to the manual of ABAQUS [124], as the ratio KE/IE remains below 10 %, for this simulations, the kinetic energy is a very small fraction of the internal energy.

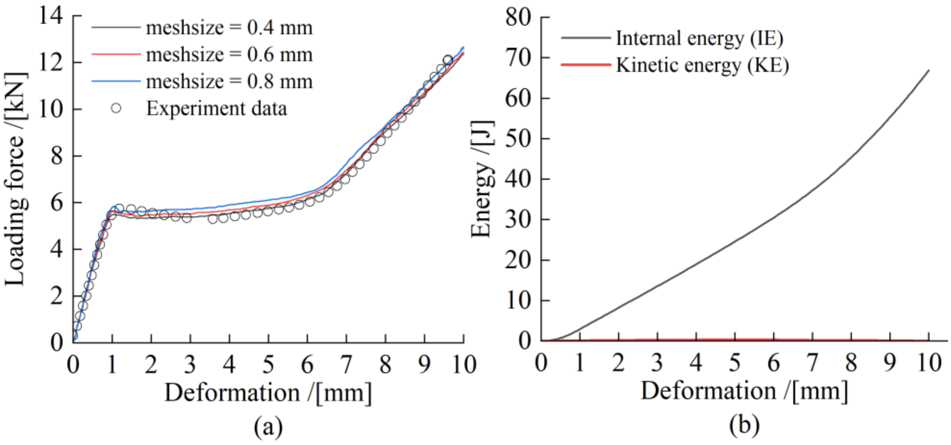

Figure 34. (a) Displacement-loading force experimental data and simulations curves for the P_u6p03 sample, obtained with different mesh sizes. (b) the energy-deformation curves for the kinetic energy (KE) and the internal energy (IE).

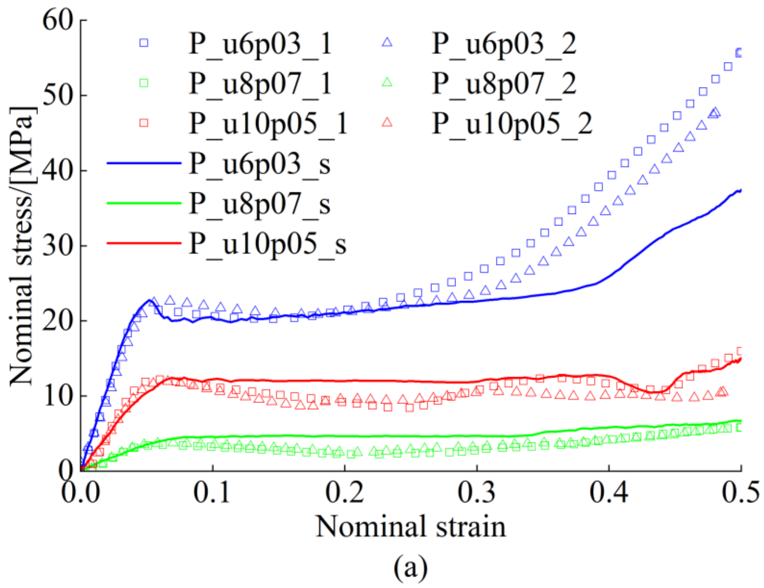

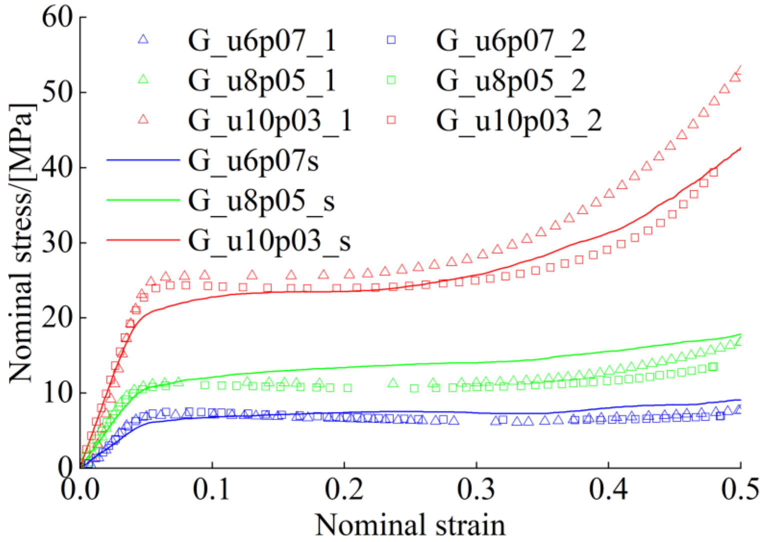

(b)

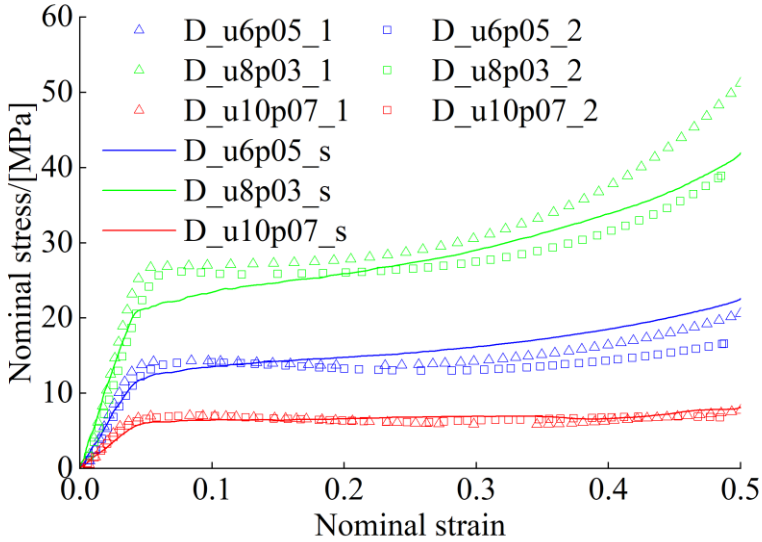

(c)

Figure 35. Load-deformation for PLA experimental results and simulations. (a) Primitive structures. (b) Gyroid structures. (c) Diamond structures.

The experimental data and the simulations for the compression tests on the PLA samples are reported in Figs. 35 (a)-(c). The Young's modulus average, Standard Deviation (std), and the Coefficient of Variation (CV) for all PLA samples are shown in Table 12. The CV values were small for all samples, with the Primitive structures having the lowest CV, and Diamond structures the largest ones. These low CV values demonstrate good data consistency for all PLA samples. For the Primitive TPMS structures in 35 (a), the samples with the smallest porosity 0.3 gave the highest Young's modulus and yield stress, and these mechanical properties decreased with increasing the porosity of the samples, as expected. The Gyroid structures in 35 (b) and the Diamond structures in 35 (c) follow the same trend, which means that porosity dominates the Young's modulus and yield stress of the TPMS structures.

The two P_u6p03 samples showed a significant three-stage deformation [69,70]: an elastic stage, a plateau stage and a densification stage. At the elastic stage, the TPMS structure deforms elastically and can return to its original size while unloading, at the plateau stage, the material of the TPMS structure begins yielding, the strain increase continuously without increasing of stress with plastic deformation occurring at this stage, then the structure is gradually damaged and does not return to original size while unloading, at the final densification stage, the TPMS structures have been fully compressed, the inner wall of the structures are in contact with each other and they have been compacted, and therefore the stress increases with increasing strain. The other samples G_u10p03 and D_u8p03 in Fig. 35 (b) and 35 (c), respectively, followed the same trend. For samples P_u8p07, G_u6p07, and D_u10p07, with a porosity of 0.7, the experimental data only show the elastic stage and plateau stage, which means that for a maximum strain of 0.5, the structures with porosity 0.7 have not yet been fully compressed.

The simulation results, see the curves in Figs. 35 (a)-(c), match rather well the experimental data and, for samples with porosity of 0.7, it is also possible to simulate the three-stage compression. Concerning the Young's modulus, computed as the slope of the elastic phase of the stress-strain curve, the simulation can describe the change in Young's modulus well, providing values close to the experimental ones, as confirmed by the coefficient of variation results (see Table 13).

Table 12. Young's modulus average, Standard deviation (std), and the Coefficient of Variation (CV) for all PLA samples.

	Average (MPa)	Std (MPa)	CV
P_u8p07	84.59	0.4	0
P_u10p05	283.88	24.19	0.09
P_u6p03	489.74	47.46	0.1
G_u6p07	165.46	12.85	0.08
G_u8p05	288.82	39.75	0.14
G_u10p03	522.47	26.29	0.05
D_u10p07	199.43	33.26	0.17
D_u6p05	362.8	65.24	0.18
D_u8p03	602.07	105.35	0.17

Table 13. Young's modulus experimental and simulation data, with the Coefficient of Variation (CV).

	Experimental data (MPa)	Simulation results (MPa)	CV
P_u8p07	84.59	75.18	0.08
P_u10p05	283.88	233.83	0.14
P_u6p03	489.74	543.42	0.07
G_u6p07	165.46	127.09	0.19
G_u8p05	288.82	241.73	0.13
G_u10p03	522.47	483.98	0.05
D_u10p07	199.43	139.81	0.25
D_u6p05	362.8	288.01	0.16
D_u8p03	602.07	517.85	0.11

For TPMS structures, the porous structure can absorb energy while loading and, based on the force-displacement curves from compressive experiments, the energy absorption E is the area underneath the load deformation curve until reaching the specific maximum deformation, and can be calculated by:

$$E = \int_0^{u_1} F du \tag{19}$$

where the F is the loading force in force-displacement curves and in this study, for PLA samples u_1 =10 mm, and for zirconia samples, u_1 is the maximum deformation at which the sample fails.

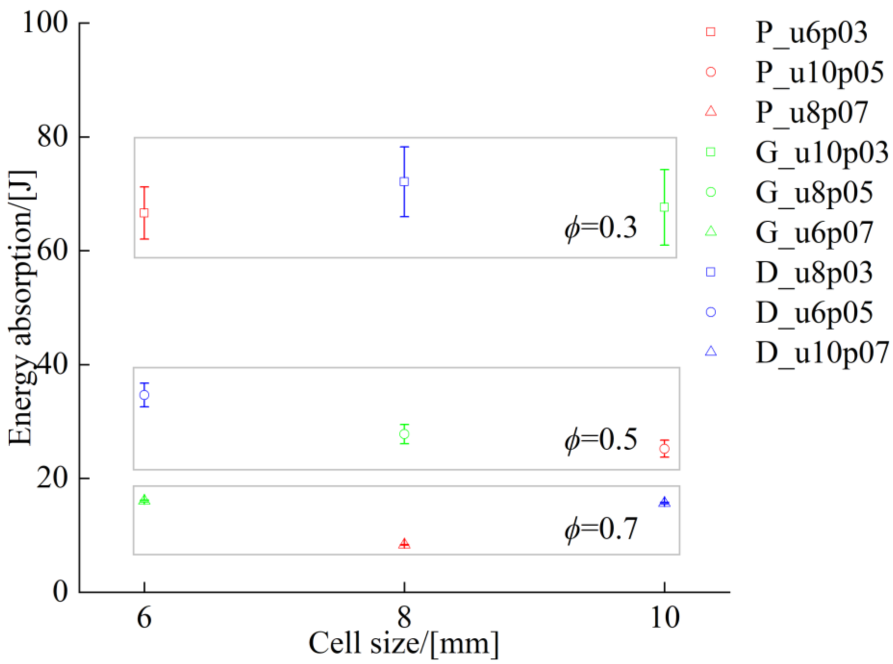

Figure 36. Energy absorption for PLA samples of different porosity.

The results for the energy absorption E with error bar for the PLA samples are plotted in Fig. 36 for all TPMS architectures. We can observe that their capability of absorbing energy varies, with the maximum energy absorption of the Primitive structure being that of sample P_u6p03 and equal to 71.22 J, while the minimum value of 8.39 J belongs to the P_u8p07 sample. For the Gyroid structures, the maximum energy absorption was

74.21 J (G_u8p03) while the minimum was 15.85 J (G_u6p07), for the Diamond structures, the maximum and minimum values were 78.22 J (D_u8p03) and 15.51 J (D_u10p07). As Fig. 36 shows, the energy absorption results can be grouped into three clusters, corresponding to porosity values of 0.3, 0.5, 0.7, this means that, for a maximum loading strain 0.5, the energy absorption of TPMS structures is mainly affected by the porosity, and increases with the decrease in porosity.

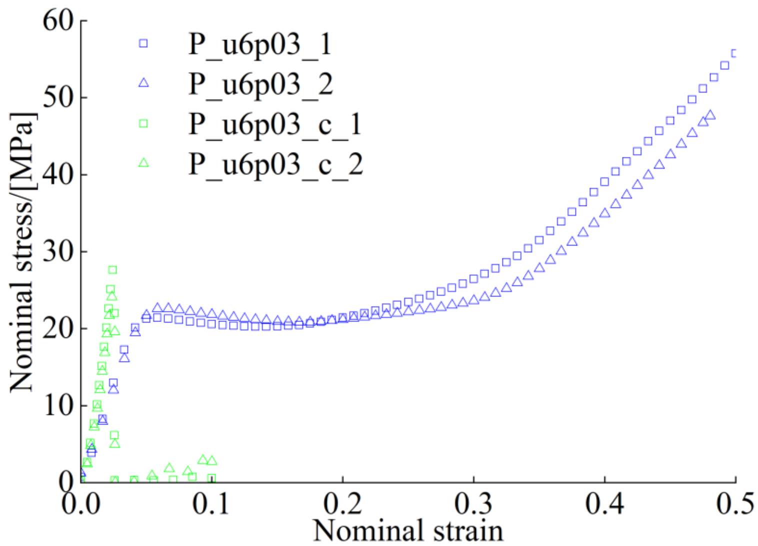

(a)

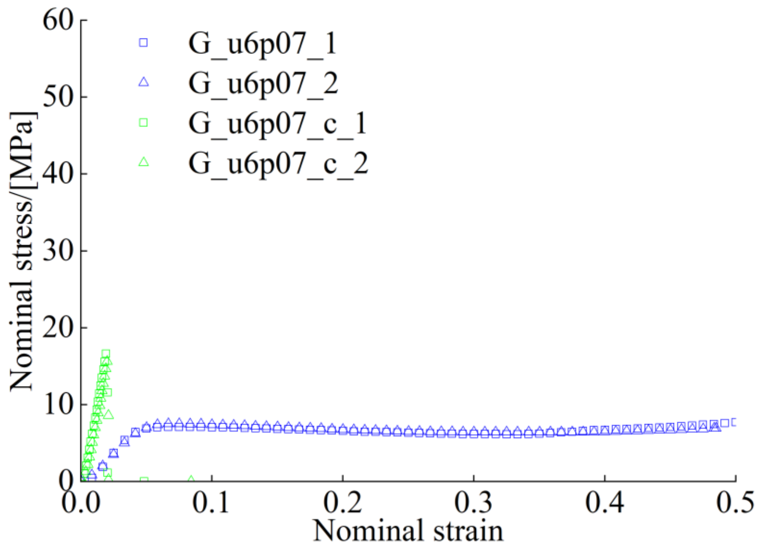

(b)

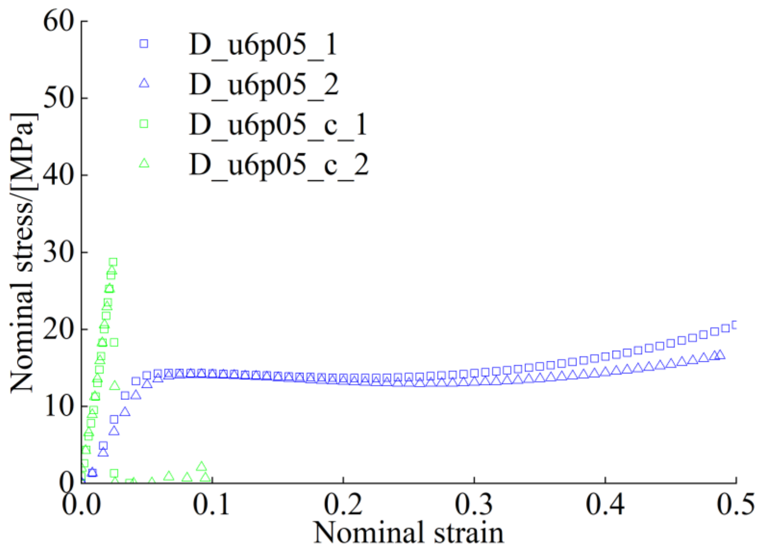

(b)

Figure 37. Zirconia samples data (green scatter), PLA samples data (clue scatter) comparison. (a) Primitive structure P_u6p03. (b) Gyroid structure G_u6p07. (c) Diamond structure D_u6p05.

Figs. 37 (a)-(c) report the zirconia stress-strain results and the corresponding PLA data, being zirconia a brittle material, the stress-strain curve exhibits a sharp drop after reaching the peak strength (catastrophic failure), which is completely different to the three-stage compressive behavior of the PLA samples. The strength of the zirconia specimens is of course higher than that of the PLA specimens, and for the Young's modulus values the situation is similar.

The energy absorption and maximum loading force of all zirconia TPMS structures are shown in Fig. 38. As Fig. 38 shows, the energy absorption and the maximum loading force are positively correlated, with the Diamond structures providing the maximum energy absorption and loading force, with the Primitive structures being the second, and Gyroid structures the last ones.

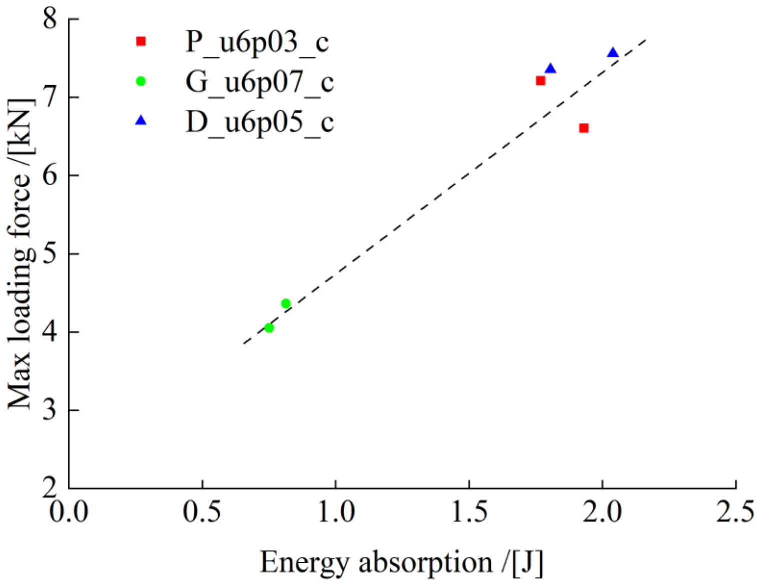

Figure 38. Maximum loading force as a function of the energy absorbed for zirconia samples.

4.3. Range analysis

In the experiments described in this Chapter, we considered three factors (see Table 2 and Table 3): TPMS structure, porosity and cell size. According to the orthogonal table $L_9(3^3)$, nine permeability and nine uniaxial compression experiments were conducted. Four datasets of experimental results were obtained: the Darcy permeability coefficient k_1 and the Forchheimer coefficient β came from the average of PLA and zirconia samples permeability results, while the Young's modulus, and the energy absorption came from the compressive experiments of PLA samples, which are all listed in Table 14.

This table shows that the four datasets vary in different ranges: the Darcy permeability coefficient k_1 from 6.98×10^{-10} to 2.87×10^{-8} m^2, the Forchheimer coefficient β from 578.55 to 18499.17 m^{-1}, the Young's modulus from 84.59 to 602.07 MPa, and the energy absorption from 8.32 to 72.11 J. To analyze the influence of three factors on these four datasets, range analysis is a useful statistic tool that can be used with orthogonal experiment design to find which is the primary factor affecting the results.

Table 14. Dataset results for the orthogonal table $L_9(3^3)$.

Label	Factors			Results			
	TPMS architecture	Porosity	Cell size (mm)	Darcy permeability coefficient k_1 (m^2)	Forchheimer coefficient β (m^{-1})	Young's modulus (MPa)	Energy absorption (J)
P_u8p07	Primitive	0.7	8	2.87×10^{-8}	578.55	84.59	8.32
P_u10p05	Primitive	0.5	10	3.56×10^{-9}	5135.61	283.88	25.22
P_u6p03	Primitive	0.3	6	6.98×10^{-10}	18499.17	489.74	66.61
G_u6p07	Gyroid	0.7	6	1.37×10^{-8}	991.07	165.46	16.04
G_u8p05	Gyroid	0.5	8	8.65×10^{-9}	1385.16	288.82	27.78
G_u10p03	Gyroid	0.3	10	2.72×10^{-9}	5975.09	522.47	67.59
D_u10p07	Diamond	0.7	10	1.90×10^{-8}	693.03	199.43	15.66
D_u6p05	Diamond	0.5	6	6.68×10^{-9}	1908.56	362.8	34.65
D_u8p03	Diamond	0.3	8	1.02×10^{-9}	8670.8	602.07	72.11

For a range analysis, the factor level mean value K_{ij} and the range value R_i should be calculated, where K_{ij} (where i is the factor number and j the corresponding level number) equals the average of all cases' results under one factor level. E.g., for the Darcy permeability coefficient k_1, the corresponding factor level mean K_{11} indicates the average of all k_1 results of cases for the TPMS architecture factor (factor number 1 in Table 2) and Primitive level (level number 1 for the TPMS architecture factor): P_u8p07, P_u10p05, P_u6p03. The range value R_i (i=the factor number) is defined as the difference between the maximum and minimum value in the factor level mean K_{ij} values with the same factor, meaning that, for the TPMS architecture factor, R_1=max(K_{11}, K_{12}, K_{13})-min(K_{11}, K_{12}, K_{13}).

Table 15. The factor level mean value K_{ij} and the range value R_i for the Darcy permeability coefficient k_1(m^2).

	Factors		
	TPMS architecture	Porosity	Cell size
K_{i1}	1.10×10^{-8}	2.05×10^{-8}	7.03×10^{-9}
K_{i2}	8.36×10^{-9}	6.30×10^{-9}	1.28×10^{-8}
K_{i3}	8.91×10^{-9}	1.48×10^{-9}	8.44×10^{-9}
R_i	2.62×10^{-9}	1.90×10^{-8}	5.75×10^{-9}

Table 16. The factor level mean value K_{ij} and the range value R_i for the Forchheimer coefficient β (m^{-1}).

	Factors		
	TPMS architecture	Porosity	Cell size
K_{i1}	8,071.11	754.22	7,132.94
K_{i2}	2,783.78	2,809.78	3,544.84
K_{i3}	3,757.46	11,048.36	3,934.58
R_i	5,287.33	10,294.14	3,588.10

Table 17. The factor level mean value K_{ij} and the range value R_i for the Young's modulus (MPa).

	Factors		
	TPMS architecture	Porosity	Cell size
K_{i1}	286.07	149.83	339.33
K_{i2}	325.58	311.83	325.16
K_{i3}	388.10	538.10	335.26
R_i	102.03	388.27	14.17

Table 18. The factor level mean value K_{ij} and the range value R_i for the energy absorption (J).

	Factors		
	TPMS architecture	Porosity	Cell size
K_{i1}	33.39	13.34	39.10
K_{i2}	37.13	29.22	36.07
K_{i3}	40.81	68.77	36.16
R_i	7.42	55.43	3.03

The factor level mean values and range values for the four results are shown in Tables 15-18. From the range analysis, we can ascertain the best combination of levels with different factors by choosing the levels which have the highest/lowest factor level mean value. Considering the factor level mean values of the Darcy permeability coefficient k_1 (see Table 15), for the highest k_1 value, the corresponding highest factor level mean values for each factor are: Primitive TPMS structure (1.10×10^{-8} m^2), porosity ϕ=0.7 (2.05×10^{-8} m^2), and cell size of 8 mm (1.28×10^{-8} m^2), therefore, the best combination is given by sample P_u8p07. Considering the factor level mean values of the Forchheimer coefficient β (see Table 16), the best combination for the highest β is the one obtained for sample P_u6p03, that is: Primitive TPMS structure (8,071.11 m^{-1}), porosity ϕ=0.3 (11,048.36 m^{-1}), and cell size of 6 mm (7,132.94 m^{-1}). Considering the factor level mean values of the Young's modulus results (see Table 17), the best combination giving the highest Young's modulus is the one given by sample D_u6p03, that is: Diamond TPMS structure (388.10 MPa), porosity ϕ=0.3 (538.10 MPa), and cell size of 6 mm (339.33 MPa). Considering the factor level mean values of the energy absorption results (see Table 18), the best combination providing the maximum energy absorption is the one for sample D_u6p03, that is: Diamond TPMS structure, porosity ϕ=0.3, and cell size of 6 mm, with sample D_u6p03 possessing the highest Young's modulus and the maximum energy absorption.

For different results, the corresponding factor level mean values for each factor are shown in Figs.39 (a)-(d). For the change of factor level mean values of the Darcy permeability coefficient k_1 (see Figs.39 (a)), the Primitive TPMS structure gives the highest k_1 value of 1.10×10^{-8} m^2, and the Gyroid structure gives the lowest k_1 value of 8.36×10^{-9} m^2, for the porosity, the k_1 values increase from 1.48×10^{-9} m^2 to 2.05×10^{-8} m^2 quickly with the increase of the porosity of the structure and, for the cell size, the k_1 values increase from 6 to 8 mm cell size, and decrease from 8 to 10 mm cell size, where the maximum k_1 value is 1.28×10^{-8} m^2 for a cell size of 8 mm and the minimum k_1 value is 7.03×10^{-9} m^2 for a cell size of 6 mm. For the change of factor level mean values of the Forchheimer coefficient β (see Figs.39 (b)), the Primitive structure gives the highest β value of 8,071.11 m^{-1}, and the Gyroid structure gives the lowest β value of 2,783.78 m^{-1}, for the porosity factor, the β value decrease from 11,048.36 m^{-1} to 754.22 m^{-1} with the increase in the structure's porosity and, for the cell size, the β value decreases from 6 to 8 mm cell size, and increases from 8 to 10 mm cell size, where the maximum β result is 7,132.94 m^{-1} for a cell size of 6 mm, and the minimum β value is 3,544.84 m^{-1} for a cell size of 8 mm.

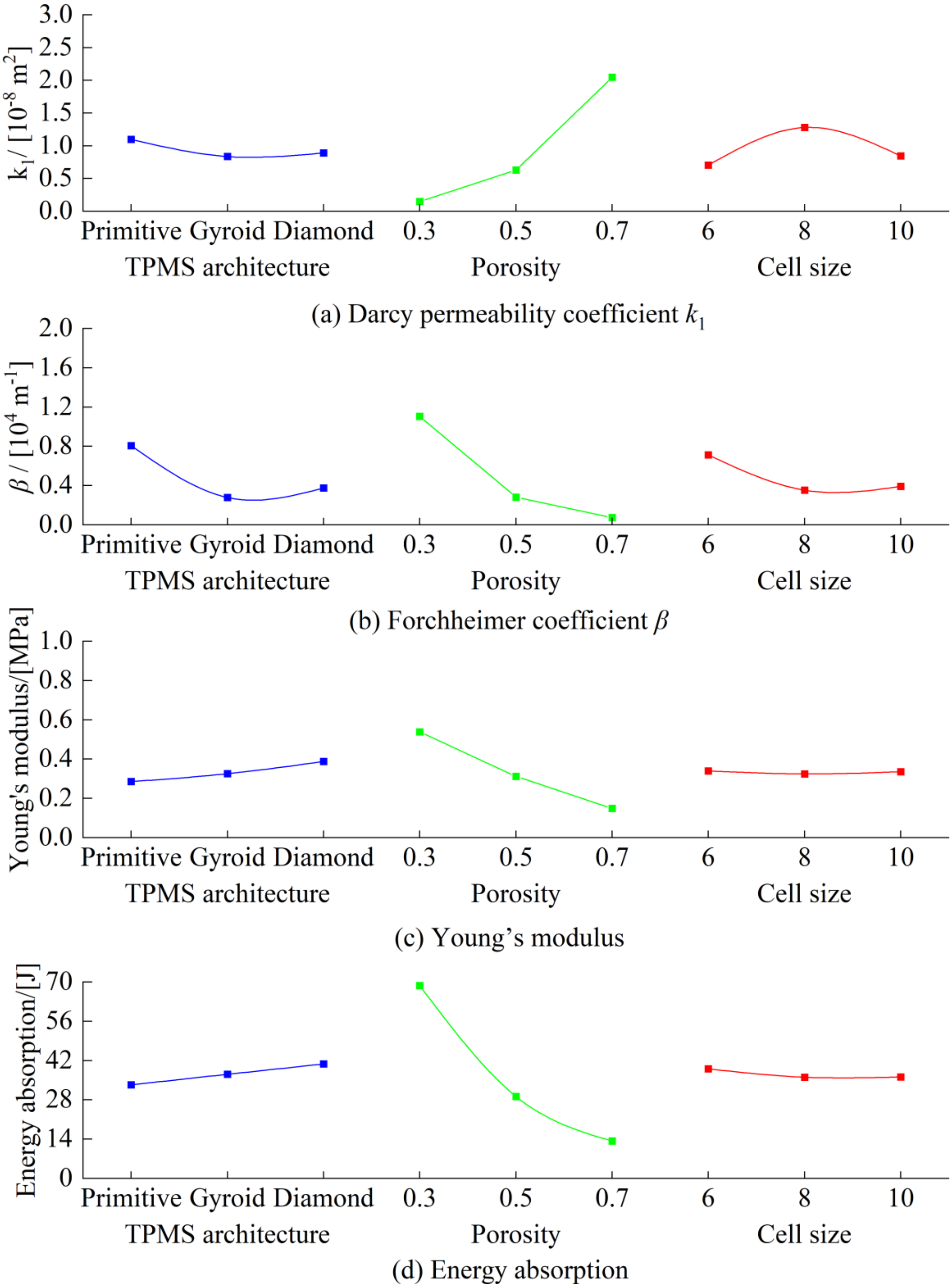

Figure 39. the factor level mean results for TPMS architectures, porosity, and cell size.(a) Darcy permeability coefficient k_1 (b) Forchheimer coefficient β. (c) Young’s modulus. (d) Energy absorption.

For the change of factor level mean values of the Young's modulus (see Figs.39 (c)), the Diamond TPMS structure gives the highest Young's modulus of 388.10 MPa, and the Primitive structure gives the lowest Young's modulus of 286.07 MPa, for the structure porosity, the Young's modulus and structure porosity are negatively correlated, the smallest porosity 0.3 gives the maximum Young's modulus 538.10 MPa, and the biggest porosity 0.7 gives the minimum Young's modulus 149.83 MPa and, for the cell size, the Young's modulus values vary little with the change in cell size, with a maximum Young's modulus of 339.33 MPa for a 6 mm cell size, and the minimum Young's modulus of 325.16 MPa for a 8 mm cell size. For the change of factor level mean values of the energy absorption (see Figs.39 (d)), similarly to the Young's modulus, the Diamond TPMS structure can absorb the maximum energy of 40.81 J, while the Primitive structure absorbs the minimum energy of 33.39 J, for the porosity factor, the energy absorption decreases quickly from 13.34 to 68.77 J with the porosity increasing from 0.3 to 0.7 and, for the cell size factor, the energy absorption decreases going from 6 to 8 mm cell size, and increases from 8 to 10 mm cell size, where the maximum energy absorption is 39.10 J for a cell size of 6 mm, and the minimum energy absorption is 36.07 J for a cell size of 8 mm.

To better understand the significance of each factor for those four datasets, the range value (R_i) for different results in Tables 15-18 are plotted in the Fig. 40. There are four Y-axis in the figure, which correspond to the four datasets (Darcy permeability coefficient k_1, Forchheimer coefficient β, Young's modulus, and energy absorption) and three factors (TPMS structure, porosity and cell size). The column height is related to the significance ranking of the factors with respect to the data, the columns for the same factor but belonging to different datasets are not comparable.

From the figure, the factor signification sequence for the Darcy permeability coefficient k_1 is: Porosity > Cell size > TPMS architecture, the range value R_i of the porosity to k_1 is the largest and this means that changing the porosity influences k_1 the most, that is, the porosity is the primary factor affecting the k_1 results. For the Forchheimer coefficient β, the factor significant sequence is: Porosity > TPMS architecture > Cell size, similarly to

k_1, the porosity is also the primary factor, which means that when trying to optimize permeability of TPMS architectures, the porosity is the primary factor to be considered, see also Fig. 33. Unlike k_1, the secondary factor for β is the TPMS architecture instead of the cell size, which means that for the flow conditions corresponding to a Darcy flow, the primary and secondary factors influencing the flow are the porosity and the cell size and, for the flow conditions corresponding to high speed and non-linear flow, the architecture of the TPMS structures affects permeability more than the cell size, because of the viscous resistance offered by the structures.

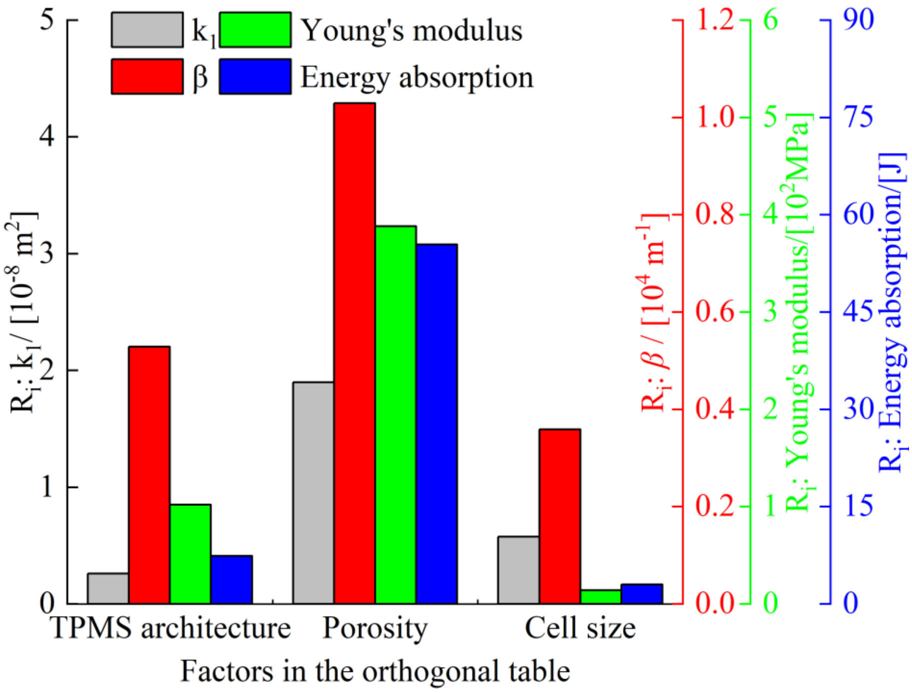

Figure 40. Range values for the Darcy permeability coefficient k_1, the Forchheimer coefficient β, the Young's modulus, and the energy absorption.

For the Young's modulus, the factor significant sequence is: Porosity > TPMS architecture > Cell size: the porosity is the primary factor and, for the energy absorption, the factor significant sequence is also: Porosity > TPMS architecture > Cell size. This means that the porosity is the primary factor for both Young's modulus and energy absorption (see also Fig. 36), and the effect of the three factors on the Young's modulus and energy absorption follows the same trend, that is, those two mechanical properties can be optimized by controlling the same factors. Finally, for all permeability and mechanical properties, the primary factor is always the porosity, which means that the designing of TPMS architectures should mainly focus on the designing an appropriate level of porosity in the structures.

The results can be applied in structural design, for instance when optimizing porous parts such as filters or scaffolds, or enhancing the heat exchanger efficiency through improved architectural topology, and offers valuable guidance for engineering solutions in load-bearing, fluid flow and thermal management contexts.

5. Mechanical properties of one cell hybrid TPMS structures with different hybrid weight functions

For design applications with specific mechanical performance demands, combining multiple TPMS units into a hybrid TPMS structure becomes a viable and effective approach. Current research on hybrid TPMS structures typically focuses on TPMS structures with a number of cells, and investigates the mechanical behavior of the whole hybrid TPMS structure.

This chapter presents an experimental investigation on the mechanical properties of one cell hybrid TPMS structures formed by combining basic TPMS structures, Gyroid and Diamond, within a single cell. Furthermore, to explore structures combined by the number of hybrid unit cells, the mechanical properties of structures with different TPMS cell configurations were also investigated. Additionally, two types of weight functions, linear and nonlinear, were applied to generate hybrid TPMS structures, and compression tests and three-point bending tests were conducted to measure and compare the mechanical properties of the two hybrid TPMS structures to the basic TPMS structures, Gyroid and Diamond.

5.1. Modeling and manufacturing of hybrid TPMS structures

5.1.1. One cell hybrid TPMS

The basic theory of generating hybrid TPMS structures was already presented by Equation 8 in Chapter 1.3. In this Chapter, as Fig. 41 shows, the hybrid process was only carried out by using two one cell TPMS structures, Gyroid and Diamond, to investigate the basic mechanical properties of one cell Gyroid and Diamond hybrid TPMS structures. Besides changing the basic TPMS architecture type, for generating a more complex hybrid, the weight function in Equation 8 gives more possibilities. In this research, as Equations 9 and 20 show, two kinds of weight functions were applied, namely a linear c function and a nonlinear s function:

$$\eta_s(x) = \begin{cases} 0, x < x_1 \\ 1, x > x_2 \\ \frac{1}{1+e^{S*(x-(x_2-x_1)/2)}}, x_1 < x < x_2 \end{cases} \tag{20}$$

where, $\eta_s(x)$ is the nonlinear s function which generates hybrid TPMS structures along the x direction, where x is the x axis coordinates, x_1 and x_2 are the beginning and end coordinates for the hybrid, S is the smoothing coefficient for the hybrid. Fig. 42 shows the curves for the linear c function and the nonlinear s function with different smoothing coefficients S. We can observe that the nonlinear s function gives a more smooth hybrid than the linear c function, and for the nonlinear s function, using a too small S coefficient (e.g., $S = 2$) will bring bigger error due to the discontinuity of $x_1<x<x_2$ interval to $x<x_1$ and $x>x_2$ intervals, while a too large S coefficient (e.g., $S = 10$) will make the area where the hybrid structure is located concentrated only in a narrow region. In this research, a program was written to calculate the error due to the discontinuity of interval $x_1<x<x_2$ to intervals $x<x_1$ and $x>x_2$, and the smoothing coefficient S was calculated as the value which can just meet the requirement of the given error value.

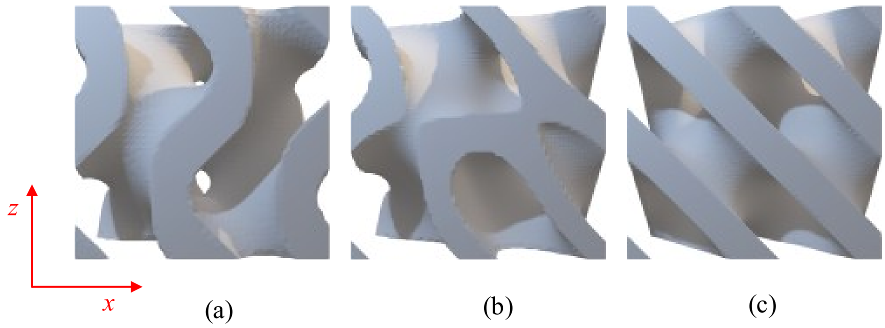

Figure 41. One cell linear hybrid TPMS structure combines the Gyroid and Diamond TPMS strucutres along x direction. (a) Gyroid cell. (b) one cell linear hybrid TPMS. (c) Diamond cell.

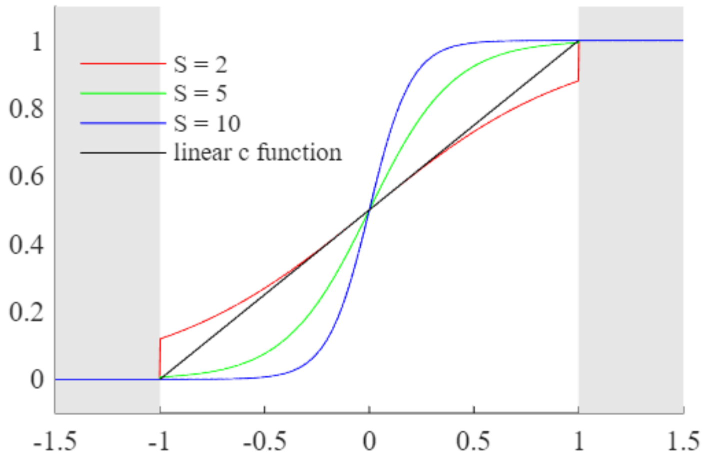

Figure 42. Curves of different weight functions.

Fig. 43 shows hybrid TPMS structures which combine the Gyroid and Diamond but were generated using different weight functions. It is evident that the geometry for these hybrid TPMS structures is different and therefore their mechanical properties will differ.

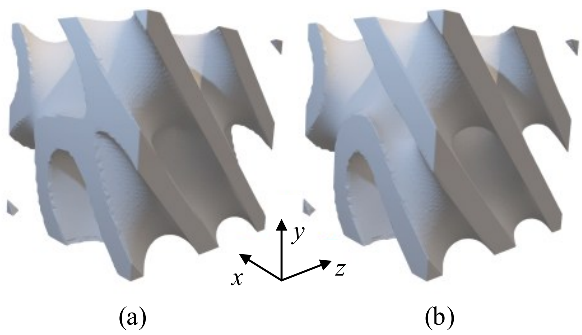

Figure 43. Hybrid TPMS structures for linear and nonlinear weight function. (a) Linear hybrid TPMS structure. (b) Nonlinear hybrid TPMS structure.

5.1.2. Experiments on structures with hybrid TPMS cells

Hybrid TPMS structures were manufactured by additive manufacturing, and their mechanical properties tested experimentally. In previous research [94,126], it has been observed that specimens containing only a single cell often fail to reflect the true mechanical properties of a structure comprised of the juxtaposition of that cell, due to the influence of manufacturing processes and experimental conditions. In this research, therefore, a number of cells were combined in the x, y, and z directions to minimize the impact of these external factors on the experimentally measured mechanical properties. In this research, Gyroid TPMS structures with different numbers of cells, 1*1*1, 2*2*2, 3*3*3, and 4*4*4, were designed, with a dimension of the basic cell of 4*4*4 mm. Testing Gyroid TPMS structures with different numbers of unit cells can give an insight on their mechanical behavior, useful for the subsequent design of hybrid TPMS structures.

Meanwhile, observing the hybrid TPMS structure shown in Fig. 44 (a), whose hybridization direction is the x-direction from a Gyroid TPMS structure to a Diamond TPMS structure generated with a linear weight function, we can note that this is not a periodic structure along the hybridization direction (x-axis). Therefore, it cannot be simply combined along the x-direction to form a periodic assembly.

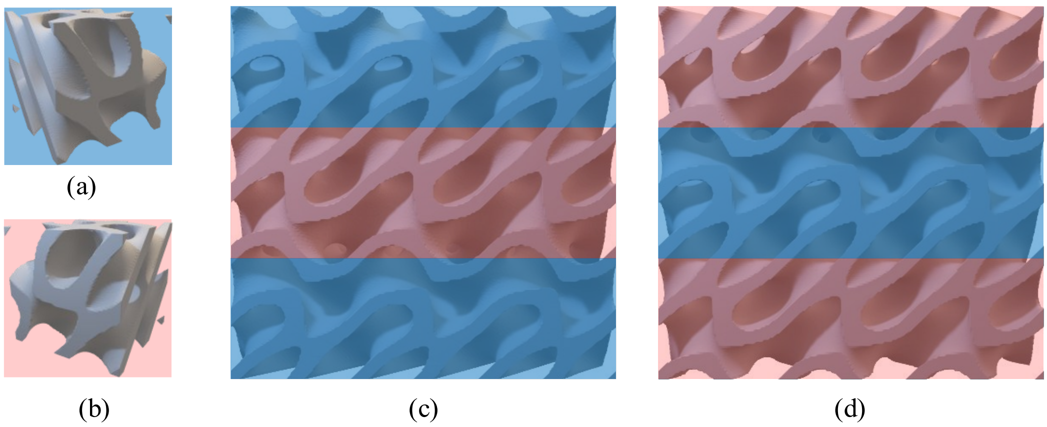

Figure 44. GD and DG hybrid TPMS unit cells, and different sequences to combine individual unit cells to create hybrid structures. (a) Diamond to Gyroid (DG) hybrid TPMS structure. (b) Gyroid to Diamond (GD) hybrid TPMS structure. (c) DGGDDG structure. (d) GDDGGD structure.

To enable the combination of the hybrid TPMS structures in the hybridization direction, a mirrored structure with respect to the *yoz* plane was generated, as shown in Fig. 44 (b). The hybridization sequence of the mirrored structure is from Diamond to Gyroid along the x-direction with the same weight function. In the following sections, the Gyroid to Diamond hybrid TPMS structure is referred to as the GD hybrid TPMS structure, while the mirrored Diamond to Gyroid one is denoted as the DG hybrid TPMS structure. Due to the mirror symmetry of the DG and GD hybrid TPMS structures with respect to the *yoz* plane, combining them along the x-direction becomes feasible. Moreover, to verify whether the newly generated DG hybrid TPMS structure has the same mechanical properties as the original GD hybrid TPMS structure, two different combined sequences of hybrid TPMS composite structures were designed, as shown in Fig. 44(c). The name of the structure DGGDDG means that the structure was assembled along the positive x-direction with a sequence of DG, GD, DG linear hybrid TPMS structures. By comparing the mechanical properties of these two hybrid TPMS cell configurations, the feasibility of using mirrored structures to achieve assembly of hybrid TPMS structures along the hybridization direction could be evaluated.

5.1.3. Additive manufacturing of alumina TPMS structure samples

With the development of techniques, the Additive Manufacturing technique has become more and more popular to fabricate structures which can't be fabricated by traditional techniques due to their complex structures. In this research, as Fig. 45(a) shows, all TPMS structure samples were fabricated by FDM technique with the 3D printer Raise PRO2. The alumina filament was purchased from Zetamix, France.

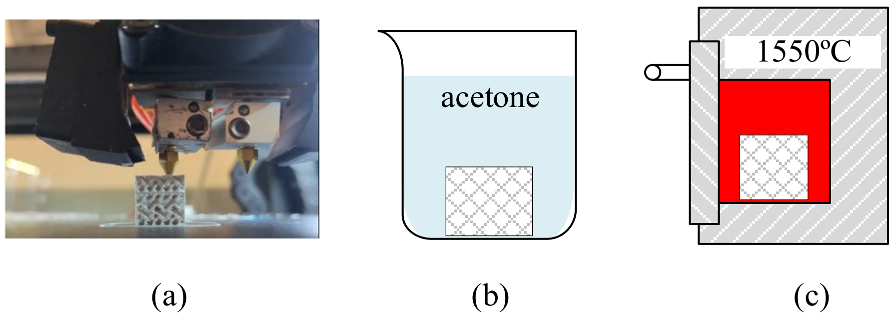

Figure 45. Alumina TPMS strcure sample fabrication. (a) 3D printed by FDM 3D printer (Raise PRO2). (b) Chemical debinding. (c) Thermal debinding and sintering.

Table 19 gives the printing parameters for the alumina samples, and the details about debinding and sintering. The samples were printed using a 0.4 mm nozzle with a printing temperature of 130°C, the build plate did not need to be heated to increase the adhesion of the green bodies while printing. The slice layer height was 0.2 mm, the wall line count was print wall line only to avoid the influence of infill pattern, the infill density was 100 %, no support structures were used, and the printing speed was selected as 15 mm/s, in order to print the overhang structures well.

Table 19. Parameters for alumina samples fabrication.

Material	Alumina (Al_2O_3)
3D Printing temperature	130°C
Build plate temperature	No heating
Filament diameter	1.75 mm
Nozzle size	0.4 mm
Layer height	0.2 mm
3D printing speed	15 mm/s
Wall line count	Print wall only
Infill density	100%
Supports structure	No
Chemical debinding temperature	40°C
Chemical debinding solver	Acetone
Chemical debinding duration	12 h
Chemical debinding weight loss	~5 wt%
Thermal debinding temperature	20 to 500°C, 8°C /h
Sintering temperature	20 to 1550°C, 50°C /h, holding 2h, 1550 to 20°C, 100°C /h
Linear Shrinkage after sintering	Horizontal: 20.8% ±1% Vertical: 23.2% ±1%

After the green bodies were printed, as Fig. 45(b) shows, the green bodies were placed in the acetone solvent for 12 hours at 40°C, losing ~5 wt% due to the chemical debinding.

After that, following the recommendation from the producer, they were inserted in a muffle furnace for thermal debinding in air (from 20 to 500°C with heating rate 8°C/h), and then sintered at 1550°C for 2 h, with a heating rate of 50°C/h. After sintering, the samples shrank 20.8% horizontally and 23.2% vertically, and this was taken into account by printing oversized samples in order to achieve the desired, final size previously specified.

The X-ray Diffraction (XRD) results for an alumina sample manufactured in this research is given in Fig. 46. The XRD pattern possesses a set of sharp, well-defined reflections at 2θ positions that agree with the corundum α-Al_2O_3 phase. Major reflections corresponding to (104), (113), (024), (116) and higher-angle planes are observed (typical 2θ: ≈35.1°, 43.4°, 52.6°, 57.6°, 66.7° and 77.5° for Cu Kα), indicating the sample is predominantly comprised of crystalline α-Al_2O_3.

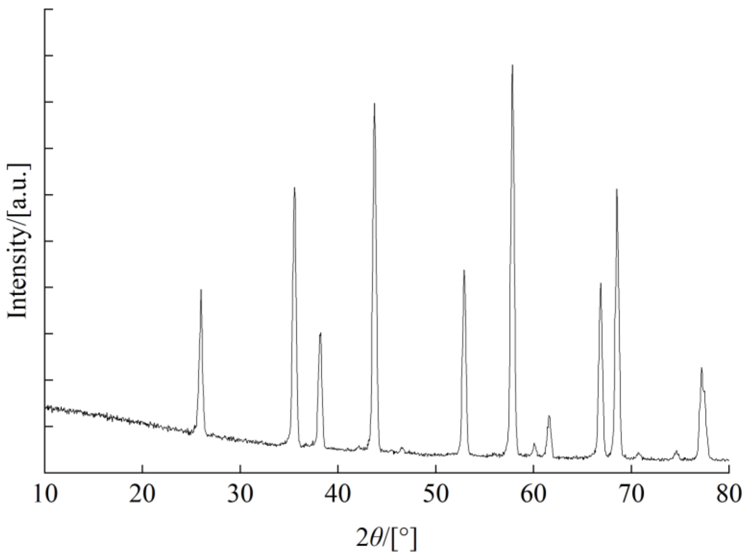

Figure 46. XRD pattern of a alumina sample.

5.2. Mechanical Property Results for different TPMS Cell Configurations

5.2.1. Cell numbers

We started our investigations by first analyzing the properties of TPMS structures built on the juxtaposition of a simple TPMS unit cell, i.e. without any hybridization. Figure 47 shows the Gyroid alumina samples with different cell number, 1*1*1, 2*2*2, 3*3*3, and 4*4*4, used for compression experiments to investigate the influence of cell number to the mechanical properties of TPMS structures. The compression experiments were conducted by a uniaxial testing machine with the Max 22kN sensor (Quasar 25, Galdabini, Cardano, Italy), applying Vaseline to the contact area between the sample and the plates to reduce friction. The loading speed was 2 mm/min, and the test was stopped when reaching a target displacement value of 2 mm, or the loading force dropped to 0 N. The data reported represents the average of three tests.

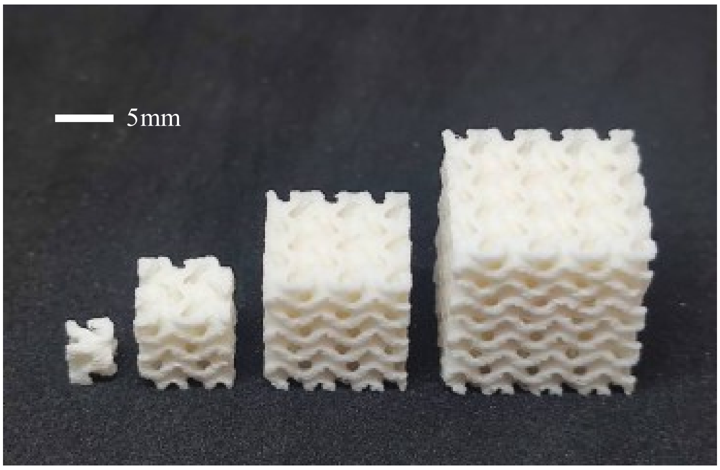

Figure 47. Gyroid alumina samples with different cell numbers for Young's modulus measurement.

The experiment results are plotted in Fig. 48. From the load-displacement curves, we can observe that all Gyroid alumina samples showed a brittle behavior when reaching the maximum strength value. With increasing number of cells in the samples, the more reliable the load-deformation curve became, for the sample with 1*1*1 Gyroid cell, the load-deformation curve shows obvious oscillations, with several load drops, which indicates that for the one cell TPMS structure, localized small failure can affect the macroscopic mechanical behavior. This behavior was also observed in samples containing 2*2*2 and 3*3*3 Gyroid cells, but the phenomenon gradually became less significant as the cell number increased. This means that although local failures still existed in the samples while loading, the influence on the overall macroscopic mechanical behavior decreased gradually, becoming negligible.

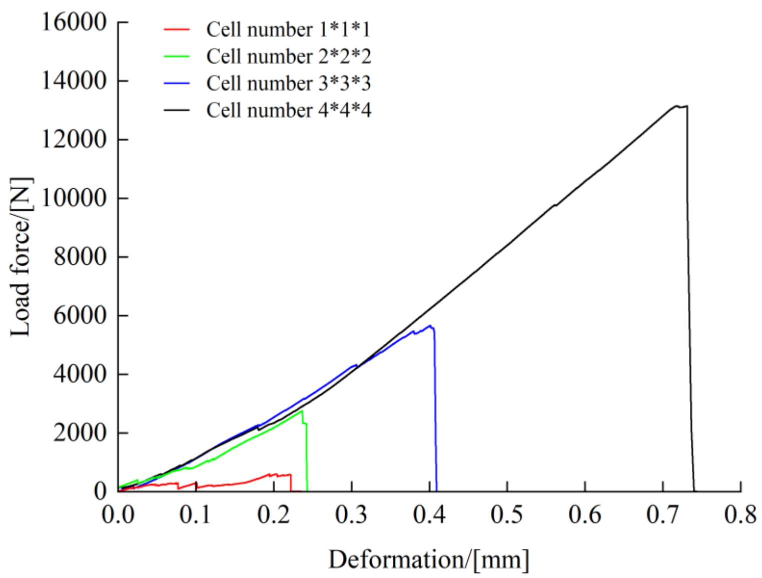

Figure 48. Load-deformation curves for alumina samples with different cell numbers.

To further investigate the effect of cell number on mechanical properties, Fig. 49 (a) and (b) give the Young's modulus results for Gyroid TPMS specimens of different volume fractions of porosity (0.7 and 0.5), and with various numbers of cells, where the Young's modulus in this research is the slope of the stress strain curves' linear stage nearby the peak of the load when samples fail and not considering the starting nonlinear stage caused by incomplete contact between the sample and the uniaxial loading machine. As shown in the figures, with increasing cell number, the Young's modulus of specimens at both porosity levels decreases and gradually stabilizes, and the variation (error) in Young's modulus significantly reduces. When the number of cells reaches or exceeds 3*3*3, the Young's modulus values become constant. This means that for cellular structures such as TPMS, only when the number of cells used to generate the structures becomes sufficiently large, the experimental results can reflect consistent and low-variance mechanical behavior of the structures. In this study, to balance manufacturing efficiency and material consumption, the 3*3*3 number of cells and 0.5 porosity is selected as the parameter for subsequent structural designs.

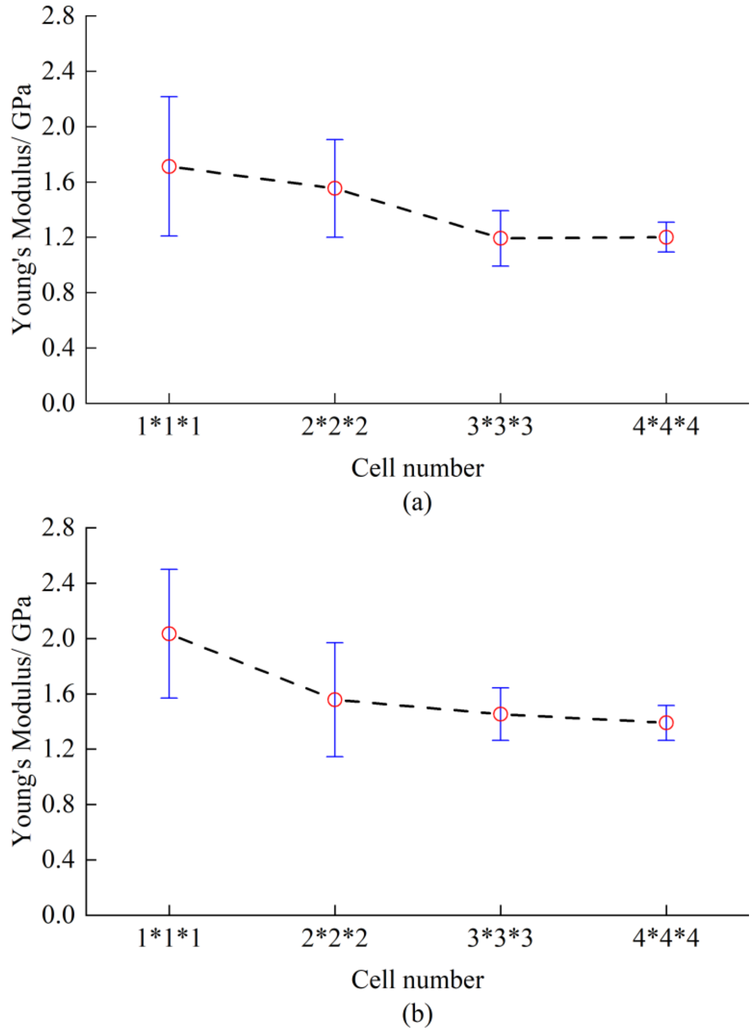

Figure 49. Young's modulus of TPMS structures with different cell numbers. (a) porosity = 0.7. (b) porosity = 0.5.

5.2.2. Mechanical properties of hybrid TPMS structures with different combined sequences

Following the description in Chapter 5.1.2, the hybrid TPMS structure models used to generate the samples with different combination sequences are shown in Fig. 44. DGGDDG and GDDGGD structures were printed, where the DGGDDG means that the combination sequence of the structures along the *x* direction is DG, GD, and DG hybrid structures, and along the *y* and *z* direction there is the same hybrid structure. Both models were printed using alumina and compressed under the same conditions as previously mentioned, in order to investigate their mechanical response. By comparing the mechanical properties of these two hybrid TPMS cell configurations, the feasibility of employing mirrored structures to enable the assembly of hybrid TPMS architectures along the hybridization direction could be evaluated.

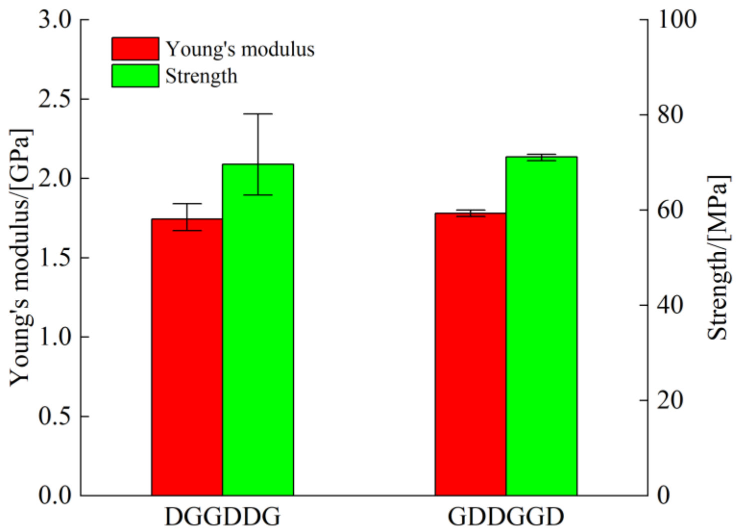

Figure 50. Young’s modulus and strength results for hybrid structures combined in different sequences.

The results of the mechanical properties of two hybrid structures are plotted in Fig. 50, for both Young’s modulus and compression strength. The values of Young’s modulus were 1.74 ± 0.09 GPa and 1.78 ± 0.02 GPa, and the strength was 69.64 ± 9.21 MPa and

71.20 ± 0.72 MPa, respectively. The results mean that for both Young's modulus and strength, the difference between the DGGDDG and GDDGGD structures is limited, which means the use of the mirror structure to combine hybrid TPMS structures is feasible.

5.3. Results for hybrid TPMS Structures generated using linear and nonlinear weight functions

After checking the influence of cell configuration on the mechanical properties, the samples for the investigation of the mechanical properties of hybrid TPMS structures with different weight functions are described below.

5.3.1. Mechanical properties of basic Gyroid, Diamond TPMS structures and linear, nonlinear hybrid TPMS structures

As Fig. 51 shows, the models used for the compressive experiments were the Gyroid, linear, nonlinear, and Diamond TPMS structures from left to right, and the length, width, and height for all models was 12 mm.

The experimental data for the Gyroid, Diamond, linear hybrid and nonlinear hybrid TPMS structure samples are plotted in Fig. 52, which reports the stress-strain values. Overall, none of the samples showed a linear mechanical behavior at the early stage of loading, which comes from the incomplete contact between the sample and the uniaxial loading machine at the beginning of compression because of non perfectly planar sample surfaces and, due to the limitation of the manufacturing technique, this phenomenon is more common for cellular structures. All samples showed the same brittle mechanical behavior typical of ceramic materials: once the peak of strength is reached, stress drops sharply, indicating catastrophic failure.

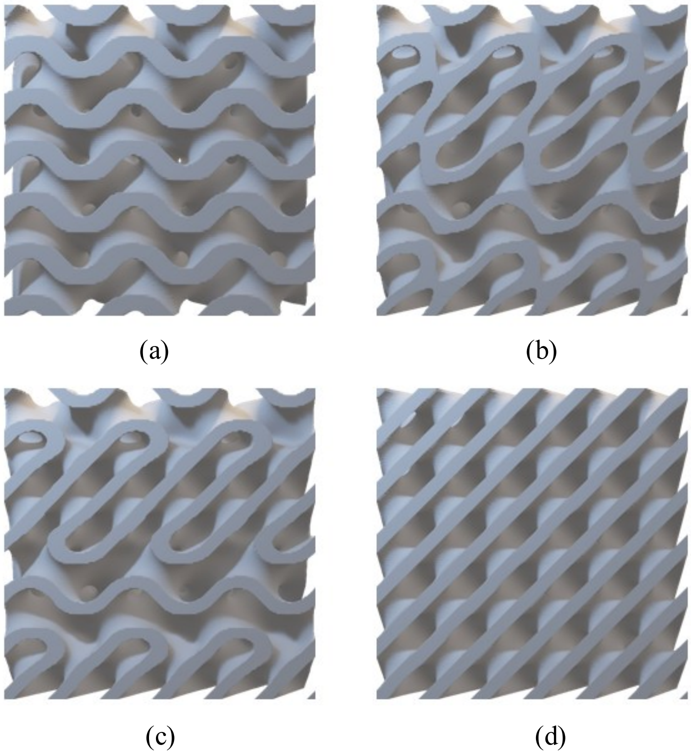

Figure 51. TPMS structures models for compressive experiment. (a) Gyroid. (b) linear hybrid. (c) nonlinear hybrid. (d) Diamond.

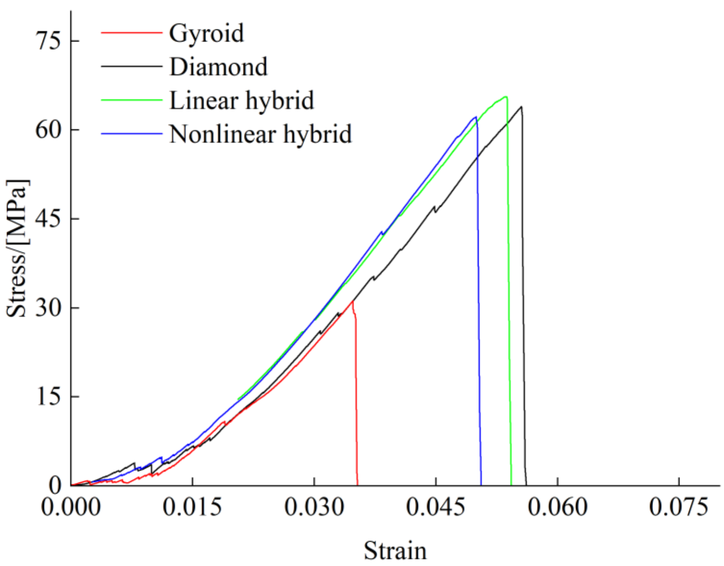

Figure 52. Stress-Strain curves of Gyroid, Diamond and linear, nonlinear hybrid TPMS structures.

The Gyroid structure possessed the lowest mechanical properties, and both its stiffness and strength were significantly lower than those of the other three structures, and brittle failure occurred at a strain value of approximately 0.035. The Diamond structure displayed higher mechanical properties compared to the Gyroid structure, and its stress strain curve closely overlaps with the curve of the Gyroid structure before the Gyroid structure failed, which means they have similar stiffness. However, the Diamond structure had a higher strength than both the Gyroid and the nonlinear hybrid TPMS structures. The diamond structure failed at a strain of around 0.056. Concerning the linear hybrid and nonlinear hybrid TPMS structures, they have very similar uniaxial compressive mechanical behavior, with nearly overlapping stress strain curves, and had higher stiffness than both the Gyroid and Diamond TPMS structures. Considering strength, the linear hybrid TPMS structure had the highest value, followed by the Diamond structure, with the nonlinear hybrid TPMS structure ranking third. Brittle failure occurred for the linear hybrid TPMS at a strain of approximately 0.053, and for the nonlinear hybrid TPMS at about 0.050.

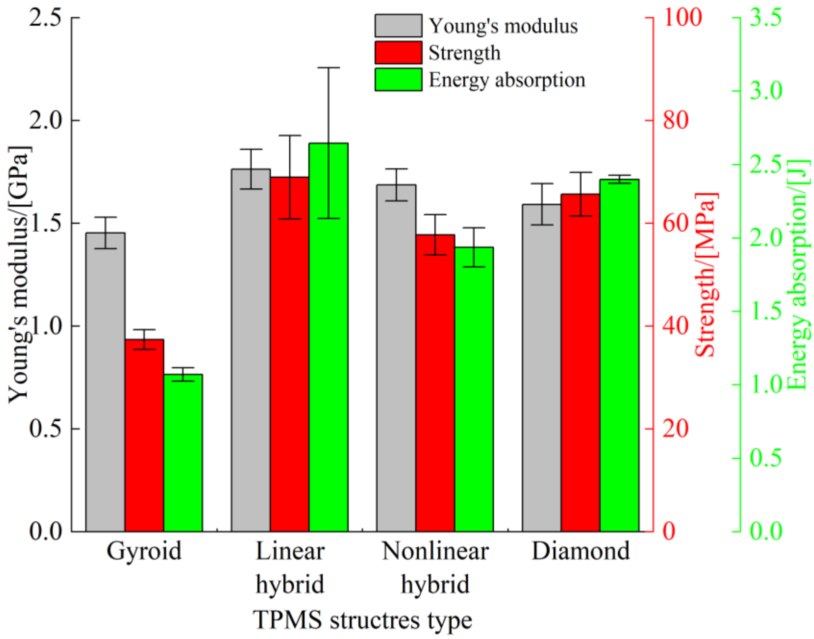

Figure 53. Young’s modulus, Strength, and Energy absorption results for the Gyroid, Diamond and linear, nonlinear hybrid TPMS structures.

Figure 53 shows the Young's modulus, strength, and energy absorption results for the Gyroid, Diamond, linear hybrid, and nonlinear hybrid TPMS structure samples. Where the energy absorption is calculated by Equation 19, and the deformation u_1 for the integral is the maximum deformation when the alumina samples fail. As the figure shows, for the uniaxial compression experiment the Gyroid structure had the lowest values for all mechanical properties: the Young's modulus was 1.45 ± 0.08 GPa, the compressive strength 37.38 ± 1.96 MPa, and the energy absorption 1.07 ± 0.05 J. In contrast, the linear hybrid TPMS structure had the highest values for all measured properties, with a Young's modulus of 1.76 ± 0.10 GPa, a strength of 68.99 ± 8.08 MPa, and an energy absorption of 2.65 ± 0.51 J. For the Diamond and nonlinear hybrid TPMS structures, their performance varied depending on the mechanical property considered. The Diamond structure had a Young's modulus of 1.59 ± 0.10 GPa, a strength of 65.57 ± 2.35 MPa, and an energy absorption of 2.40 ± 0.03 J, while the nonlinear hybrid TPMS possessed a higher Young's modulus of 1.69 ± 0.08 GPa, a slightly lower strength of 57.75 ± 3.92 MPa, and a lower energy absorption of 1.94 ± 0.13 J.

These results indicate that, compared to the simple Gyroid and Diamond TPMS structures, hybrid TPMS designs can significantly enhance mechanical performance. The linear hybrid TPMS structure provided improvements across all mechanical properties, and the nonlinear hybrid TPMS primarily improved stiffness, which means that the mechanical improvements provided by hybrid TPMS structures depend on the specific weight function used in their design.

5.3.2. Mechanical properties of hybrid TPMS structures along the primary axis

A hybrid TPMS structure is an anisotropic structure, and Fig. 54 shows the linear hybrid structure samples used for the investigation of the anisotropy of mechanical properties along the *x*, *y*, *z* directions. Considering that the 3D printing technology employed to manufacture the samples used in these experiments fabricates them layer by layer, for the same hybrid TPMS structure model but different load direction conditions the model was rotated accordingly to keep the loading direction perpendicular to the layer plane, in order to avoid the influence of the adhesion between adjacent layers on mechanical properties to of the samples, the model was rotated accordingly to keep the loading direction perpendicular to the layer plane. In figure, samples to be tested along the *x*, *y*, *z* directions are shown, the length, width, and height for all samples were 12 mm. In this research, both linear and nonlinear hybrid TPMS structure samples, Fig. 51 (b) and (c), with 0.5 porosity were fabricated to investigate the anisotropy of hybrid TPMS structures.

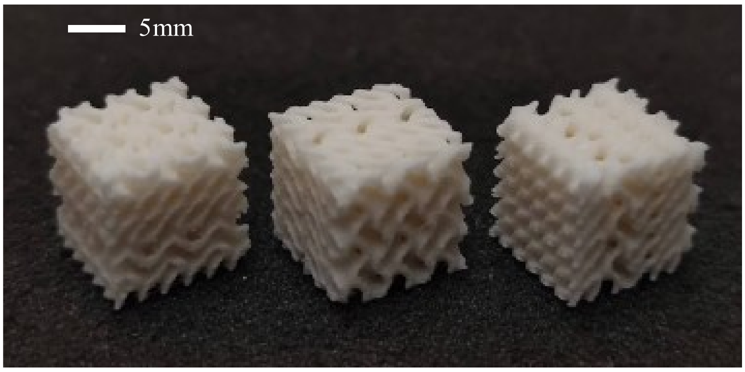

Figure 54. Cubic samples for compressive mechancal properties measurements of linear hybrid TPMS structures along different directions.

Figure 55 shows the stress-strain curves of the linear hybrid and nonlinear hybrid TPMS samples which were compressed along their *x*, *y*, and *z* direction. It should be mentioned that in this study, the *x* direction is defined as the hybridization direction. As Fig. 55 shows clearly, both the linear hybrid and nonlinear hybrid TPMS samples showed brittle fracture behavior under loading along all three directions, *x*, *y*, and *z*. The stiffness of both types of hybrid TPMS structure samples during the linear elastic stage was similar for all load directions. Moreover, the strength for the two kinds of hybrid TPMS structure samples follow the same order: $S_z > S_y > S_x$. That is, regardless of whether the design of the sample was generated using the linear or nonlinear hybrid weight function, the highest compressive strength occurs when the sample is loaded along the *z* direction, followed by the *y* direction, while the lowest strength observed was along the *x* direction. For the linear hybrid samples shown in Fig.55, failure occurred at a strain of 0.054 along the *x* direction, 0.064 along the *y* direction, and 0.081 along the *z* direction. For the nonlinear hybrid specimens, failure occurred at strains of 0.050 along the *x* direction, 0.073 along the *y* direction, and 0.081 along the *z* direction.

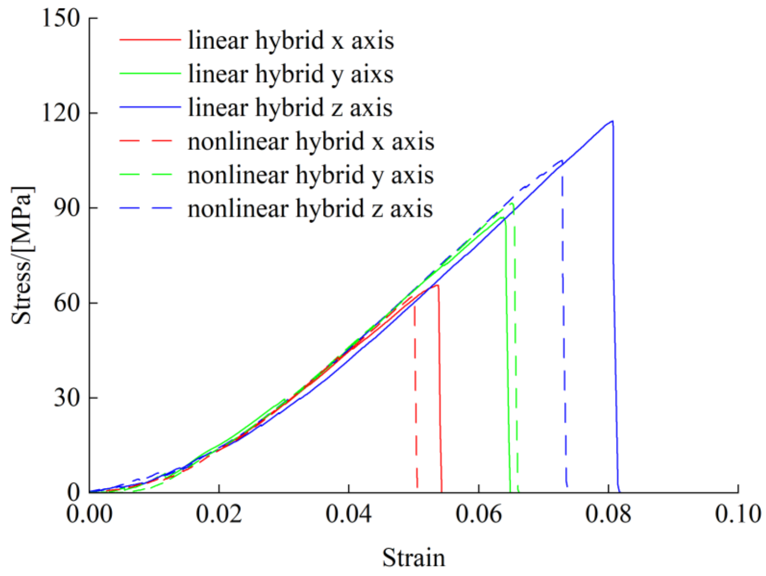

Figure 55. Strain-stress curves of linear hybrid TPMS structures compressed along different axis.

Specifically, the results for Young's modulus, strength, and energy absorption of all linear hybrid and nonlinear hybrid TPMS samples along their *x*, *y*, and *z* directions, and the average, standard deviations (std), and coefficients of variation (CV) of those results, are listed in Table 20 and Table 21, respectively. The coefficient of variation (CV) is a useful measure to assess the consistency of experimental data. Concerning the different hybrid TPMS structures, for the linear hybrid TPMS structure, the energy absorption measured along the *x* direction had the maximum CV (0.19), for the nonlinear hybrid TPMS structures, the energy absorption along *y* direction had the maximum CV (0.28). Concerning the different mechanical properties, for the Young's modulus the maximum CV was 0.06, for the linear hybrid TPMS structures along its *y* direction. For the compression strength, the maximum CV was 0.15, for the nonlinear hybrid TPMS structures along the *z* direction. For energy absorption, the maximum CV was 0.28, for the nonlinear hybrid TPMS structures tested along the *y* direction. These relatively low

CV values across different samples show good consistency in mechanical properties for all tested TPMS samples.

Table 20. Young's modulus, strength, and energy absorption results and Average, Standard Deviation (std), Coefficient of Variation (CV) of linear hybrid TPMS structures tested along the *x*, *y*, and *z* direction.

Sample	Young's modulus/[GPa]			Strength/[MPa]			Energy absorption/[J]		
	x	y	z	x	y	z	x	y	z
1	1.87	1.59	1.96	63.14	87.13	117.56	2.26	3.99	7.81
2	1.68	1.77	1.93	65.60	95.59	127.35	2.45	4.68	6.67
3	1.74	1.78	1.90	78.21	100.25	139.29	3.23	4.84	9.14
Average	1.76	1.71	1.93	68.99	94.33	128.07	2.65	4.50	7.87
Std	0.10	0.11	0.03	8.08	6.65	10.88	0.51	0.45	1.24
CV	0.06	0.06	0.02	0.12	0.07	0.08	0.19	0.10	0.16

Table 21. Young's modulus, strength, and energy absorption results and Average, Standard Deviation (std), Coefficient of Variation (CV) of nonlinear hybrid TPMS structures tested along the *x*, *y*, and *z* direction.

Sample	Young's modulus/[GPa]			Strength/[MPa]			Energy absorption/[J]		
	x	y	z	x	y	z	x	y	z
1	1.60	1.85	1.76	55.01	117.35	101.40	2.09	6.50	5.49
2	1.75	1.89	1.81	56.01	91.55	133.02	1.86	4.16	8.32
3	1.71	1.93	1.94	62.24	90.47	105.08	1.86	4.10	5.18
Average	1.69	1.89	1.84	57.75	99.79	113.17	1.94	4.92	6.33
Std	0.08	0.04	0.09	3.92	15.22	17.29	0.13	1.37	1.73
CV	0.05	0.02	0.05	0.07	0.15	0.15	0.07	0.28	0.27

For the linear hybrid TPMS structure samples, the highest Young's modulus was along the *z* direction (1.93 ± 0.03 GPa), and the lowest value was along the *y* direction (1.71 ± 0.11 GPa). The highest strength was also along the *z* direction (128.07 ± 10.88 MPa), and the lowest was along the *x* direction (68.99 ± 8.08 MPa). The highest energy absorption was along the *z* direction (7.87 ± 1.24 J), and the lowest was along the *x* direction (2.65 ± 0.51 J). These data show that the linear hybrid TPMS structure samples have significant anisotropic mechanical properties, with the highest mechanical properties generally observed when testing along the *z* direction rather than the *x* direction, which is the hybridization direction, and the lowest Young's modulus measured was along the *y* direction, while the lowest strength and energy absorption were along the *x* direction.

For the nonlinear hybrid specimens, the Young's modulus results along the *y* and *z* directions were similar, 1.89 ± 0.04 GPa and 1.84 ± 0.09 GPa, respectively, while testing along the *x* direction gave the lowest result (1.69 ± 0.08 GPa). The maximum strength value was 113.17 ± 17.29 MPa measured along the *z* direction, and the lowest value of 57.75 ± 3.92 MPa tested along the *x* direction. The energy absorption was the highest, 6.33 ± 1.73 J, when measured along the *z* direction and the lowest, 1.94 ± 0.13 J, when testing along the *x* direction. Similarly to the linear hybrid TPMS structure, the nonlinear hybrid structure samples also showed significant anisotropic mechanical properties, however, while the *z* direction had the highest strength and energy absorption results, the Young's modulus values were very similar, but slightly lower with respect to the value measured in the *y* direction. All the mechanical properties tested in the *x* direction were the lowest.

To better visualize the anisotropic behavior of the two hybrid TPMS structure samples with different weight functions, linear and nonlinear, and compare their mechanical property differences directly, Fig. 56 to Fig. 58 report the bar charts with error bars comparing the Young's modulus, strength, and energy absorption of the linear hybrid and nonlinear hybrid TPMS structure samples. All three figures clearly show the anisotropy of these two hybrid TPMS structures.

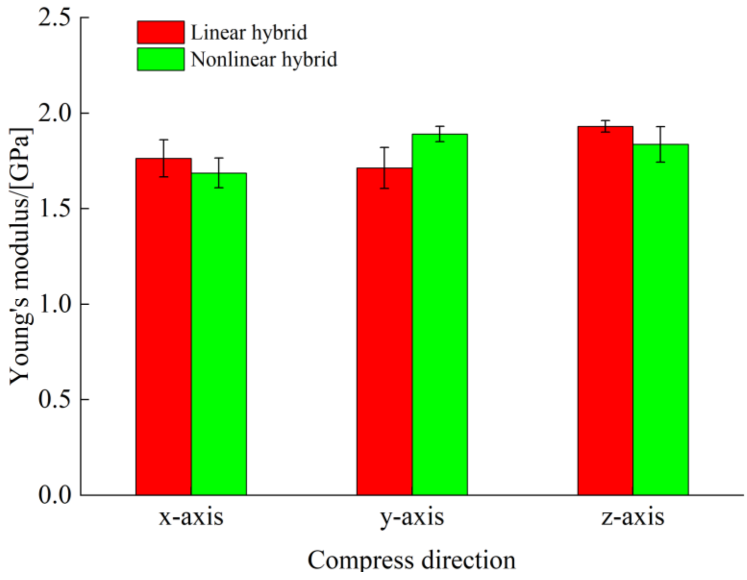

Figure 56. Young's modulus of samples tested along different axes for both linear and nonlinear hybrid TPMS structures.

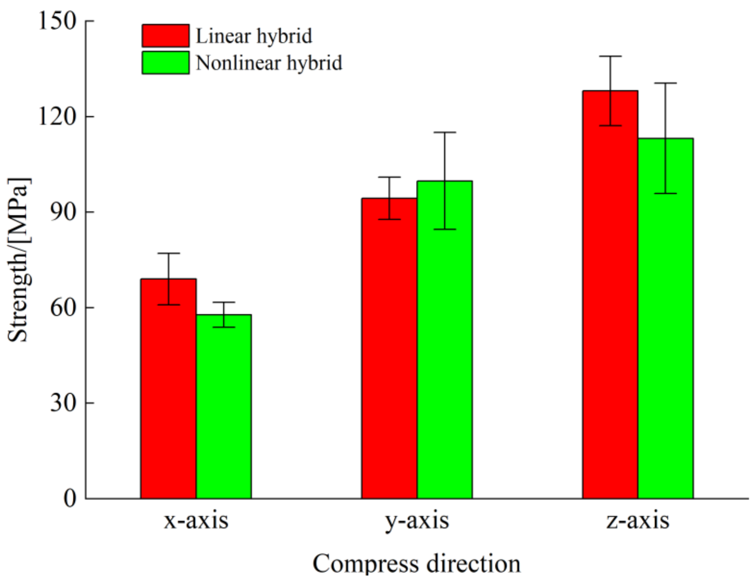

Figure 57. Compression strength of samples tested along different axes for both linear and nonlinear hybrid TPMS structures.

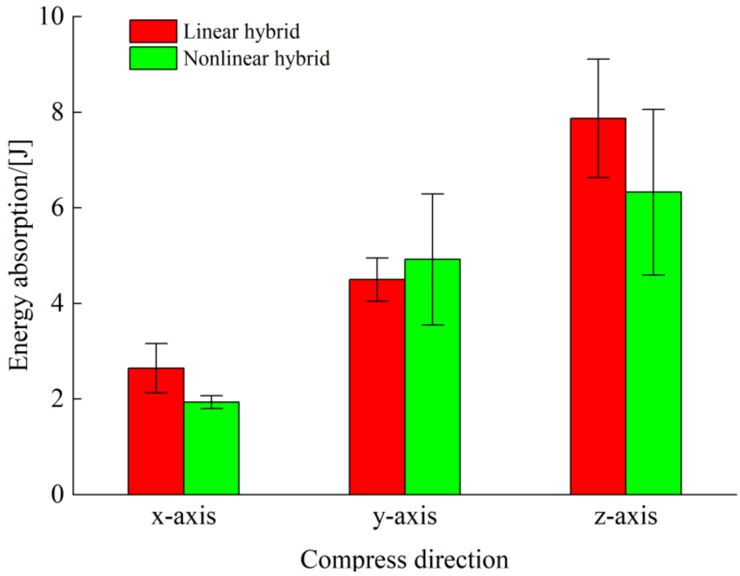

Figure 58. Energy absorption of samples tested along different axes for both linear and nonlinear hybrid TPMS structures.

As shown in Fig. 56 for the Young's modulus, the linear hybrid TPMS structure samples possessed a higher Young's modulus than the nonlinear hybrid TPMS structure when measured along the *x* and *z* directions, but a lower value when testing along the *y* direction. Concerning the anisotropy, the Young's modulus of the linear hybrid structure tested along the *x* and *y* directions were close, and significantly lower than the Young's modulus measured when loading along the *z* direction. In contrast, for the nonlinear hybrid structure, the Young's modulus measured when testing along the *y* and *z* directions were similar and higher than that obtained when testing along the *x* direction. Regarding strength and energy absorption (Fig. 57 and Fig. 58), both linear and nonlinear hybrid structure samples followed the same trend: results obtained when testing along the *z* direction were greater than those obtained when testing along the *y* direction, which in turn exceeded the results for the *x* direction. Furthermore, both the strength and energy absorption results along different directions showed the same behavior: the mechanical properties of linear hybrid TPMS structures were higher than those of nonlinear hybrid TPMS structures when testing along the *x* and *z* directions, but lower when testing along the *y* direction.

5.3.3. Three-point bending strength

Additionally, when using a mirror-symmetric hybrid TPMS structure, the hybrid TPMS structures can be combined together to generate beam samples, as reported in Fig. 59 (a), which shows the Gyroid, linear hybrid, and Diamond TPMS structures beam samples for the three-point bending test, from left to right. From the previous result concerning the cell number with respect to the mechanical properties, three layers of hybrid TPMS structures were placed along the height direction, meanwhile, to avoid lateral instability failure of the specimen during the three-point bending, two columns of three-layer high hybrid TPMS structures were set along the width direction, i.e. The length direction of the three-point bending beam sample corresponded to the *z* direction of the unit cell hybrid TPMS structure, and was 48 mm. The height direction aligned with the hybridization direction, *x* direction, with a height of 12 mm, and the width direction along the *y* was 8 mm. In this study, both linear hybrid and nonlinear hybrid TPMS structure samples were fabricated to investigate and compare the mechanical properties differences between them and basic Gyroid and Diamond TPMS structure beams.

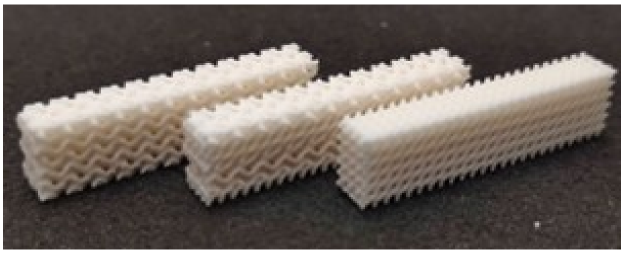

(a)

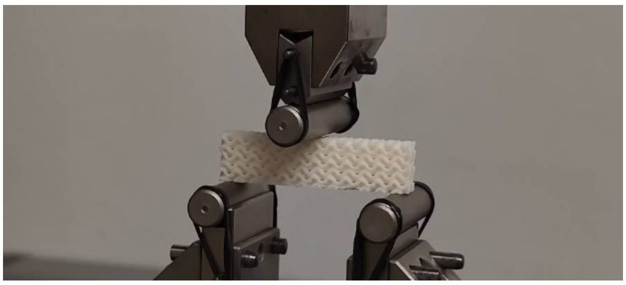

(b)

Figure 59. Beam sample and the three-point beding experiment. (a) Beam samples of Gyroid, linear hybrid, and Diamond TPMS strucutres. (b) Set up of three point bending.

As shown in Fig. 59(b), all samples were tested by the three-point bending. The span length for the three-point bending was 42 mm, with both the support and loading contact points utilizing rollers, the diameter of the rollers used was 9 mm to weaken the stress concentration caused by small roller diameters. The loading speed was set at 0.1 mm/min, and the test stopped when the displacement reached 2 mm or the load force dropped to zero. For the three-point bending test, the flexural modulus E_{flex} of the linear stage of the load deformation curves can be calculated by:

$$E_{\text{flex}} = \frac{L^3}{4wh^3} * \frac{dF}{du} \tag{21}$$

where, L is the span length, w and h are the width and height of the beam, respectively, dF/du represents the slope of the linear stage of the load force deformation curve in Fig. 60. Meanwhile, the flexural strength can be calculated by:

$$\sigma_{\text{flex}} = \frac{3FL}{2wh^2} \tag{22}$$

where, the F is the maximum load force of the beam.

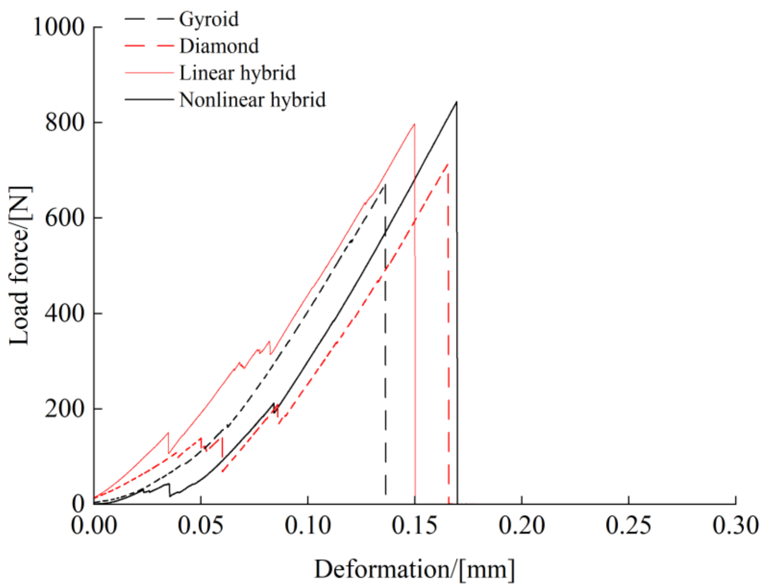

Figure 60. Load-deformation curves for three-point bending of Gyroid, Diamond and Linear, Nonlinear hybrid TPMS beams.

The load force deformation curves of the three-point bending experiments for Gyroid, Diamond, linear hybrid, and nonlinear hybrid TPMS beam samples are shown in Fig. 60. As shown in all curves, each load-displacement curve had a certain degree of load drop in the early stage of loading, which comes from the localized failure of the cellular structure of the TPMS beams, but for all sample, the location of the fracture was distant form the rollers. Then, in the later stage of loading, all beams demonstrated a stable linear elastic behavior before reaching brittle failure. The largest load for the Gyroid and Diamond TPMS beams was lower than that of the two kinds of hybrid TPMS beams. The Gyroid TPMS beam reached its maximum load of 670.48 N at a deformation of 0.14 mm before failure. The Diamond TPMS beam had a slightly higher maximum load of 710.49 N at a deformation of 0.17 mm. In comparison, the linear hybrid and nonlinear hybrid TPMS beams fracture at higher loads of 799.39 N and 844.37 N, respectively. The nonlinear hybrid TPMS beam can therefore carry a higher load force than the linear hybrid TPMS beam, which means better mechanical performance under three-point bending conditions.

The values for the flexural modulus, flexural strength, and energy absorption, together with their mean values, standard deviations (std), and coefficients of variation (CV) for the three-point bending testing of Gyroid, Diamond, linear hybrid, and nonlinear hybrid TPMS beam samples are listed in Table 22. The CV is a useful measure to assess the consistency of experimental data. For the Gyroid TPMS beam sample, the highest CV value was 0.04 for flexural strength, for the Diamond TPMS beam sample, the highest CV value was 0.09 for energy absorption, for the linear hybrid TPMS beam sample, the highest CV value was 0.12 for energy absorption, for the nonlinear hybrid TPMS beam sample, the highest CV value was 0.07 for energy absorption. These relatively low CV values across different samples show good consistency in mechanical properties for all tested TPMS beam samples. Specifically, concerning the flexural modulus of the beams in the three-point bending tests, the nonlinear hybrid TPMS structure beam possessed the highest flexural modulus (7.06 ± 0.04 GPa), while the Diamond TPMS structure beam had the lowest (5.97 ± 0.46 GPa). In terms of flexural strength, the nonlinear hybrid TPMS structure beam showed the highest value (29.91 ± 1.63 MPa), and the Gyroid

TPMS structure beam the lowest (23.77 ± 0.98 MPa). For energy absorption, the linear hybrid TPMS structure beam had the highest value (6.02 ± 0.12 J), and the Gyroid TPMS structure beam the lowest (0.37 ± 0.01). These differences in all mechanical properties between the two kinds of hybrid TPMS structure beams and the basic Gyroid and Diamond TPMS structure beams mean that using a hybrid TPMS structure beam design can provide significant improvements in mechanical performance with respect to non-hybrid structures.

Table 22. Flexural modulus (GPa), Flexural strength (MPa), and Energy absorption (J) average, standard deviation (std) and coefficient of variation (CV) of Gyroid, Diamond and linear, nonlinear hybrid TPMS beams.

Sample	Flexural modulus			Flexural strength			Energy absorption		
	Average	Std	CV	Average	Std	CV	Average	Std	CV
Gyroid	6.40	0.06	0.01	23.77	0.98	0.04	33.64	0.37	0.01
Diamond	5.97	0.46	0.08	26.32	0.33	0.01	45.51	4.25	0.09
Linear hybrid	6.32	0.13	0.02	27.90	1.04	0.04	49.19	6.02	0.12
Nonlinear hybrid	7.06	0.04	0.01	29.91	1.63	0.05	47.42	3.34	0.07

To better illustrate the differences in mechanical properties for different kinds of TPMS structure beams, Fig. 61 presents bar charts with error bars that contain the flexural modulus, flexural strength, and energy absorption of the Gyroid, Diamond, linear hybrid, and nonlinear hybrid TPMS beam samples. Generally, the two hybrid TPMS structure beams had better mechanical properties compared to the basic Gyroid and Diamond TPMS beams across nearly all mechanical properties. Specifically, in terms of flexural modulus, the order was: nonlinear hybrid > Gyroid > linear hybrid > Diamond TPMS. The flexural modulus values for the Gyroid and linear hybrid TPMS beams were very close, at 6.40 ± 0.06 GPa and 6.32 ± 0.13 GPa, respectively. For flexural strength, the order was: nonlinear hybrid > linear hybrid > Gyroid > Diamond TPMS, and the nonlinear hybrid TPMS beam had a higher flexural strength than the linear hybrid one.

Concerning energy absorption, the order was: linear hybrid > nonlinear hybrid > Gyroid > Diamond TPMS, and the linear hybrid TPMS beam had higher energy absorption than the nonlinear hybrid one. The mutual advantages of the two hybrid TPMS structural beams in flexural modulus, flexural strength and energy absorption reflect the differences in the generation of the two hybrid TPMS structural beams using different weight functions.

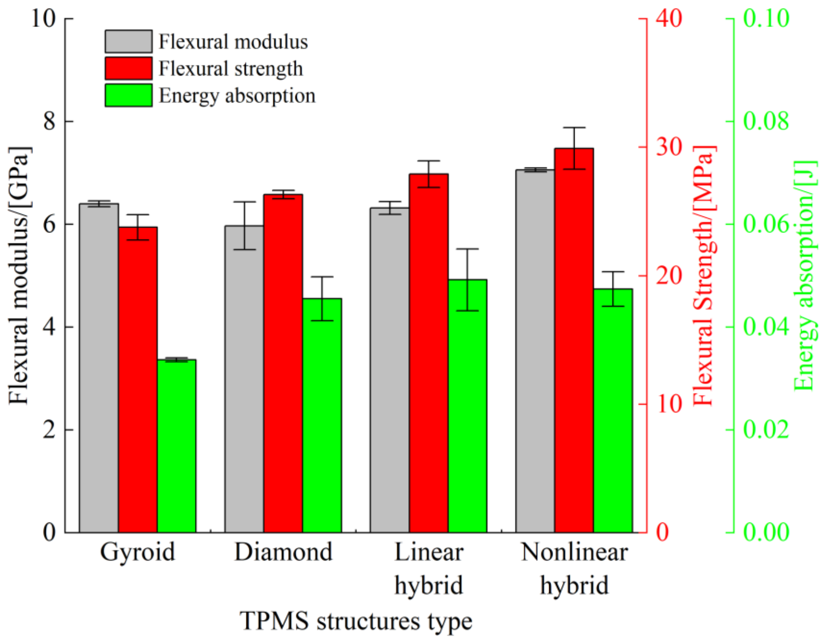

Figure 61. Flexural modulus, Flexural Strength, and Energy absorption values for Gyroid, Diamond and linear, nonlinear hybrid TPMS beams.

Conclusions

This research studied the permeability and mechanical properties of different kinds of TPMS structures. FDM additive manufacturing was used to produce samples of PLA, zirconia and alumina.

For basic TPMS structures, the permeability characteristics (Darcy permeability coefficient k_1 and Forchheimer coefficient β) and mechanical properties (Young's modulus and energy absorption) of three TPMS structures were investigated, as well as how those properties are influenced by the TPMS architecture, porosity and cell size. The relationship between the four properties and the three factors was studied by an orthogonal experimental design approach, and all experimental data were compared with Fluent and Abaqus simulations.

The results show that both Fluent and Abaqus simulations could match well the experimental data. The data for the four properties were analyzed by range analysis, to assess the factor level mean value. The Primitive TPMS architecture possessed the highest permeability characteristics but the lowest mechanical properties, the Darcy permeability coefficient k_1 increased significantly with the increase in porosity, and the Forchheimer coefficient β, Young's modulus and energy absorption increased significantly with the increase in porosity. No linear relationship of the cell size in relation to all properties was found. Moreover, the range value reflected the significance of the factors for each property, and porosity was ascertained to be the primary factor of influence for all properties. With respect to the sequence of the significance of the three factors, when considering the permeability properties, the TPMS architecture was the third for the Darcy permeability coefficient k_1 but second for the Forchheimer coefficient β. This means that, when comparing the effect of the cell size, the TPMS architecture is more significant in high-speed nonlinear flow conditions rather than in Darcy flow conditions. For the mechanical properties, the factor sequence and the response of factor level mean values for each factor were similar for both Young's modulus and energy absorption, which means that those factors may follow a common trend, and that those properties which can be simultaneously optimized by controlling the same factors.

For hybrid TPMS structures, this study experimentally tested how cell configuration, number of cells, and cell combination sequence can affect the mechanical properties. Uniaxial compression and three-point bending test were carried out for simple Gyroid, and Diamond TPMS structures, and for hybrid TPMS structures designed using different weight functions, to investigate the differences in mechanical properties of Young's modulus, strength, and energy absorption provided by the samples' architecture.

The results show that the Young's modulus can be affected by the cell number of a cellular structure. When a mirror symmetry hybrid structure is designed to let the assembling of one cell hybrid structure possible, the mechanical properties for samples assembled using a two-mirror symmetry hybrid structure sequence were similar, which means that using a mirror symmetry hybrid approach for combining hybrid structure together is feasible. Then, for hybrid structures generated using linear and nonlinear weight function, the mechanical properties along them x, y, and z direction were different, which means that the hybrid structures were anisotropic structures. Specifically, for the linear hybrid structure, all mechanical properties followed the order of loading directions: $z > y > x$, and the Young's modulus measured testing along the x and y directions was much lower than in the z direction for both hybrid structures. For the nonlinear hybrid structure, the Young's modulus of y and z directions were similar and both higher than for the x direction. Compression test results showed that, compared to the simple Gyroid and Diamond TPMS structures, the linear hybrid TPMS design provided improvements across all mechanical properties, and the nonlinear hybrid TPMS primarily improved stiffness. Three-point bending test results showed that two hybrid TPMS structure beams displayed better performance compared to the simple Gyroid and Diamond TPMS beams across nearly all mechanical properties. The two kinds of hybrid TPMS structure beams showed different advantages for different mechanical properties, with the linear hybrid TPMS structure beam providing higher energy absorption, and the nonlinear hybrid TPMS structure beam possessing higher flexural modulus. This means that the mechanical improvements provided by employing hybrid TPMS structures depend on the specific weight function used in their generation, leading to different and expanded range of values for all mechanical properties of interest.

Appendix A. The permeability experiment software

A software was developed for recording and processing data of permeability experiments. It contains two sections: the data record section and the data process section. Fig. 26 shows the set up of the permeability experiment, which contain the collection of mass flow data and pressure drop data. For the pressure drop data, which can be recorded by the software of Picolog, and for the mass flow data obtained from the digital mass flow meter, which is recorded by the data record section (see Fig. 62), the program can set the parameters. The computer is connected to the digital mass flow meter and, when clicking the start bottom, the on-time mass flow data will be plotted immediately and, after stopping the recording, the mass flow data can be exported as a .CSV format file.

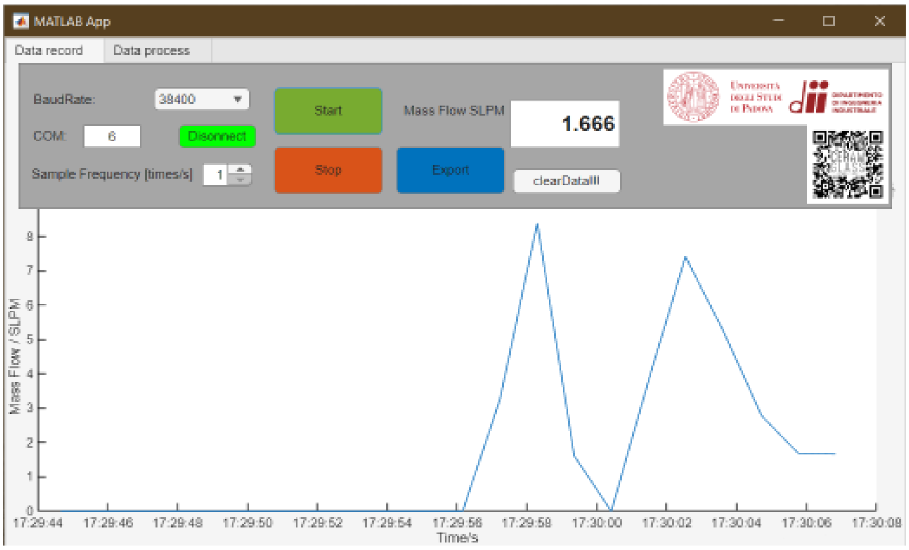

Figure 62. User graph interface of mass flow data recorder section of the permeability experiment software.

The digital mass flow meter used for the experiments in this research (MF6600, Siargo) is shown in Fig. 63, and the parameters are listed in Table 23. The meter can measure the flow of nitrogen in the range of 0-50 SLPM (Standard Liter Per Minute), with an accuracy of ±2.0% of the full scale, and a maximum working pressure of 1.0 MPa. This can meet the requirements of the permeability experiments carried out in this research.

Figure 63. The digital mass flow meter MF6600.

Table 23. Device parameters for the MF6600 flow meter.

Parameter	**MF6600**	**Unit**
Flow range (air/oxygen/nitrogen)	0-50	SLPM
Accuracy	±2.0	%FS
Repeatability	0.5	%FS
Output drift	±0.12	%/°C
Power supply	3.6-24 VDC or 3.6 V lithium battery (ER14250)	
Output interface	RS485 (Modbus)	
Display	LCD backlit display	
Max. working pressure	1.0	MPa
Operating temperature	-10 - +55	°C
Storage temperature	-20 - +65	°C
Operating humidity	<95% RH (non-condensing, no frost)	

The data process section, which is shown in Fig. 64, supports the importing of the pressure drop data recorded by the Picolog software, and the mass flow data recorded by the previous data record section. As Fig. 64 shows, this software supports batch import of pressure drop and mass flow data from multiple samples. Since the pressure drop and mass flow data are collected by two separate software systems, a time offset exists between them. Using the functional buttons in the Data Operation Panel within the current Section, users can do time alignment of pressure drop and mass flow data for each sample individually.

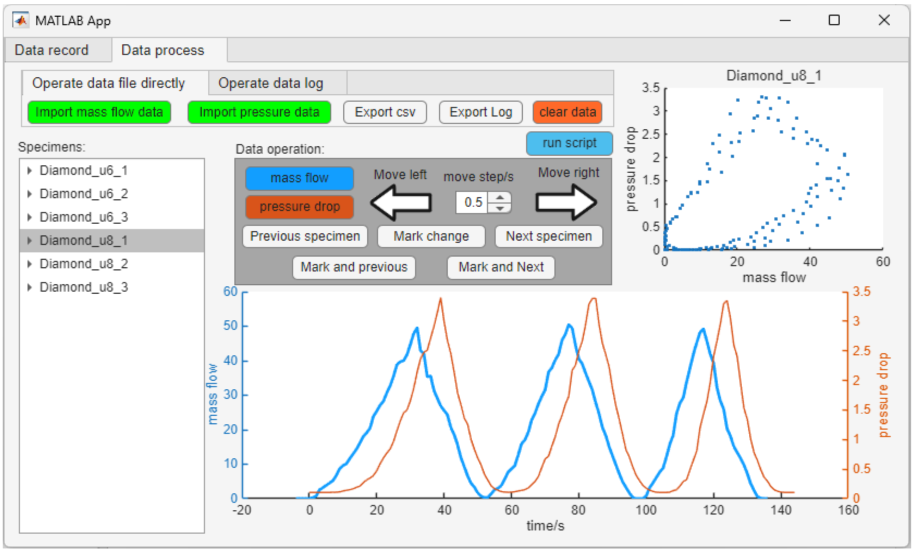

Figure 64. User graph interface of mass flow data and pressure drop data process section of the permeability experiment software.

The result of the data after alignment is shown in Fig. 65. After aligning the pressure drop and mass flow data by time, the scatter, the upper-right corner of the window, shows the permeability property of the sample clearly. Once the time alignment has been completed for all samples, clicking the Export .CSV button opens the interactive data export interface shown in Fig. 66, which allows users to select the data to be exported. Additionally, as shown in Fig. 65, the Export Log button enables the export of data operation as a .LOG file without modifying the original raw data, and this log file can also be imported later to restore or review the history of the data processing steps.

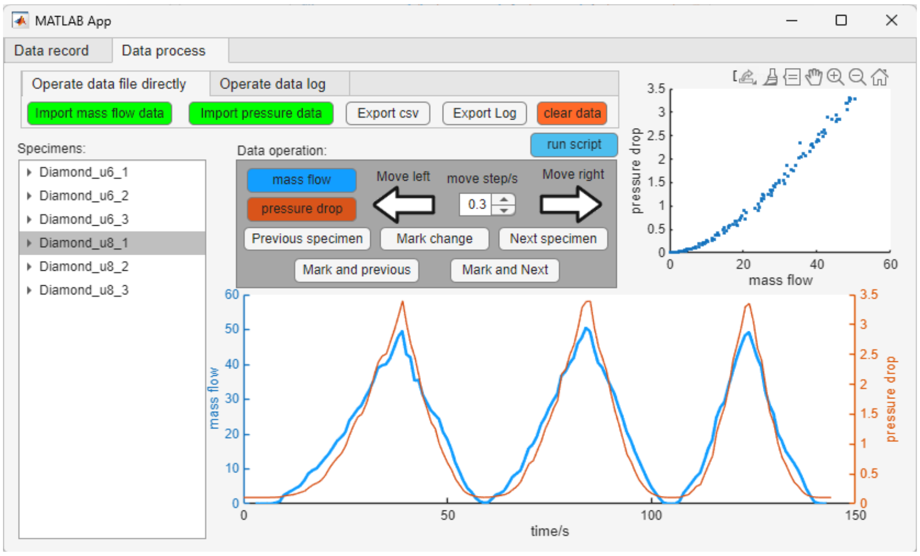

Figure 65. Mass flow and pressure drop data after alignment in the process section of the permeability experiment software.

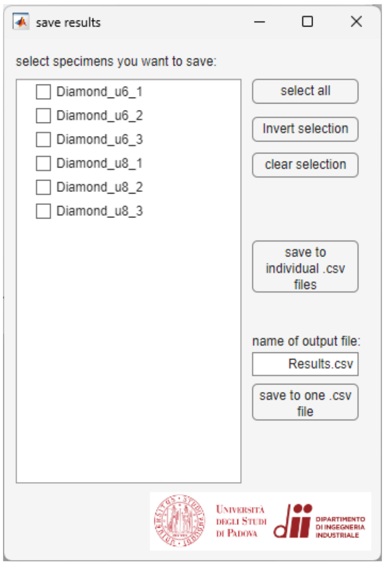

Figure 66. The results export graph user interface.

References

[1] DeBoer, B., Nguyen, N., Diba, F., & Hosseini, A. (2021). Additive, subtractive, and formative manufacturing of metal components: A life cycle assessment comparison. The International Journal of Advanced Manufacturing Technology, 115(1), 413–432. https://doi.org/10.1007/s00170-021-07173-5

[2] de Sousa Alves, B. A., Kontziampasis, D., & Soliman, A.-H. (2024). The Quest for the Holy Grail Of 3D Printing: A Critical Review of Recycling in Polymer Powder Bed Fusion Additive Manufacturing. Polymers, 16(16), 2306. https://doi.org/10.3390/polym16162306

[3] Patterson, A. E., Peddada, S. R. T., & Allison, J. T. (2019). Simple Basic and Convex Processing Time and Power Models for Common Subtractive Manufacturing Processes. https://hdl.handle.net/2142/106014

[4] Wong, K. V., & Hernandez, A. (2012). A Review of Additive Manufacturing. International Scholarly Research Notices, 2012(1), 208760. https://doi.org/10.5402/2012/208760

[5] Jung, S., Kara, L. B., Nie, Z., Simpson, T. W., & Whitefoot, K. S. (2023). Is Additive Manufacturing an Environmentally and Economically Preferred Alternative for Mass Production? Environmental Science & Technology, 57(16), 6373–6386. https://doi.org/10.1021/acs.est.2c04927

[6] Chen, H., Han, Q., Wang, C., Liu, Y., Chen, B., & Wang, J. (2020). Porous Scaffold Design for Additive Manufacturing in Orthopedics: A Review. Frontiers in Bioengineering and Biotechnology, 8. https://doi.org/10.3389/fbioe.2020.00609

[7] Lv, Y., Wang, B., Liu, G., Tang, Y., Lu, E., Xie, K., Lan, C., Liu, J., Qin, Z., & Wang, L. (2021). Metal Material, Properties and Design Methods of Porous Biomedical Scaffolds for Additive Manufacturing: A Review. Frontiers in Bioengineering and Biotechnology, 9. https://doi.org/10.3389/fbioe.2021.641130

[8] Tetik, H., Wang, Y., Sun, X., Cao, D., Shah, N., Zhu, H., Qian, F., & Lin, D. (2021). Additive Manufacturing of 3D Aerogels and Porous Scaffolds: A Review. Advanced Functional Materials, 31(45), 2103410. https://doi.org/10.1002/adfm.202103410

[9] Bandyopadhyay, A., & Heer, B. (2018). Additive manufacturing of multi-material structures. Materials Science and Engineering: R: Reports, 129, 1–16. https://doi.org/10.1016/j.mser.2018.04.001

[10] Hasanov, S., Alkunte, S., Rajeshirke, M., Gupta, A., Huseynov, O., Fidan, I., Alifui-Segbaya, F., & Rennie, A. (2022). Review on Additive Manufacturing of Multi-Material Parts: Progress and Challenges. Journal of Manufacturing and Materials Processing, 6(1), 4. https://doi.org/10.3390/jmmp6010004

[11] Han, D., & Lee, H. (2020). Recent advances in multi-material additive manufacturing: Methods and applications. Current Opinion in Chemical Engineering, 28, 158–166. https://doi.org/10.1016/j.coche.2020.03.004

[12] Moura, B., & Monteiro, H. (2025). Current development of the metal additive manufacturing sustainability—A systematic review. Environmental Impact Assessment Review, 112, 107778. https://doi.org/10.1016/j.eiar.2024.107778

[13] Pelin, G., Sonmez, M., & Pelin, C.-E. (2024). The Use of Additive Manufacturing Techniques in the Development of Polymeric Molds: A Review. Polymers, 16(8), 1055. https://doi.org/10.3390/polym16081055

[14] Ngo, T. D., Kashani, A., Imbalzano, G., Nguyen, K. T. Q., & Hui, D. (2018). Additive manufacturing (3D printing): A review of materials, methods, applications

and challenges. Composites Part B-Engineering, 143, 172–196. https://doi.org/10.1016/j.compositesb.2018.02.012

[15] Kodama, H. (1981). Automatic method for fabricating a three-dimensional plastic model with photo-hardening polymer. Review of Scientific Instruments, 52(11), 1770–1773. https://doi.org/10.1063/1.1136492

[16] Zhou, L., Miller, J., Vezza, J., Mayster, M., Raffay, M., Justice, Q., Al Tamimi, Z., Hansotte, G., Sunkara, L. D., & Bernat, J. (2024). Additive Manufacturing: A Comprehensive Review. Sensors, 24(9), 2668. https://doi.org/10.3390/s24092668

[17] Dubey, D., Singh, S. P., & Behera, B. K. (2024). A review on recent advancements in additive manufacturing techniques. Proceedings of the Institution of Mechanical Engineers, Part E: Journal of Process Mechanical Engineering, 09544089241275860. https://doi.org/10.1177/09544089241275860

[18] ASTM, I. (2022). Additive manufacturing-general principles-fundamental and vocabulary. Geneva, Switzerland: American Society of Testing Materials. https://doi.org/10.3403/30448424

[19] Winczewski, J. P., Zeiler, S., Gabel, S., Maestre, D., Merle, B., Gardeniers, J. G. E., & Arce, A. S. (2024). Additive manufacturing of 3D yttria-stabilized zirconia microarchitectures. Materials & Design, 238, 112701. https://doi.org/10.1016/j.matdes.2024.112701

[20] Li, H., Elsayed, H., & Colombo, P. (2024). Effect of particle size distribution and printing parameters on alumina ceramics prepared by Additive Manufacturing. Ceramics International, 50(4), 6340–6348. https://doi.org/10.1016/j.ceramint.2023.11.365

[21] Brafton. (Oct, 24, 2024,). 7 Families of Additive Manufacturing. Hybrid Manufacturing Technologies. https://hybrid-am.com/resource-centre/blogs/7-families-of-additive-manufacturing/

[22] Zocca, A., Colombo, P., Gomes, C. M., & Günster, J. (2015). Additive Manufacturing of Ceramics: Issues, Potentialities, and Opportunities. Journal of the American Ceramic Society, 98(7), 1983–2001. https://doi.org/10.1111/jace.13700

[23] Li, Q., An, X., Liang, J., Liu, Y., Hu, K., Lu, Z., Yue, X., Li, J., Zhou, Y., & Sun, X. (2022). Balancing flexural strength and porosity in DLP-3D printing Al2O3 cores for hollow turbine blades. Journal of Materials Science & Technology, 104, 19–32. https://doi.org/10.1016/j.jmst.2021.05.077

[24] Zhao, D., Bi, G., Chen, J., Quach, W., Feng, R., Salminen, A., & Niu, F. (2024). A critical review of direct laser additive manufacturing ceramics. International Journal of Minerals Metallurgy and Materials, 31(12), 2607–2626. https://doi.org/10.1007/s12613-024-2960-2

[25] Zhang, M., Fang, B., & Fan, L. (2025). Optimizing powder morphology and scanning strategies to enhance shape accuracy in L-PBF alumina ceramic formation. Ceramics International, 51(6), 8042–8053. https://doi.org/10.1016/j.ceramint.2024.12.240

[26] Ullah, A., Wu, H., Ur Rehman, A., Zhu, Y., Liu, T., & Zhang, K. (2020). Influence of laser parameters and Ti content on the surface morphology of L-PBF fabricated Titania. Rapid Prototyping Journal, 27(1), 71–80. https://doi.org/10.1108/RPJ-03-2020-0050

[27] Zhao, X., & Wang, T. (2023). Laser Powder Bed Fusion of Powder Material: A Review. 3D Printing and Additive Manufacturing, 10(6), 1439–1454. https://doi.org/10.1089/3dp.2021.0297

[28] Hu, Y., Wang, H., Cong, W., & Zhao, B. (2019). Directed Energy Deposition of Zirconia-Toughened Alumina Ceramic: Novel Microstructure Formation and Mechanical Performance. Journal of Manufacturing Science and Engineering, 142(021005). https://doi.org/10.1115/1.4045626

[29] Wu, D., Shi, J., Niu, F., Ma, G., Zhou, C., & Zhang, B. (2022). Direct additive manufacturing of melt growth Al2O3-ZrO2 functionally graded ceramics by laser directed energy deposition. Journal of the European Ceramic Society, 42(6), 2957–2973. https://doi.org/10.1016/j.jeurceramsoc.2022.01.034

[30] Huang, Y., Wu, D., Zhao, D., Niu, F., & Ma, G. (2021). Investigation of melt-growth alumina/aluminum titanate composite ceramics prepared by directed energy deposition. International Journal of Extreme Manufacturing, 3(3), 035101. https://doi.org/10.1088/2631-7990/abf71a

[31] Dadkhah, M., Tulliani, J.-M., Saboori, A., & Iuliano, L. (2023). Additive manufacturing of ceramics: Advances, challenges, and outlook. Journal of the European Ceramic Society, 43(15), 6635–6664. https://doi.org/10.1016/j.jeurceramsoc.2023.07.033

[32] Lv, X., Ye, F., Cheng, L., Fan, S., & Liu, Y. (2019). Binder jetting of ceramics: Powders, binders, printing parameters, equipment, and post-treatment. Ceramics International, 45(10), 12609–12624. https://doi.org/10.1016/j.ceramint.2019.04.012

[33] Du, W., Ren, X., Pei, Z., & Ma, C. (2020). Ceramic Binder Jetting Additive Manufacturing: A Literature Review on Density. Journal of Manufacturing Science and Engineering, 142(040801). https://doi.org/10.1115/1.4046248

[34] Gonzalez, J. A., Mireles, J., Lin, Y., & Wicker, R. B. (2016). Characterization of ceramic components fabricated using binder jetting additive manufacturing

technology. Ceramics International, 42(9), 10559–10564. https://doi.org/10.1016/j.ceramint.2016.03.079

[35] Gonzalez-Gutierrez, J., Cano, S., Schuschnigg, S., Kukla, C., Sapkota, J., & Holzer, C. (2018). Additive Manufacturing of Metallic and Ceramic Components by the Material Extrusion of Highly-Filled Polymers: A Review and Future Perspectives. Materials, 11(5), 840. https://doi.org/10.3390/ma11050840

[36] Li, W., & Leu, M. C. (2020). Material Extrusion Based Ceramic Additive Manufacturing. https://doi.org/10.31399/asm.hb.v24.a0006562

[37] Clemens, F., Sarraf, F., Borzì, A., Neels, A., & Hadian, A. (2023). Material extrusion additive manufacturing of advanced ceramics: Towards the production of large components. Journal of the European Ceramic Society, 43(7), 2752–2760. https://doi.org/10.1016/j.jeurceramsoc.2022.10.019

[38] Wu, X., Teng, J., Ji, X., Xu, C., Ma, D., Sui, S., & Zhang, Z. (2023). Research progress of the defects and innovations of ceramic vat photopolymerization. Additive Manufacturing, 65, 103441. https://doi.org/10.1016/j.addma.2023.103441

[39] Fiume, E., Coppola, B., Montanaro, L., & Palmero, P. (2023). Vat-photopolymerization of ceramic materials: Exploring current applications in advanced multidisciplinary fields. Frontiers in Materials, 10. https://doi.org/10.3389/fmats.2023.1242480

[40] Diptanshu, Miao, G., & Ma, C. (2019). Vat photopolymerization 3D printing of ceramics: Effects of fine powder. Manufacturing Letters, 21, 20–23. https://doi.org/10.1016/j.mfglet.2019.07.001

[41] Jang, S., Park, S., & Bae, C. (2020). Development of ceramic additive manufacturing: Process and materials technology. Biomedical Engineering Letters, 10(4), 493–503. https://doi.org/10.1007/s13534-020-00175-4

[42] Meeks, W. H. (1990). The Theory of Triply Periodic Minimal Surfaces. Indiana University Mathematics Journal, 39(3), 877–936. https://www.jstor.org/stable/24895601

[43] Foroughi, A. H., Liu, D., & Razavi, M. J. (2023). Simultaneous optimization of stiffness, permeability, and surface area in metallic bone scaffolds. International Journal of Engineering Science, 193, 103961. https://doi.org/10.1016/j.ijengsci.2023.103961

[44] Wang, H., Tan, D., Liu, Z., Yin, H., & Wen, G. (2022). On crashworthiness of novel porous structure based on composite TPMS structures. Engineering Structures, 252, 113640. https://doi.org/10.1016/j.engstruct.2021.113640

[45] Zhang, J., Chen, X., Sun, Y., Yang, J., Chen, R., Xiong, Y., Hou, W., & Bai, L. (2022). Design of a biomimetic graded TPMS scaffold with quantitatively adjustable pore size. Materials & Design, 218, 110665. https://doi.org/10.1016/j.matdes.2022.110665

[46] Zhang, X., Yan, S., Xie, X., Li, Y., Wang, C., & Wen, P. (2024). Multi-dimensional hybridized TPMS with high energy absorption capacity. International Journal of Mechanical Sciences, 273, 109244. https://doi.org/10.1016/j.ijmecsci.2024.109244

[47] Ding, J., Zou, Q., Qu, S., Bartolo, P., Song, X., & Wang, C. C. L. (2021). STL-free design and manufacturing paradigm for high-precision powder bed fusion. CIRP Annals, 70(1), 167–170. https://doi.org/10.1016/j.cirp.2021.03.012

[48] Feng, J., Fu, J., Yao, X., & He, Y. (2022). Triply periodic minimal surface (TPMS) porous structures: From multi-scale design, precise additive manufacturing to multidisciplinary applications. International Journal of Extreme Manufacturing, 4(2), 022001. https://doi.org/10.1088/2631-7990/ac5be6

[49] Thakur, R., Agarwal, P., Manoria, A., Singh, C. P., & Naresh. (2025). Customization of existing TPMS lattices to enhance biocompatibility and active cell proliferation area. Medical Engineering & Physics, 144, 104397. https://doi.org/10.1016/j.medengphy.2025.104397

[50] Nhaichaniya, G. K., Kumar, M., & Dayal, R. (2024). Improvement in Active Cell Proliferation Area at Higher Permeability With Novel TPMS Lattice Structure. Journal of Biomechanical Engineering, 146(111009). https://doi.org/10.1115/1.4066218

[51] Pires, T., Santos, J., Ruben, R. B., Gouveia, B. P., Castro, A. P. G., & Fernandes, P. R. (2021). Numerical-experimental analysis of the permeability-porosity relationship in triply periodic minimal surfaces scaffolds. Journal of Biomechanics, 117, 110263. https://doi.org/10.1016/j.jbiomech.2021.110263

[52] Santos, J., Pires, T., Gouveia, B. P., Castro, A. P. G., & Fernandes, P. R. (2020). On the permeability of TPMS scaffolds. Journal of the Mechanical Behavior of Biomedical Materials, 110, 103932. https://doi.org/10.1016/j.jmbbm.2020.103932

[53] Ali, D., Ozalp, M., Blanquer, S. B. G., & Onel, S. (2020). Permeability and fluid flow-induced wall shear stress in bone scaffolds with TPMS and lattice architectures: A CFD analysis. European Journal of Mechanics - B/Fluids, 79, 376–385. https://doi.org/10.1016/j.euromechflu.2019.09.015

[54] Rathore, S. S., Mehta, B., Kumar, P., & Asfer, M. (2023). Flow Characterization in Triply Periodic Minimal Surface (TPMS)-Based Porous Geometries: Part 1—Hydrodynamics. Transport in Porous Media, 146(3), 669–701. https://doi.org/10.1007/s11242-022-01880-7

[55] Gabrieli, R., Schiavi, A., Pennecchi, F. R., Alidoost, D., Schwentenwein, M., D’Andrea, L., Vena, P., Verné, E., & Baino, F. (2025). Permeability and microstructural parameters of 3D-printed triply periodic minimal surface (TPMS)

hydroxyapatite scaffolds. Journal of the American Ceramic Society, 108(11), e70104. https://doi.org/10.1111/jace.70104

[56] Castro, A. P. G., Pires, T., Santos, J. E., Gouveia, B. P., & Fernandes, P. R. (2019). Permeability versus Design in TPMS Scaffolds. Materials, 12(8), 1313. https://doi.org/10.3390/ma12081313

[57] Zeng, C., & Wang, W. (2022). Modeling method for variable and isotropic permeability design of porous material based on TPMS lattices. Tribology International, 176, 107913. https://doi.org/10.1016/j.triboint.2022.107913

[58] Montazerian, H., Zhianmanesh, M., Davoodi, E., Milani, A. S., & Hoorfar, M. (2017). Longitudinal and radial permeability analysis of additively manufactured porous scaffolds: Effect of pore shape and porosity. Materials & Design, 122, 146–156. https://doi.org/10.1016/j.matdes.2017.03.006

[59] Penubarthi, G. V., Suresh Babu, K. B., Sundararaj, S., & Kang, S. W. (2025). Investigating Experimental and Computational Fluid Dynamics of 3D-Printed TPMS and Lattice Porous Structures. Micromachines, 16(8), 883. https://doi.org/10.3390/mi16080883

[60] Zhou, J., Gui, Y., Xu, Q., He, L., & Long, Y. (2024). Investigation of permeability and biocompatibility of TPMS structures printed by laser powder bed fusion using Ti64-5Cu alloy for orthopedic implants. Materials Letters, 355, 135552. https://doi.org/10.1016/j.matlet.2023.135552

[61] Karaman, D., & Ghahramanzadeh Asl, H. (2023). The effects of sheet and network solid structures of similar TPMS scaffold architectures on permeability, wall shear stress, and velocity: A CFD analysis. Medical Engineering & Physics, 118, 104024. https://doi.org/10.1016/j.medengphy.2023.104024

[62] Sauermoser-Yri, M., Veldurthi, N., Wölfle, C. H., Svartvatn, P. J., Flo Hoem, S. O., Lid, M. J., Bock, R., Palko, J. W., & Torgersen, J. (2023). On the porosity-dependent permeability and conductivity of triply periodic minimal surface based porous media. Journal of Materials Research and Technology, 27, 585–599. https://doi.org/10.1016/j.jmrt.2023.09.242

[63] Li, Z., Chen, Z., Chen, X., & Zhao, R. (2024). Multi-objective optimization for designing porous scaffolds with controllable mechanics and permeability: A case study on triply periodic minimal surface scaffolds. Composite Structures, 333, 117923. https://doi.org/10.1016/j.compstruct.2024.117923

[64] Liu, Z., Gong, H., Gao, J., & Liu, L. (2022). Topological design, mechanical responses and mass transport characteristics of high strength-high permeability TPMS-based scaffolds. International Journal of Mechanical Sciences, 217, 107023. https://doi.org/10.1016/j.ijmecsci.2021.107023

[65] Tian, C., Wan, Y., Li, X., & Rong, Y. (2023). Permeability design and assessment of the additively manufactured metal-bonded diamond grinding wheel based on TPMS structures. International Journal of Refractory Metals and Hard Materials, 114, 106237. https://doi.org/10.1016/j.ijrmhm.2023.106237

[66] Hesselmann, F., Halwes, M., Bongartz, P., Wessling, M., Cornelissen, C., Schmitz-Rode, T., Steinseifer, U., Jansen, S. V., & Arens, J. (2022). TPMS-based membrane lung with locally-modified permeabilities for optimal flow distribution. Scientific Reports, 12(1), 7160. https://doi.org/10.1038/s41598-022-11175-y

[67] Li, X., Qu, P., Kong, H., Lei, Y., Guo, A., Wang, S., Wan, Y., & Takahashi, J. (2024). Enhanced mechanical properties of sandwich panels via integrated 3D printing of continuous fiber face sheet and TPMS core. Thin-Walled Structures, 204, 112312. https://doi.org/10.1016/j.tws.2024.112312

[68] Dong, D. T., Minh, T. Q., Tu, B. T., Tran, K. Q., & Nguyen-Xuan, H. (2024). Nonlinear thermo-mechanical static stability analysis of FG-TPMS shallow spherical shells. Thin-Walled Structures, 205, 112343. https://doi.org/10.1016/j.tws.2024.112343

[69] Qiu, N., Wan, Y., Shen, Y., & Fang, J. (2024). Experimental and numerical studies on mechanical properties of TPMS structures. International Journal of Mechanical Sciences, 261, 108657. https://doi.org/10.1016/j.ijmecsci.2023.108657

[70] Feng, G., Li, S., Xiao, L., & Song, W. (2023). Mechanical properties and deformation behavior of functionally graded TPMS structures under static and dynamic loading. International Journal of Impact Engineering, 176, 104554. https://doi.org/10.1016/j.ijimpeng.2023.104554

[71] Guan, Y., Zhang, X., Cao, X., Yang, H., Wang, S., Cao, W., & He, C. (2025). Dual-material TPMS metamaterial with high load-bearing capacity and performance stability. International Journal of Mechanical Sciences, 303, 110613. https://doi.org/10.1016/j.ijmecsci.2025.110613

[72] Ravichander, B. B., Jagdale, S. H., Jabed, A., & Kumar, G. (2023). Mechanical and corrosion behavior of sheet-based 316L TPMS structures. International Journal of Mechanical Sciences, 254, 108439. https://doi.org/10.1016/j.ijmecsci.2023.108439

[73] Al-Ketan, O., Lee, D.-W., Rowshan, R., & Abu Al-Rub, R. K. (2020). Functionally graded and multi-morphology sheet TPMS lattices: Design, manufacturing, and mechanical properties. Journal of the Mechanical Behavior of Biomedical Materials, 102, 103520. https://doi.org/10.1016/j.jmbbm.2019.103520

[74] Yang, L., Li, Y., Wu, S., Chen, P., Wu, H., Su, J., Wang, H., Liu, J., Yan, C., & Shi, Y. (2022). Tailorable and predictable mechanical responses of additive manufactured TPMS lattices with graded structures. Materials Science and Engineering: A, 843, 143109. https://doi.org/10.1016/j.msea.2022.143109

[75] Ma, X., Guo, C., Hu, C., Zhang, Z., & Shen, J. (2023). Study on the topological morphology and mechanical properties of variable-amplitude TPMS structures. Journal of Materials Research and Technology, 27, 3459–3472. https://doi.org/10.1016/j.jmrt.2023.10.164

[76] Chen, X., Hu, M., Sun, Y., Yang, J., Bai, L., & Xiong, Y. (2022). Wide-range tuning of the mechanical properties of TPMS lattice structures through frequency variation. Materials & Design, 224, 111370. https://doi.org/10.1016/j.matdes.2022.111370

[77] Luo, Z., Tang, Q., Song, J., Zhang, Y., Feng, Q., Ma, S., Setchi, R., & Zhao, M. (2024). TPMS-based strut-shell interpenetrating lattice metamaterial with wide-range customizable mechanical properties and superior energy absorption. Composite Structures, 349–350, 118555. https://doi.org/10.1016/j.compstruct.2024.118555

[78] Zhao, M., Li, X., Zhang, D. Z., & Zhai, W. (2023). TPMS-based interpenetrating lattice structures: Design, mechanical properties and multiscale optimization. International Journal of Mechanical Sciences, 244, 108092. https://doi.org/10.1016/j.ijmecsci.2022.108092

[79] Cao, Y., Lai, S., Wu, W., Sang, L., Lin, Y., Liu, T., Liang, C., Liu, W., & Zhao, Y. (2023). Design and mechanical evaluation of additively-manufactured graded TPMS lattices with biodegradable polymer composites. Journal of Materials Research and Technology, 23, 2868–2880. https://doi.org/10.1016/j.jmrt.2023.01.221

[80] Viet, N. V., Karathanasopoulos, N., & Zaki, W. (2022). Mechanical attributes and wave propagation characteristics of TPMS lattice structures. Mechanics of Materials, 172, 104363. https://doi.org/10.1016/j.mechmat.2022.104363

[81] Guo, X., Zheng, X., Yang, Y., Yang, X., & Yi, Y. (2019). Mechanical behavior of TPMS-based scaffolds: A comparison between minimal surfaces and their lattice

structures. SN Applied Sciences, 1(10), 1145. https://doi.org/10.1007/s42452-019-1167-z

[82] Sengsri, P., Fu, H., & Kaewunruen, S. (2022). Mechanical Properties and Energy-Absorption Capability of a 3D-Printed TPMS Sandwich Lattice Model for Meta-Functional Composite Bridge Bearing Applications. Journal of Composites Science, 6(3), 71. https://doi.org/10.3390/jcs6030071

[83] Xi, H., Zhou, Z., Zhang, H., Huang, S., & Xiao, H. (2023). Multi-morphology TPMS structures with multi-stage yield stress platform and multi-level energy absorption: Design, manufacturing, and mechanical properties. Engineering Structures, 294, 116733. https://doi.org/10.1016/j.engstruct.2023.116733

[84] Jian, L., He, J., Wen, G., Wang, Z.-P., Yang, J., Xie, Y. M., & Liu, J. (2025). Multifunctional TPMS-based metastructures. International Journal of Mechanical Sciences, 293, 110208. https://doi.org/10.1016/j.ijmecsci.2025.110208

[85] Chatzigeorgiou, C., Piotrowski, B., Chemisky, Y., Laheurte, P., & Meraghni, F. (2022). Numerical investigation of the effective mechanical properties and local stress distributions of TPMS-based and strut-based lattices for biomedical applications. Journal of the Mechanical Behavior of Biomedical Materials, 126, 105025. https://doi.org/10.1016/j.jmbbm.2021.105025

[86] Song, K., Wang, Z., Lan, J., & Ma, S. (2021). Porous structure design and mechanical behavior analysis based on TPMS for customized root analogue implant. Journal of the Mechanical Behavior of Biomedical Materials, 115, 104222. https://doi.org/10.1016/j.jmbbm.2020.104222

[87] Bobbert, F. S. L., Lietaert, K., Eftekhari, A. A., Pouran, B., Ahmadi, S. M., Weinans, H., & Zadpoor, A. A. (2017). Additively manufactured metallic porous biomaterials based on minimal surfaces: A unique combination of topological, mechanical, and

mass transport properties. Acta Biomaterialia, 53, 572–584. https://doi.org/10.1016/j.actbio.2017.02.024

[88] Xu, Y., Zhang, S., Ding, W., Du, H., Li, M., Li, Z., & Chen, M. (2024). Additively-manufactured gradient porous bio-scaffolds: Permeability, cytocompatibility and mechanical properties. Composite Structures, 336, 118021. https://doi.org/10.1016/j.compstruct.2024.118021

[89] Montazerian, H., Mohamed, M. G. A., Montazeri, M. M., Kheiri, S., Milani, A. S., Kim, K., & Hoorfar, M. (2019). Permeability and mechanical properties of gradient porous PDMS scaffolds fabricated by 3D-printed sacrificial templates designed with minimal surfaces. Acta Biomaterialia, 96, 149–160. https://doi.org/10.1016/j.actbio.2019.06.040

[90] Zeinali, B., Soleimani Jafarabadi, H., & Bazargan, M. (n.d.). Novel Equations for Permeability and Elastic Modulus of Triply Periodic Minimal Surface Scaffolds via Experimental and Numerical Analysis. Advanced Engineering Materials, n/a(n/a), 2500414. https://doi.org/10.1002/adem.202500414

[91] Wu, X., & Leung, D. Y. C. (2011). Optimization of biodiesel production from camelina oil using orthogonal experiment. Applied Energy, 88(11), 3615–3624. https://doi.org/10.1016/j.apenergy.2011.04.041

[92] Zhu, J., Chew, D. A. S., Lv, S., & Wu, W. (2013). Optimization method for building envelope design to minimize carbon emissions of building operational energy consumption using orthogonal experimental design (OED). Habitat International, 37, 148–154. https://doi.org/10.1016/j.habitatint.2011.12.006

[93] Guo, W., Yang, Y., Liu, C., Bu, W., Guo, F., Li, J., Wang, E., Peng, Z., Mai, H., You, H., & Long, Y. (2023). 3D printed TPMS structural PLA/GO scaffold: Process parameter optimization, porous structure, mechanical and biological properties.

Journal of the Mechanical Behavior of Biomedical Materials, 142, 105848. https://doi.org/10.1016/j.jmbbm.2023.105848

[94] Gao, T., Liu, K., Wang, X., Li, Z., & Wang, Z. (2022). Elastic mechanical property hybridization of configuration-varying TPMS with geometric continuity. Materials & Design, 221, 110995. https://doi.org/10.1016/j.matdes.2022.110995

[95] Lu, C., Ding, J., Jiang, X., Wen, P., Zhang, C., Shen, Q., & Chen, F. (2024). Enhancing mechanical properties and damage tolerance of additive manufactured ceramic TPMS lattices by hybrid design. Journal of the American Ceramic Society, 107(10), 6524–6531. https://doi.org/10.1111/jace.19978

[96] Song, W., Li, R., Feng, G., & Xiao, L. (2025). Dynamic mechanical behaviors and deformation mechanism of hybrid triply periodic minimal surface structures. International Journal of Impact Engineering, 203, 105359. https://doi.org/10.1016/j.ijimpeng.2025.105359

[97] Novak, N., Al-Ketan, O., Borovinšek, M., Krstulović-Opara, L., Rowshan, R., Vesenjak, M., & Ren, Z. (2021). Development of novel hybrid TPMS cellular lattices and their mechanical characterisation. Journal of Materials Research and Technology, 15, 1318–1329. https://doi.org/10.1016/j.jmrt.2021.08.092

[98] Novak, N., Tanaka, S., Hokamoto, K., Mauko, A., Yilmaz, Y. E., Al-Ketan, O., Vesenjak, M., & Ren, Z. (2023). High strain rate mechanical behaviour of uniform and hybrid metallic TPMS cellular structures. Thin-Walled Structures, 191, 111109. https://doi.org/10.1016/j.tws.2023.111109

[99] Nazir, A., Hussain, S., Ali, H. M., & Waqar, S. (2024). Design and mechanical performance of nature-inspired novel hybrid triply periodic minimal surface lattice structures fabricated using material extrusion. Materials Today Communications, 38, 108349. https://doi.org/10.1016/j.mtcomm.2024.108349

[100] Gao, T., Liu, K., Wang, X., Shen, L., Zhao, Y., Wei, K., & Wang, Z. (2023). Elastic wave manipulation via functional incorporation of air-solid phases in hybrid TPMS. Composites Communications, 44, 101745. https://doi.org/10.1016/j.coco.2023.101745

[101] Wang, J., Qian, C., Zhang, F., Qiu, X., Yu, B., Shi, J., & Chen, J. (2025). Experimental and numerical analysis of functionally graded hybrid TPMS heat exchangers for enhanced flow and thermal performance. Applied Thermal Engineering, 264, 125528. https://doi.org/10.1016/j.applthermaleng.2025.125528

[102] Gao, T., Liu, K., Wang, X., Wei, K., & Wang, Z. (2024). Multi-level mechanism of biomimetic TPMS hybridizations with tailorable global homogeneity and heterogeneity. Extreme Mechanics Letters, 68, 102136. https://doi.org/10.1016/j.eml.2024.102136

[103] Yin, Y., Li, F., & Zhu, D. (2025). Enhanced energy absorption characteristics of TPMS lattice structures with linear and circular hybrid designs. Engineering Structures, 340, 120759. https://doi.org/10.1016/j.engstruct.2025.120759

[104] Zhang, X., Xie, X., Yan, S., Li, Y., Fang, Y., Wang, C., & Ke, L. (2025). Dynamic compressive behaviour of multi-dimensional hybridized TPMS structure. Thin-Walled Structures, 213, 113304. https://doi.org/10.1016/j.tws.2025.113304

[105] Li, F., Gan, J., Zhang, L., Tan, H., Li, E., & Li, B. (2024). Enhancing impact resistance of hybrid structures designed with triply periodic minimal surfaces. Composites Science and Technology, 245, 110365. https://doi.org/10.1016/j.compscitech.2023.110365

[106] Li, P., Huang, H., Luo, X., Cai, A., Liu, H., Zhou, H., Chen, Y., & Ou, C. (2025). Parametric Design and Mechanical Behavior of Hybrid TPMS Lattice Structures Based on Sigmoid Function. Advanced Engineering Materials, 27(15), 2402360. https://doi.org/10.1002/adem.202402360

[107] Yoo, D.-J., & Kim, K.-H. (2015). An advanced multi-morphology porous scaffold design method using volumetric distance field and beta growth function. International Journal of Precision Engineering and Manufacturing, 16(9), 2021–2032. https://doi.org/10.1007/s12541-015-0263-2

[108] Zhang, J., Xie, S., He, G., Li, T., Sun, G., Zhou, Z., & Cui, Y. (2025). Design of hybrid triply periodic minimal surface structures to enhance structural dynamic compression behavior. Composite Structures, 354, 118790. https://doi.org/10.1016/j.compstruct.2024.118790

[109] Zhang, J., Xie, S., Li, T., Liu, Z., Zheng, S., & Zhou, H. (2023). A study of multi-stage energy absorption characteristics of hybrid sheet TPMS lattices. Thin-Walled Structures, 190, 110989. https://doi.org/10.1016/j.tws.2023.110989

[110] Liu, Z., Wang, M., Guo, P., Gao, D., Gao, Y., & Yang, J. (2025). Bio-inspired wall thickness modulation of hybrid TPMS structures for enhanced energy absorption. Engineering Structures, 343, 121020. https://doi.org/10.1016/j.engstruct.2025.121020

[111] Wang, C., Yan, S., Li, Y., Zhang, X., Xie, X., Zheng, H., Xue, X., & Fang, Y. (2025). Improved mechanical behavior of hybrid structures designed with triply periodic minimal surfaces. Materials Today Communications, 46, 112581. https://doi.org/10.1016/j.mtcomm.2025.112581

[112] Ye, J., He, W., Wei, T., Sun, C., & Zeng, S. (2023). Mechanical Properties Directionality and Permeability of Fused Triply Periodic Minimal Surface Porous Scaffolds Fabricated by Selective Laser Melting. ACS Biomaterials Science & Engineering, 9(8), 5084–5096. https://doi.org/10.1021/acsbiomaterials.3c00214

[113] Na, X., Xia, Z., Han, P., & Bai, G. (2025). Parametric design and performance evaluation of a hybrid triple-periodic minimal surface. Progress in Additive Manufacturing. https://doi.org/10.1007/s40964-025-01237-8

[114] Ciklacandir, S., Mihcin, S., & Isler, Y. (2022). Detailed Investigation of Three-Dimensional Modeling and Printing Technologies from Medical Images to Analyze Femoral Head Fractures Using Finite Element Analysis. IRBM, 43(6), 604–613. https://doi.org/10.1016/j.irbm.2022.04.005

[115] The Stanford 3D Scanning Repository. accessed on 15 Sep. 2025. https://graphics.stanford.edu/data/3Dscanrep/.

[116] Constructive solid geometry. Wikipedia. accessed on 15 Sep. 2025. https://en.wikipedia.org/w/index.php?title=Constructive_solid_geometry&oldid=1301631591

[117] Lin, C., Wen, G., Yin, H., Wang, Z. P., Liu, J., & Xie, Y. M. (2022). Revealing the sound insulation capacities of TPMS sandwich panels. Journal of Sound and Vibration, 540, 117303. https://doi.org/10.1016/j.jsv.2022.117303

[118] Al-Ketan, O., & Abu Al-Rub, R. K. (2021). MSLattice: A free software for generating uniform and graded lattices based on triply periodic minimal surfaces. Material Design & Processing Communications, 3(6), e205. https://doi.org/10.1002/mdp2.205

[119] Jones, A., Leary, M., Bateman, S., & Easton, M. (2021). TPMS Designer: A tool for generating and analyzing triply periodic minimal surfaces. Software Impacts, 10, 100167. https://doi.org/10.1016/j.simpa.2021.100167

[120] Cui, W., Li, X., Zhou, S., & Weng, J. (2007). Investigation on process parameters of electrospinning system through orthogonal experimental design. Journal of Applied Polymer Science, 103(5), 3105–3112. https://doi.org/10.1002/app.25464

[121] Lock, E., Ghasemi, M., Mostofi, M., & Rasouli, V. (2012). An experimental study of permeability determination in the lab. WIT Transactions on Engineering Sciences, 80, 221-230. https://doi.org/10.2495/PMR120201

[122] Heller, R., Vermylen, J., & Zoback, M. (2014). Experimental investigation of matrix permeability of gas shales. AAPG Bulletin, 98(5), 975–995. https://doi.org/10.1306/09231313023

[123] Reynolds, B. W., Fee, C. J., Morison, K. R., & Holland, D. J. (2023). Characterisation of Heat Transfer within 3D Printed TPMS Heat Exchangers. International Journal of Heat and Mass Transfer, 212, 124264. https://doi.org/10.1016/j.ijheatmasstransfer.2023.124264

[124] Hibbitt, Karlsson & Sorensen, Inc (2001). ABAQUS/standard User's Manual.

[125] Rathore, S. S., Mehta, B., Kumar, P., & Asfer, M. (2024). Thermo-Hydrodynamic Performance Evaluation of a Mini-Channel Inserted With TPMS-Based Porous Lattice. Journal of Thermal Science and Engineering Applications, 16(6), 061009. https://doi.org/10.1115/1.4065189

[126] Shen, M., Qin, W., Xing, B., Zhao, W., Gao, S., Sun, Y., Jiao, T., & Zhao, Z. (2021). Mechanical properties of 3D printed ceramic cellular materials with triply periodic minimal surface architectures. Journal of the European Ceramic Society, 41(2), 1481–1489. https://doi.org/10.1016/j.jeurceramsoc.2020.09.062

Curriculum Vitae

Personal data

Surname Name: Zhang Yu

Data, Place of birth: 23/01/1996, Hunan, China

Ph.D. course: Industrial Engineering

Curriculum: Materials Engineering

Cohort: XXXVIII

Education and research

09/2024-07/2022

Ph.D. - Department of Industrial Engineering, University of Padova, Italy

09/2017-07/2020

Master of Engineering Mechanics – School of Mechanics and Engineering, Liaoning Technical University, China

2013/09-2017/07

Bachelor of Theoretical and Applied Mechanics - School of Mechanics and Engineering, Liaoning Technical University, China